1993

# Forest Fires in Western Europe in 1987

Philippe Le Canut
*College of William & Mary - Arts & Sciences*

# FOREST FIRES IN WESTERN EUROPE IN 1987

---

A Thesis

Presented to

The Faculty of the Applied Science Program

The College of William and Mary in Virginia

In Partial Fulfillment

Of the Requirements for the Degree of

Master of Arts

---

by

Philippe Le Canut

1993

APPROVAL SHEET

This thesis is submitted in partial fulfillment of

the requirements for the degree of

Master of Arts

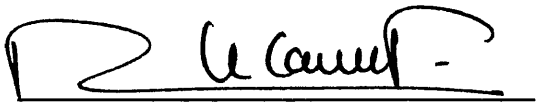

Philippe J.F. Le Canut

Approved, May 1993

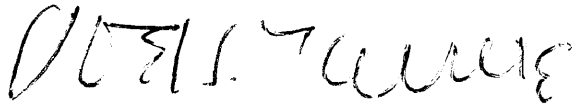

Joel S. Levine

Dennis M. Manos

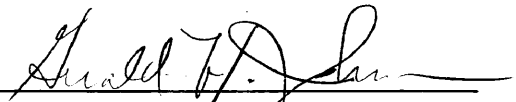

Gerald H. Johnson
Geology Department

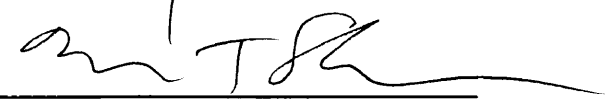

Marc T. Sher
Physics Department

TABLE OF CONTENTS

ACKNOWLEDGEMENTS

The author would like to thank Don Cahoon (the remote sensing expert) for answering many questions about the processing of satellite imagery, as well as Mark Kiser (system manager of the ASD branch) for solving unexpected data processing problems. In addition, Dr. J.S. Levine is acknowledged for his constant support and his careful review of this thesis. Without him, the author would not have gotten the authorization to work at the NASA Langley Research Center due to his foreign citizenship. Also many thanks to Gerald Johnson, Dennis Manos, and Marc Sher for their careful reading and criticism of the manuscript. Finally, a special thank you to everyone, and especially to my friend Peter, who helped me with my English while writing this thesis.

LIST OF TABLES

LIST OF FIGURES

LIST OF SATELLITE IMAGES

# ABSTRACT

The purpose of this study was to determine the total amount of $CO_2$ released due to forest fires in western Europe in the year 1987 and to map its spatial distribution on a $1^o \times 1^o$ grid.

The climate and the vegetation in western Europe influence the spatial distribution of the burning on a regional scale. It is shown that the majority of the burning is concentrated around the Mediterranean Sea.

The total $CO_2$ emission due to forest fires in 1987 turns out to be negligible compared to the industrial emissions in western Europe.

In order to map the $CO_2$ emissions on a $1^o \times 1^o$ grid, satellite remote sensing techniques were used. The Local Area Coverage (LAC) format of the Advanced Very High Resolution Radiometer (AVHRR) sensor onboard the NOAA-9 satellite was selected to provide the data because of its low price and its relatively high resolution. Images were selected and ordered after studying METEOSAT images in May and April of 1987 and 1988.

The regional classification of burn scars showed that a $1^o \times 1^o$ grid can not be obtained on a continental scale due to differences between scars in different ecosystems and the presence of certain land surfaces having spectral properties similar to those of scars. An estimation for the overlap between different scars is proposed and applied to the few known scars.

The local classification of burn scars showed that even in a single ecosystem, scar signatures vary too much with the imagery selected to result in a precise estimation of the size and distribution of the fires. A coefficient estimating the precision of the classification is proposed and applied.

# TRACE GAS EMISSIONS DUE TO FOREST FIRES
# IN WESTERN EUROPE IN 1987
# AND REMOTE SENSING OF SCARS RESULTING THE BURNING

# INTRODUCTION

World biomass burning appears to be one of the major sources of atmospheric carbon dioxide and carbon monoxide, both trace gases of significant importance in the greenhouse effect and in tropospheric chemistry, respectively. A worldwide estimation of the distribution of these trace gases is presently being developed at the NASA Langley Research Center for the year 1987. This year has been chosen among others because the extent of burning in the world was particularly important during this year. A final goal is to produce a $1^{o}\times1^{o}$ grid of the trace gas emissions due to biomass burning all over the Earth, that will serve as input data into a numerical model of the carbon cycle. The latter consists of the interaction between the atmosphere, the biosphere, and the ocean. It will assess how the added amount of carbon, due to biomass burning, to the atmosphere is distributed among the three mentioned systems.

Studies in parts of the world like South America, Africa, Asia, and circumpolar countries have already been carried out for 1987 with the help of remote sensing to locate scars and estimate their respective sizes. Western Europe has not been studied so far because of the relatively small amount of burning in this part of the world. Nevertheless, biomass burning in western Europe has to be documented in order to evaluate the feasibility of getting the corresponding $1^{o}\times1^{o}$ grid of the trace gas emissions.

After a detailed description of the biomass burning around the world and its consequences to the environment, forest fires and their emissions in western Europe will first be documented, then related to climatic factors and the air circulation pattern, and finally

quantified. At this point, a raw estimation of the spatial distribution will be provided.

Then a remote sensing study of the burn scars, that result from fires, will be implemented on a regional and local scale in order to assess the precise spatial distribution of the burning. Remote sensing consists of a spectral separation of the electromagnetic radiation reflected and emitted by the Earth. Sensors onboard satellites measure in different wavelength bands the spectral properties of ground surfaces. Remote sensing of fires is implemented through a spectral classification of burn scars. The regional classification of scars will result in a qualitative study, whereas the local classification will result in a quantitative study. Several classification principles will be applied and their results compared. The similarity of individual scars as well as the classification error will be estimated.

It will finally be determined whether remote sensing is an adequate technique for the detection of burning in western Europe, as it is for the tropical forests in Africa, South America, and Asia.

# CHAPTER I

## BIOMASS BURNING AROUND THE WORLD

In determining the composition of the major components of the atmosphere, including $CO_2$, biomass burning had been considered unimportant for a long time. Fires in industrialized countries were not always reported and documented, and fires in developing countries were overlooked most of the time because of the lack of competent authorities and because of politics. But in the 1970's began a massive deforestation in the tropical forests, principally in the Amazon Basin, which has alerted the scientific community around the world. Since this time, many regional experiments have been conducted. Only lately has the scientific community realized the full scope of the problem. Biomass burning may be a major problem with harmful consequences to the environment.

Lately biomass burning around the world has dramatically increased. According to Houghton's studies[1] biomass burning may have increased by about 50% around the world since 1850. In Latin America alone, where forests are burned and converted to grasslands, pastures and croplands, the rate of deforestation has increased by 50% between 1850 and 1985. Similarly, analyses of countries accounting for 75% of the area in South and South East Asia show a 50% increase in the area of croplands, grasslands and scrublands between 1850 and 1980. Levine[2] has discussed this trend, showing the decrease of the forested and woodland area in ten world regions. The figures are displayed in Table 1.1. Between 1850 and 1980, there has been a decrease for 9 out of 10 of the world's regions. The decrease can be as important as 59% in North Africa & Middle East and the region

which experienced the largest burned area (269 million hectares) is Latin America. The only region which experienced an increase in forested land (5%) is Europe which has been settled and industrialized for many centuries. That is why no more deforestation with industrialization purposes takes place. Moreover there a recent growing environmental concern among the European population resulting in letting new forests and woodlands grow. Nevertheless, the worldwide decrease in forested and woodland areas is 15% with a burned area of 912 million hectares (Levine[2]).

The most tangible demonstration of biomass burning was given by astronauts onboard the space shuttle who have observed differences in smoke palls which appeared over certain regions of the world in a 10 year interval of time (Charles A. Wood and Raymond Nelson[3]). In 1973 and 1983 the area covered by Amazon smoke was about 300 000 $km^2$. This smoke was mainly produced by the burning of agricultural stubble. But in 1985 and 1988 they reported continent-sized Amazon smoke plumes: 3 500 000 $km^2$ and 3 000 000 $km^2$, respectively. These clouds were produced by forest fires (65%) and agricultural fires (35%). The area of the smoke plumes correlates with the cumulative area of deforestation due to the exponential rate of deforestation in this part of the world.

The geographical location, extent and temporal distribution as well as the causes of biomass burning will be discussed in this chapter. The geographical and temporal distributions turn out to be two relevant means of classification.

Most of today's burning occurs in the tropics and the boreal forests of the world. The temperate regions have not yet been very well documented. Nevertheless, estimations do exist and turn out to be much less important than those for the tropical forests. The tropics consist of several regions and ecosystems around the globe. These regions are the

tropical forests in the Amazon basin and in Asia, and the African savanna.

Worldwide, the present day biomass burned is about 8700 Tg (1 Tg = $10^{12}$ g) of dry material per year (Andreae[4]). The partition of this total amount is shown in Table 1.2. In this table, the boreal forests are included with the temperate forests. Most of the burning occurs in the African savanna, more than 40% of the worldwide total. The burning in the tropical forests does not exceed the amount of fuelwood burned and is certainly less than the amount of agricultural waste burned. Nevertheless, it is about 15% of the worldwide amount and therefore should not be overlooked because it is constantly increasing.

The other way to categorize biomass burning is to use the temporal distribution of the fires. Some fires are recurrent, like the savanna fires, some are unexpected, like the boreal fires, and others grow exponentially, like the tropical forest fires. Each one has a different cause.

The recurrent fires in the African savanna occur each year with a strikingly similar pattern with reference to the spatial and temporal distribution (Cahoon[5]). The seasonality of the burning in the savanna shows up very clearly when the extent of the burned area is displayed month after month. The variability is due to variations in the precipitation pattern. These fires, whose extent is about 1530 million hectares are almost all human initiated because of the burning's agricultural role, and are left uncontrolled because of the lack of firefighting equipment. Savanna is burned for clearing, grazing, hunting and pest purposes (Andreae[4]).

The boreal fires are, in general, wildfires and therefore have a low spatial frequency and are randomly spread out in certain regions. Most of the boreal fires occur in

Canada, the former Soviet Union, Finland, Norway, Sweden and Alaska (Stocks[6]). The annual average area burned in these regions during the 1980-1989 period is about 5 600 000 ha. Their extent is not to be overlooked. For example, the Great Chinese fire of 1987, which lasted three weeks on both sides of the boundary between the People's Republic of China and the former Soviet Union, documented by Cahoon et al[7], was estimated to be of 1.1 million hectares in the People's Republic of China and of 3.6 million hectares in the former Soviet Union. The weather plays a critical role as far as all the boreal fires are concerned. The year 1987 was particularly bad in terms of the extent of burning in the boreal forests mainly because of this exceptional fire in China and the former Soviet Union. There are many possible causes of wildfires. Lightning contributes to between 10 and 30% of wildfires (Andreae[4]). The rest are caused by accident, negligence or arson.

Burning in the tropical forests has seen spectacular increases in recent years due to deforestation. In the tropical forests of the Amazon basin, burning is associated with land clearing for new plots, shifting cultivation, biomass mineralization, ranch burning and population growth (Malingreau et al[8]). Nevertheless, a differentiation should be made between shifting cultivation and permanent removal. According to Andreae[4], shifting cultivation is not expected to grow much beyond its present extent of 300 to 500 million hectares per year. On the other hand, permanent removal is expected to expand due to growing populations requiring more open land and more food. The current rate of yearly deforestation is estimated by Kaufman[9] to be about 30% for the states of Amazonas, Mato Grosso, Para and Rondonia.

In the tropical forests of South East Asia, the drought of 1982 and 1983 enhanced a process similar to that of the Amazon basin. The tropical forests of Kalimatan and North Borneo suffered greatly during the intense El Nino warming in the Eastern Pacific. For

three months fires burned unabated (Kaufman[9]). It has been estimated that 3.5 million hectares were affected by drought and fire in East Kalimatan and that 1.5 million hectares were damaged in North Borneo in what, until the Great Chinese fire in 1987, was the major fire of the century (Kaufman[9]).

At the Chapman Conference on Global Biomass Burning, held in Williamsburg in 1990, researchers attempted to assess the extent of biomass burning around the world, to quantify the production of atmospheric gases and particulates and to evaluate the effect of gases on the composition and chemistry of the atmosphere.

TABLE 1.1

EVOLUTION OF THE FORESTED AREA IN 10 WORLD REGIONS

BETWEEN 1850 AND 1980

| Country | 1850 forested area (million ha) | 1980 forested area (million ha) | Difference (million ha) | Change |
|---|---|---|---|---|
| Latin America | 1420 | 1151 | 269 | -19% |
| Tropical Africa | 1336 | 1074 | 262 | -20% |
| Soviet Union | 1067 | 941 | 126 | -12% |
| North America | 971 | 942 | 29 | -3% |
| South Asia | 317 | 180 | 137 | -43% |
| Pacific countries | 267 | 246 | 21 | -8% |
| Southeast Asia | 252 | 235 | 17 | -7% |
| Europe | 159 | 167 | 8 | +5% |
| China | 96 | 58 | 38 | -40% |
| North Africa &ME | 34 | 14 | 20 | -59% |
| World | 5919 | 5007 | 912 | -15% |

Source: Andreae[4]

TABLE 1.2

PRESENT-DAY BIOMASS BURNED

| Source | Present-day biomass burned (Tg dm/yr.) |
|---|---|
| Tropical forests | 1260 |
| Temperate forests | 280 |
| Savanna | 3690 |
| Agricultural waste | 2020 |
| Fuelwood | 1430 |
| World total | 8680 |

Source: Andreae[4]

## NOTES TO CHAPTER I

1. Houghton, R. A. Global Biomass Burning: Atmospheric, Climatic, and Biospheric Implications. 322-325 Cambridge, Massachusetts: MIT Press, 1991.

2. Levine, J. S., Cofer III, W. R., Winstead, E. L., Rhinehart, R. P., Cahoon, Jr., D. R., Sebacher, D. I., Stocks, B. J. Global Biomass Burning: Atmospheric, Climatic, and Biospheric Implications. 264-271 Cambridge, Massachusetts: MIT Press, 1991.

3. Wood, C. A., Nelson, R. Global Biomass Burning: Atmospheric, Climatic, and Biospheric Implications. 29-40 Cambridge, Massachusetts: MIT Press, 1991.

4. Andreae, M. O. Global Biomass Burning: Atmospheric, Climatic, and Biospheric Implications. 3-21 Cambridge, Massachusetts: MIT Press, 1991.

5. Cahoon, Jr., D. R., Stocks, B. J., Levine, J. S., Cofer III, W. R., O'Neill, K. P. Seasonal Distribution of African Savanna Fires, Nature, Vol 359, 812-815.

6. Stocks, B. J. Global Biomass Burning: Atmospheric, Climatic, and Biospheric Implications. 197-202 Cambridge, Massachusetts: MIT Press, 1991.

7. Cahoon, Jr., D. R., Levine, J. S., Cofer II, W. R., Miller, J. E.,Minnis, P., Tennille, G. M., Yip, T. M., Stocks, B. J., Heck, P. W. Global Biomass Burning: Atmospheric, Climatic, and Biospheric Implications. 61-66 Cambridge, Massachusetts: MIT Press, 1991.

8. Malingreau, J. P. Fire in the Tropical Biota: Ecosystem Processes and global Challenge. 337-368 Berlin, Heidelberg: Sprinter-Verlag, 1990.

9.Kaufman,Y. J., Setzer, A., Justice, C.,Peireira, M. C., Fung, I. Fire in the Tropical Biota: Ecosystem Processes and global Challenges. 371-397 Berlin, Heidelberg: Sprinter-Verlag, 1990.

# CHAPTER II

# COMBUSTION CHEMISTRY AND EFFECTS OF BURNING

The assessment of the contribution of burning to the global budgets of atmospheric gases and particulates is an important goal of the IGAC[1] project (International Global Atmospheric Chemistry), a core project of the IGBP (International Geosphere-Biosphere Program). An understanding of the atmospheric composition is needed in order to better evaluate the impact of biomass burning.

About 85% of the total mass of the atmosphere is found in the troposphere (0-15km). Above the troposphere is the stratosphere (15-50 km). Short-lived trace gases produced by biomass burning do not cross the tropopause. On the other hand, long-lived trace gases like methylchloride ($CH_3Cl$) can diffuse into the stratosphere where 90% of the total ozone is located and can destroy this ozone which protects us from the lethal solar radiation (<300 nm).

The ground level concentrations of the major atmospheric gases in dry air by volume are the following: dinitrogen ($N_2$) 78.1%, dioxygen ($O_2$) 20.9%, and argon (Ar) 0.93%. These are not, however, the only gases. There are about 1500 different gases in the atmosphere, 99% of which are man-made. Since their concentrations are on the order of parts by million by volume (ppmv) or parts by billion by volume (ppbv), they are called trace gases. These gases perturb the fragile chemical equilibrium of the atmosphere and can have harmful effects on the biota. As an example, tropospheric ozone is known to cause respiratory ailments for humans. The most important trace gases can be classified

into six species; the carbon species: carbon dioxide ($CO_2$), methane ($CH_4$), carbon monoxide (CO), and non methane hydro carbon (NMHC); the nitrogen species: molecular nitrogen ($N_2$), nitrous oxide ($N_2O$), nitrogen monoxide (NO), nitrogen dioxide ($NO_2$), and ammonia ($NH_3$); the sulfur species: sulfur dioxide ($SO_2$), hydrogen sulfide ($H_2S$), dimethyl disulfur (DMDS); the halogen species: chlorofluorocarbon (CFC), methylchloride ($CH_3Cl$), methylbromide ($CH_3Br$); the hydrogen species: water ($H_2O$), dihydrogen ($H_2$), hydroxyl radical (OH), hydrogen dioxide ($HO_2$), hydrogen peroxide ($H_2O_2$); and the oxygen species: molecular oxygen ($O_2$), atomic oxygen (O), ozone ($O_3$). Not only is their concentration important to the chemical equilibrium, but also their lifetime is significant. If a lifetime of a gas is greater than two years, then the gas is uniformly mixed throughout the whole atmosphere. Table 2.1 shows the current concentrations and lifetimes of the major trace gases. The concentrations and the lifetimes vary greatly and therefore affect the global balance differently.

Biomass burning is an important source of particulates and trace gases to the atmosphere. The biomass burn particulates are composed of elemental carbon and compounds of nitrogen (N), carbon (C), sulfur (S), and metallic elements. The amounts of total particulate matter (TPM), particulate organic carbon (POC), and elemental carbon (EC) released by biomass burning, and those for all sources, have been estimated by Andreae[2] and are shown in Table 2.2. According to Andreae[2], 7% of the total particulate matter in the atmosphere is due to biomass burning, whereas biomass burning accounts for more than one third of the total particulate organic matter and for more than three quarters of the total elemental carbon.

These particulates affect the global climate because they affect the transmission of incoming solar radiation and outgoing infrared radiation. They participate in changing the total albedo of the Earth. The size of the particles, produced during the flaming phase of a

wetland fire, range between 0.1 μm and 0.2 μm while the particles produced during the following smoldering phase are coarser[3]. Therefore, biomass burn particulates are important cloud condensation nuclei. In order to form droplets, the cloud particles have to increase in size about a million times. These particles are nucleated by heterogeneous nucleation on atmospheric aerosols.

The major gases produced by biomass burning can be classified into two categories: the atmospheric greenhouse gases ($CO_2$, $CH_4$, $N_2O$, and tropospheric ozone) and the chemically active gases (NO, CO, $H_2$, $CH_3Cl$, NMHC, $NH_3$). All these gases are produced in different quantities during or after biomass burning. Moreover, for each one of them, the rate of release varies upon the time elapsed since the onset of the fire (Cofer[4]).

The first phase of burning is called flaming and is usually very hot (700 $^oK$). It lasts about 90 seconds. The second phase of burning is called smoldering and is usually cooler (350 $^oK$). It lasts longer than the flaming phase (Kaufman et al[5]). During flaming, the highly oxidized species ($CO_2$, $NO_x$, $N_2O$) are produced and, during smoldering, the less oxidized species (CO, $CH_4$, NMHC) and smoke particles are produced.

Carbon dioxide ($CO_2$) is produced by complete combustion of the biomass of which the composition can be represented by $CH_2O$. The chemical reaction is:

$$CH_2O + O_2 \rightarrow H_2O + CO_2$$

Carbon monoxide (CO) is produced by incomplete combustion and the chemical reaction is:

$$2\ CH_2O + O_2 \rightarrow 2\ H_2O + 2\ CO$$

Methane ($CH_4$) is produced during biomass burning by incomplete combustion and also after biomass burning by the metabolic activity of a methanogenic bacteria in an anaerobic environment.

Tropospheric ozone is not directly produced during biomass burning but is an indirect product. The tropospheric ozone cycle is:

$$NO_2 + h\nu \rightarrow NO + O$$

$$O + O_2 + M \rightarrow O_3 + M$$

$$NO + O_3 \rightarrow NO_2 + O_2$$

Nitrogen dioxide ($NO_2$) is produced by biomass burning and then is broken up by solar radiation to form atomic oxygen which combines with molecular oxygen to finally form ozone.

Nitrous oxide ($N_2O$) and nitric oxide (NO) are both produced during biomass burning and after biomass burning by nitrification and denitrification of soils. These emissions are enhanced after biomass burning (Levine[6]). Nitrification is an aerobic process. Ammonium ($NH_4^+$) combines with molecular oxygen in order to form nitrous oxide and nitric oxide. Denitrification is an anaerobic process. Nitrate ($NO_3^-$) decays and yields nitrous oxide and nitric oxide. The ratios $N_2O/N_2$ and $NO/N_2$ in denitrification are respectively 1-2% and less than 1%. A new term (pyrodenitrification) was coined for these emissions. World estimates range from 12 to 28 Tg of nitrogen per year following biomass burning.

Using the figures in Table 1.2, Andreae[2] estimates the present day carbon releases in Tg/yr. for several sources and gives the estimates for the year 1850. The results are dis-

played in Table 2.3. Today's savanna accounts for the majority of the world's carbon releases (more than 40%). More importantly, it accounts for twice as much as the total of the carbon released by both tropical and temperate forests. Nevertheless, the carbon released from deforestation must be distinguished from the carbon released from savannas. This latter has no or little effect on the greenhouse effect because in savannas a regrowth occurs during the next growing cycle and the amount released during biomass burning is used up through photosynthesis. If there is no regrowth, then the carbon dioxide is added to the atmosphere and its concentration builds up. Grass and crops can take up less $CO_2$ than high forests. A net increase in the amount of carbon released due to deforestation can be pointed out over the period 1850 to 1980. It goes from 175 Tg/yr. to 570 Tg/yr., while the amount released by savannas does not increase much because, for centuries, savannas have been cleared to the same extent.

According to Andreae[2], 45% of the biomass matter is released in the form of carbon species ($CO_2$, CO, $CH_4$, NMHC). When the masses of these four elements are added up together (Table 2.4), it comes up to 3912 Tg/yr., which is about 45% of the total biomass burned, 8680 Tg/yr. (Table 1.2). Table 2.4 gives the amount of all the trace gases produced by biomass burning. Included in this chart is the total amount of these same gases produced by all sources. Up to 40% of the worldwide emissions of $CO_2$ are due to biomass burning; up to 30% of the worldwide emissions of CO are also due to biomass burning; more than one third of the tropospheric ozone is to be accounted for by biomass burning. For all the other gases, the ratios are greater then 10%, which is not negligible.

Specific data exists for these trace gas emissions. For example, the DECAFE program (Dynamics and Chemistry of the Atmosphere in Equatorial Forests) has provided data allowing the detection of strongly acidic precipitation and abnormally high ozone concentrations in the Tropics. Also, concentrations of particular gases can be measured in

the atmosphere by the use of remote sensing. Measurements of the number density of CO all over the world have been carried out in the middle and upper troposphere by MAPS (Measurement of Air Pollution by Satellite) when this sensor flew on the space shuttle in 1981 and 1984. The highest CO concentrations were measured in the tropical regions of Africa and of the Amazon basin (Connors[7]). These levels, unmistakably attributed to biomass burning, were reported to be greater than those in industrialized areas. These experiments support the theory of large trace gas emissions due to biomass burning.

The potential consequences of these high emissions of trace gases are several. The mean albedo of the earth changes while the greenhouse effect and the acidic precipitation are enhanced. Moreover tropospheric ozone builds up. These consequences are harmful to the environment and humans.

The albedo of deforested regions is about 18-20% whereas the albedo of high forests is about 12% (Wood and Nelson[8]). High forests indeed reflect the solar radiation less than pastures and crops. More importantly, smoke palls have an albedo of 50% or more. Their extent has been emphasized in chapter I. Once these figures are used in a general circulation model, the albedo changes result in increases in temperatures and in a reduction of evaporation and rainfall. The radiation budget is therefore affected. The greenhouse effect is enhanced by biomass burning. Some molecules produced by biomass burning, like $CO_2$, $CH_4$ and $N_2O$, trap the outgoing infrared radiation and cause a radiative forcing which is a temperature enhancement resulting from the absorption and reemission of a particular gas. Each gas has a different radiative forcing. Furthermore, the water vapor feedback of the greenhouse gases produced by biomass burning has to be considered. If $CO_2$ is taken as unity, then the global warming potential (GWP) of $CH_4$ is 63 and the GWP of $N_2O$ is 270. These figures are based on the concentrations and the lifetimes of the gases.

The acidic precipitation is also enhanced. The nitric oxide (NO) is further oxidized to nitrogen dioxide ($NO_2$), which becomes nitric acid ($HNO_3$), a main component of the acid rain.

All these consequences of biomass burning affect the global climate. Biomass burning contributes therefore to the global change which main characteristic is the buildup of greenhouse gases.

TABLE 2.1

CONCENTRATION AND LIFETIME OF THE MAJOR TRACE GASES

| Species | Concentration | Lifetime |
|---|---|---|
| $N_2O$ | 0.31 ppmv | 150 years |
| NO | 0.001-10 ppbv | 1-2 days |
| $NO_2$ | 0.002-20 ppbv | 1-2 days |
| $NH_3$ | 0.1 ppbv | 10 days |
| CFC11 ($CCl_3F$) | 280 pptv | 65 years |
| CFC12 ($CCl_2F_2$) | 484 pptv | 130 years |
| $CH_3Cl$ | 600 pptv | 1.5 years |
| $CH_3Br$ | 10 pptv | 1.5 years |
| $CO_2$ | 350 ppmv | 50-1000 years |
| $CH_4$ | 1.7 ppmv | 8 years |
| CO | 0.1-1 ppmv | 3 months |

TABLE 2.2

RATIO OF PARTICULATE EMISSIONS DUE TO BIOMASS BURNING

| Particulates | Biomass burning (Tg/yr.) | All sources (Tg/yr.) | Ratio due to biomass burning |
|---|---|---|---|
| TPM | 104 | 1530 | 7 |
| POC | 69 | 180 | 39 |
| EC | 19 | <22 | >86 |

Source: Andreae[2]

TABLE 2.3

EVOLUTION OF THE CARBON EMISSIONS BETWEEN 1850 AND 1980

| Source | Present-day carbon released (Tg/yr.) | 1850 carbon released (Tg/yr.) |
|---|---|---|
| Tropical forests | 570 | 175 |
| Temperate forests | 130 | 250 |
| Savanna | 1660 | 1850 |
| Agricultural waste | 910 | NA |
| Fuelwood | 640 | 500 |
| World total | 3910 | 2775 |

Source: Andreae[2]

TABLE 2.4

WORLD EMISSIONS OF TRACE GASES DUE TO BIOMASS BURNING

| Gas | Biomass burning (Tg/yr.) | All sources (Tg/yr.) | Biomass burning (%) |
|---|---|---|---|
| $CO_2$ | 3500 | 8700 | 40 |
| CO | 350 | 1100 | 32 |
| $CH_4$ | 38 | 380 | 10 |
| NMHC | 24 | 100 | 24 |
| $NO_x$ | 8.5 | 40 | 21 |
| $NH_3$ | 5.3 | 44 | 12 |
| $CH_3Cl$ | 0.51 | 2.3 | 22 |
| $H_2$ | 19 | 75 | 25 |
| $O_3$ | 420 | 1100 | 38 |

Source: Andreae[2]

## NOTES TO CHAPTER II

1. Prinn, R. G. Global Biomass Burning: Atmospheric, Climatic, and Biospheric Implications. 22-28 Cambridge, Massachusetts: MIT Press, 1991.

2. Andreae, M. O. Global Biomass Burning: Atmospheric, Climatic, and Biospheric Implications. 3-21 Cambridge, Massachusetts: MIT Press, 1991.

3. Woods, D. C., Chuan, R. L.,Cofer III, W. R., Levine, J. S. Global Biomass Burning: Atmospheric, Climatic, and Biospheric Implications. 240-244 Cambridge, Massachusetts: MIT Press, 1991.

4. Cofer III, W. R., Levine, J. S., Winstead, R. L.,Stocks, B. J. Global Biomass Burning: Atmospheric, Climatic, and Biospheric Implications. 203-208 Cambridge, Massachusetts: MIT Press, 1991.

5. Kaufman,Y. J., Setzer, A., Justice, C.,Peireira, M. C., Fung, I. Fire in the Tropical Biota: Ecosystem Processes and global Challenges. 371-397 Berlin, Heidelberg: Sprinter-Verlag, 1990.

6. Levine, J. S., Cofer III, W. R., Winstead, E. L., Rhinehart, R. P., Cahoon, Jr., D. R., Sebacher, D. I., Stocks, B. J. Global Biomass Burning: Atmospheric, Climatic, and Biospheric Implications. 264-271 Cambridge, Massachusetts: MIT Press, 1991.

7. Connors, V. S., Cahoon, Jr., D. R., Reichle, H. G., Garstang, M., Seiler, W., Scheel, H. E. Global Biomass Burning: Atmospheric, Climatic, and Biospheric Implications. 147-153 Cambridge, Massachusetts: MIT Press, 1991.

8. Wood, C. A., Nelson, R. Global Biomass Burning: Atmospheric, Climatic, and Biospheric Implications. 29-40 Cambridge, Massachusetts: MIT Press, 1991.

# CHAPTER III

# CLIMATE AND VEGETATION IN WESTERN EUROPE

All over the world, the importance of biomass burning is closely related to climatic conditions. Fires are more likely to occur in dry, hot areas, whereas they are hindered by abundant precipitation. This is true in western Europe and therefore the climate over this continent needs to be discussed in order to better understand the distribution of fires in Europe. The air circulation over western Europe offer insight on the temperature, precipitation, and average cloudiness distributions.

Figures 3.1, 3.2, 3.3, and 3.4 come from Climates of Northern and Western Europe[1], whereas Figures 3.5, 3.6, 3.7, and 3.8 come from Goode's World Atlas[2].

The climate in Europe is referred to as "humid mesothermal". It is composed of two main subregions separated approximately by the 45 degree north latitude parallel (Figure 3.5). North of this latitude, the climate is "maritime". The winters are mild and the summers are cool. Northern Spain, France (except the very southern part), England, Germany, Austria, and Poland experience this climate. South of the 45 degree north parallel, the climate is "mediterranean". It is characterized by summer droughts and winter rains. Portugal, southern Spain, Italy (except the very northern part), Corsica, Sardinia, and Greece have this climate. Northern Italy and Yugoslavia do not belong to the two previous climate regions but to a slightly different one called "humid subtropical". Its main characteristics are mild winters and warm summers.

These climatic regions result from the air and sea circulation in this region of the world. The most important climate driver is indeed the large scale air circulation of the meandering westerly jet stream in the troposphere. This planetary wave influences the smaller synoptic scale motion, which is associated with day to day weather[4]. The weather of western Europe, therefore, depends upon the changing patterns of the tropospheric jet stream. Its pattern shows up on pressure contour maps. This westerly jet stream is a tropospheric phenomenon and therefore shows up best on a 500 mb contour map (Figures 3.1 and 3.3). The zonal tropospheric jet stream is clearly visible in Figure 3.1, where it is parallel to the isobars in the central band of the figure. On the surface contour maps (1000 mb), it is attenuated but still visible (Figures 3.2 and 3.4). Over Europe, the air circulation oscillates between one typical pattern and one atypical[1]. Figures 3.1 and 3.2 represent the so-called high-index circulation, whereas Figures 3.3 and 3.4 represent the so-called low-index circulation.

The most common pattern over Europe during a typical year is the high-index circulation pattern[1]. The tropospheric jet steam runs between a low pressure system over Iceland and a high pressure system over the Azores. Mild maritime air is carried over the continent where it encounters cold continental air. This results in the creation of a front at the surface. In winter, the low Icelandic pressure system is usually more developed than the Azorian high pressure system[4]. This extended cyclonic activity results in occluded fronts which sweep repeatedly across northern Europe. Cloudy and rainy weather follow suit in this part of Europe. The Azorian high pressure system produces a cloudless mild weather in the southern part of Europe in winter. In summer, the Icelandic low pressure system is less developed than the high Azorian pressure system[4]. The cyclonic activity over northern Europe is therefore less pronounced and less frequent yielding more equitable weather. In southern Europe, the anticyclonic activity warms up the continent and pushes northward the weak low pressure systems.

The low-index circulation is less frequent over Europe but is an important disturbing factor in the weather[1]. This circulation is characterized by a strong anticyclone over the Shetland Islands, which blocks the jet stream zonal circulation and splits it in two unequal parts. Most of the energy goes north to circle around the high pressure system and ends up over eastern Europe in low pressure systems which bring considerable rain in winter. The cyclonic activity takes place along south-north tracks (meridional circulation) rather than west-east tracks (zonal circulation)[1]. The southward part of the jet stream ends up in a cyclonic activity strongly developed in winter time over the mediterranean part of Europe. This meridional circulation is characterized in winter by low pressure systems over the Gulf of Genoa. These latter yield a strong northerly cold wind, called "Mistral", in southern France and a strong southerly warm wind, called "Scirocco", over Italy[1]. According Buys-Ballot's rule, with the wind blowing on your back in the northern hemisphere, the low pressures stand on your left. That is exactly what is happening around the Gulf of Genoa. This cyclonic activity in the Mediterranean part of Europe, due to the low-index circulation, is restricted to the winter season. In summer, the winds are weak and the weather sunny and steady due to the strong anticyclone blocking the perturbations coming from the west. This general circulation greatly influences the temperature, precipitation and cloud patterns.

The surface temperatures, which are displayed on Figure 3.7, are important in terms of the distribution of biomass burning over western Europe. It is well known that fires are associated in part with high environmental temperatures. Southern Spain, southern Portugal, and Sicily have mild winters ($10^{o}$C-$20^{o}$C) and hot summers (>$20^{o}$C). Central Spain, central Portugal, southern France, Italy, and Greece have cool winters ($0^{o}$C-$10^{o}$C) and hot summers (>$20^{o}$C). Northern Spain, northern Portugal, France (except the southern part), and England have cool winters ($0^{o}$C-$10^{o}$C) and mild summers ($10^{o}$C-$20^{o}$C). The cool winters are due to the dominating cyclonic activity in these countries dur-

ing this season. The mild winters and hot summers are due to the dominating anticyclonic activity in these countries during these seasons.

Precipitation also agrees with the general circulation previously described. Precipitation is fairly evenly distributed and most of the lowlands in Europe receive in average less than 500-750 mm per year[1], with the majority falling during winter time due to the strongly developed cyclonic activity. There are, however, discrepancies in the local maxima and minima due to seasonal and orographical reasons. Although precipitation generally maximizes during winter, there is higher precipitation due to convection on the westward sides of mountains like the Pyrenees, the Alps, and the Balkans[1]. Although precipitation generally minimizes in summer, there is some strong local minima on the leeside of these same mountain ranges[1]. These minima are very important in terms of biomass burning because they greatly enhance the fire risk. Average precipitation over western Europe between May 1 and October 31, the period corresponding to the fire season, is therefore particularly relevant and is shown in Figure 3.6. During this spell of time, southern Portugal receives less than 12 cm of rain, southern Spain, Sicily, and Greece receive between 12 cm and 25 cm of rain, northern Portugal, northern Spain, France, Italy, and Germany receive between 25 cm and 50 cm of rain, and Austria, and Yugoslavia receive between 50 cm and 100 cm of rain.

Another consequence of the general circulation is the cloud cover over western Europe. The cloudiness of the sky is related both to the amount of precipitation and to the temperature. The greater the cloud coverage is, the higher the precipitation is likely to be, and the less radiation reaches and warms up the earth. Averaged by season, the global distribution of the cloud cover with a $5^{o}$ by $5^{o}$ latitude-longitude resolution is found in the atlas NCAR/TN-273 +STR[3]. The period studied was 1971-1981[3]. Similar information is unfortunately not yet available for the following decade. For each season, the average

cloud cover for both northern and southern Europe is displayed in Table 3.1. For all seasons, the average cloudiness is less for southern Europe than for northern Europe with a minimum of 33% for southern Europe in summer, versus 62% in northern Europe, and a maximum of 73% in northern Europe in winter, versus 57% in southern Europe. These results agree with the predominant anticyclonic activity in summer over southern Europe, and the predominant cyclonic activity over northern Europe in winter.

Precipitation depends upon the type of cloud. Averaged by season, the most frequently occurring type of cloud with a $5^{o}$ by $5^{o}$ latitude-longitude resolution is also found in the atlas previously mentioned. The seasonal cloud type distribution over southern Europe is displayed in Table 3.2, whereas the seasonal cloud type distribution over northern Europe is displayed in Table 3.3. There are three main types of clouds: stratus clouds, which are layered clouds, cirrus clouds, which are fibrous clouds, and cumulus clouds, which are convective clouds[4]. The prefix alto indicates middle-level clouds (2-7 km). Stratus are the most common clouds in winter and autumn over northern Europe and in winter over southern Europe. They are associated with rising air and forecast the development of cyclones, dominating features of these periods of the year. The occluded front (Figure 3.2) is made of a warm front preceding a cold front. Ahead of the passage of the warm front, the rise of the air in the warm sector over the denser cold air produces clouds. First, cirrus clouds can be seen, and then, as the front moves closer, cirrostratus form and thicken to give altostratus. Finally, the latter lower toward the ground and form stratus clouds which bring rain[4]. In winter and autumn, occluded fronts follow each other, and therefore the most common clouds are stratus clouds. In summer and spring, both over northern and southern Europe, the dominating clouds are cirrus clouds. The depressions are not low enough to sweep through the continent because of the typically strong cyclonic activity over southern Europe. Therefore, the early stages of occluded fronts characterized by cirrus clouds are not followed by the stratus clouds which bring rain.

Some countries in Europe therefore experience both low summer precipitation and high summer temperatures: they are the mediterranean countries. Due to climatic conditions, these countries are then prone to more biomass burning than the northern European countries.

The vegetation in Europe can be classified into several ecosystems. Its distribution (Figure 3.8), is closely related to the climatic regions (Figure 3.5). Associated with the "mediterranean" or "dry summer subtropical climate" (<45$^{o}$ N) is the mediterranean vegetation with mixed forests composed of coniferous and deciduous trees. Associated with the "marine west coastal" climate (>45$^{o}$ N) are deciduous forests, coniferous forests and mixed forests. The few spots of dry climate in Spain are associated with grass.

Coniferous forests are composed of evergreen trees with needlelike leaves, such as fir, hemlock, pine, and spruce. Broad-leaved forests are composed of deciduous trees including oak, maple, and willow. The area of forests in western Europe, composed of the 21 countries in Table 3.4 is about 144 million hectares while the land area of these 21 countries is equal to about 467 million hectares. Therefore, about 31% of western Europe is forested, which is about the worldwide average (30%)[4]. These 144 million hectares split into 88 million hectares of coniferous forests and 56 million of broad-leaved forests, respectively 61% and 39% of the total (Table 3.5). The ratio of forested areas and the distribution of coniferous and broad-leaved forests varies in the countries of Europe. It is nevertheless consistent with the ecosystem distribution. In some countries like Ireland, Netherlands, and the United Kingdom, very few forests of any kind (<10% of the land area) exist. In other countries like Austria, Czechoslovakia, Finland, Portugal, and Sweden, the forested areas exceed the worldwide average 30% of the total land area. The ratio of coniferous forests to broad-leaved forests depends upon the countries. In northern European countries like Austria, Czechoslovakia, Finland, Germany, Ireland, the Netherlands,

Norway, Poland, Sweden, Switzerland and the United Kingdom, coniferous forests predominate over broad-leaved forests. This corresponds to the northern type of forests composed of a few different species with a high growing stock volume for timber, sawn wood and paper[4]. In southern European countries like France, Greece, Italy, Portugal, Spain and Yugoslavia, broad-leaved forests are more abundant than coniferous forests. This corresponds to the southern type of vegetation. The latter also includes shrublands with a role of conserving water, preventing soil erosion, and sheltering grazing herds[4].

TABLE 3.1

CLOUDINESS DISTRIBUTION (%) IN WESTERN EUROPE BY SEASON

| Countries | Winter | Spring | Summer | Autumn |
|---|---|---|---|---|
| Northern Europe | 73 | 64.3 | 62 | 67.8 |
| Southern Europe | 57 | 53.6 | 33.1 | 45.8 |

Source: Global distribution of total cloud cover and cloud type amounts over land[3].

TABLE 3.2

CLOUD TYPE DISTRIBUTION (%) IN SOUTHERN EUROPE BY SEASON

| Seasons | Stratus | Cirrus | Altostratus | Cumulus |
|---|---|---|---|---|
| Winter | 10 | 3 | 1 | 0 |
| Spring | 6 | 7 | 1 | 0 |
| Summer | 6 | 5 | 1 | 2 |
| Autumn | 4 | 7 | 3 | 0 |

Source: Global distribution of total cloud cover and cloud type amounts over land[3].

TABLE 3.3

CLOUD TYPE DISTRIBUTION (%) IN NORTHERN EUROPE BY SEASON

| Seasons | Stratus | Cirrus | Altostratus | Cumulus |
|---|---|---|---|---|
| Winter | 18 | 0 | 1 | 0 |
| Spring | 4 | 14 | 1 | 0 |
| Summer | 5 | 11 | 3 | 0 |
| Autumn | 17 | 1 | 1 | 0 |

Source: Global distribution of total cloud cover and cloud type amounts over land[3].

TABLE 3.4

LAND AND FORESTED AREAS (1000 HA) IN WESTERN EUROPE

| Country | Total area | Forest area | Ratio of forests (%) |
|---|---|---|---|
| Austria | 8385 | 3857 | 46 |
| Belgium | 3057 | 602 | 19.7 |
| Bulgaria | 11100 | 3314 | 29.8 |
| Czechoslov. | 12789 | 4491 | 35.1 |
| Finland | 30464 | 20059 | 65.8 |
| France | 54919 | 14440 | 26.2 |
| Germany | 35562 | 9828 | 27.6 |
| Greece | 13204 | 2034 | 15.4 |
| Hungary | 9300 | 1684 | 18.1 |
| Ireland | 6889 | 380 | 5.5 |
| Italy | 30126 | 8675 | 28.8 |
| Netherlands | 4147 | 311 | 7.5 |
| Norway | 30686 | 8435 | 27.5 |
| Poland | 31270 | 8654 | 27.7 |
| Portugal | 8800 | 3372 | 38.3 |
| Romania | 23750 | 6244 | 26.3 |
| Spain | 50471 | 11792 | 23.4 |
| Sweden | 40800 | 23700 | 58.1 |
| Switzerland | 4129 | 1186 | 28.7 |
| U.K. | 24100 | 2200 | 9.1 |
| Yugoslavia | 33262 | 8960 | 26.9 |
| EUROPE | 467210 | 144218 | 30.9 |

Source: Forest Condition in Europe: Executive Summary of the 1992 Report[5]

TABLE 3.5

CONIFEROUS AND BROAD-LEAVED FORESTS (1000 HA) IN WESTERN EUROPE

| Country | Coniferous forests | Ratio of coniferous forests (%) | Broad-leaved forests | Ratio of broad-leaved forests (%) |
|---|---|---|---|---|
| Austria | 2922 | 76 | 935 | 24 |
| Belgium | 302 | 50 | 300 | 50 |
| Bulgaria | 1172 | 35 | 2142 | 65 |
| Czechoslov. | 2891 | 64 | 1600 | 36 |
| Finland | 18484 | 92 | 1575 | 8 |
| France | 4840 | 34 | 9600 | 66 |
| Germany | 6927 | 70 | 2901 | 30 |
| Greece | 954 | 47 | 1080 | 53 |
| Hungary | 264 | 16 | 1420 | 84 |
| Ireland | 334 | 88 | 46 | 12 |
| Italy | 1735 | 20 | 6940 | 80 |
| Netherlands | 208 | 67 | 103 | 33 |
| Norway | 7700 | 91 | 735 | 9 |
| Poland | 6895 | 80 | 1759 | 20 |
| Portugal | 1340 | 40 | 2032 | 60 |
| Romania | 1929 | 31 | 4315 | 69 |
| Spain | 5637 | 48 | 6155 | 52 |
| Sweden | 19400 | 82 | 4300 | 18 |
| Switzerland | 818 | 69 | 368 | 31 |
| U.K. | 1550 | 70 | 650 | 30 |
| Yugoslavia | 1894 | 21 | 7066 | 79 |
| EUROPE | 88196 | 61 | 56022 | 39 |

Source: Forest Condition in Europe: Executive Summary of the 1992 Report[5]

FIGURE 3.1

TYPICAL 500 MB CONTOUR MAP OVER WESTERN EUROPE

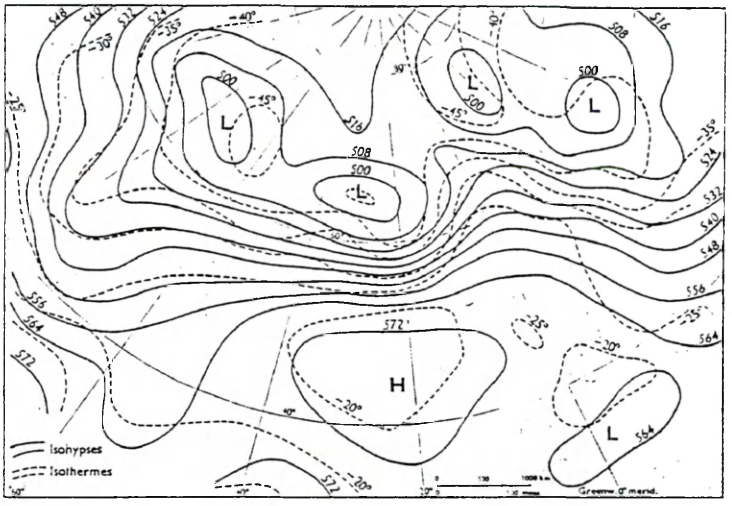


FIGURE 3.2

TYPICAL EARTH'S SURFACE CONTOUR MAP OVER WESTERN EUROPE

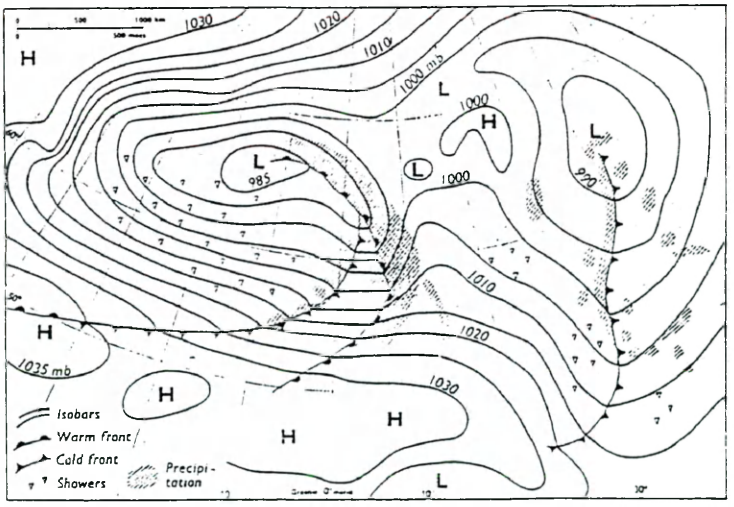

FIGURE 3.3

ATYPICAL 500 MB CONTOUR MAP OVER WESTERN EUROPE

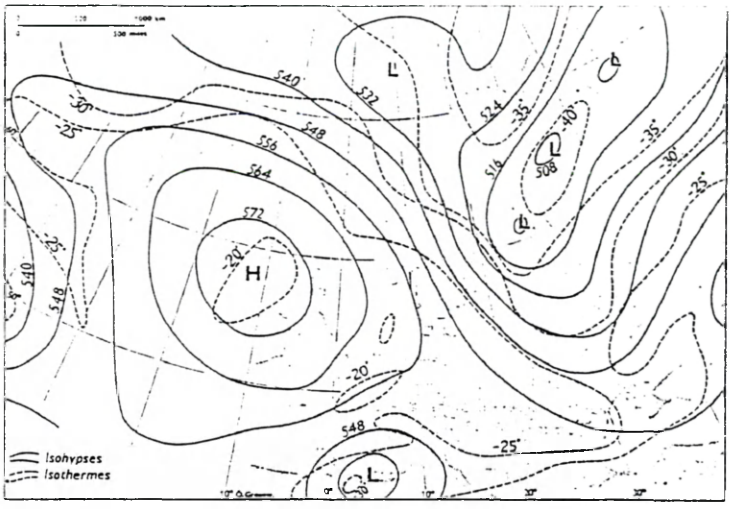


FIGURE 3.4

ATYPICAL EARTH'S SURFACE CONTOUR MAP OVER WESTERN EUROPE

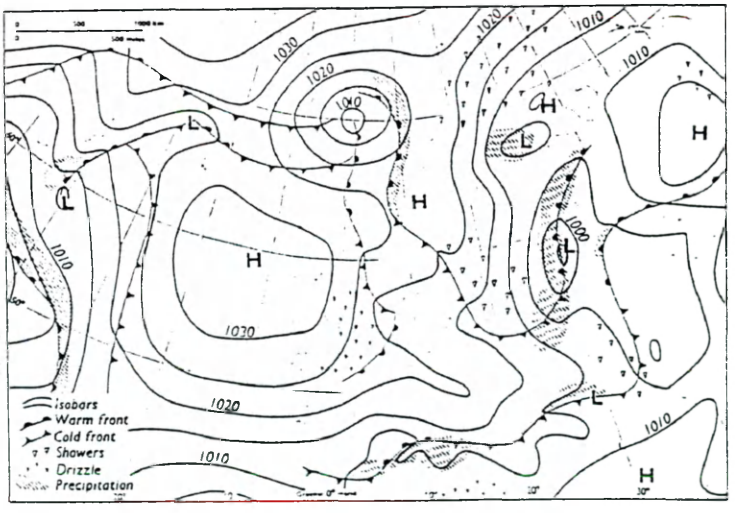

FIGURE 3.5

CLIMATIC REGIONS IN WESTERN EUROPE

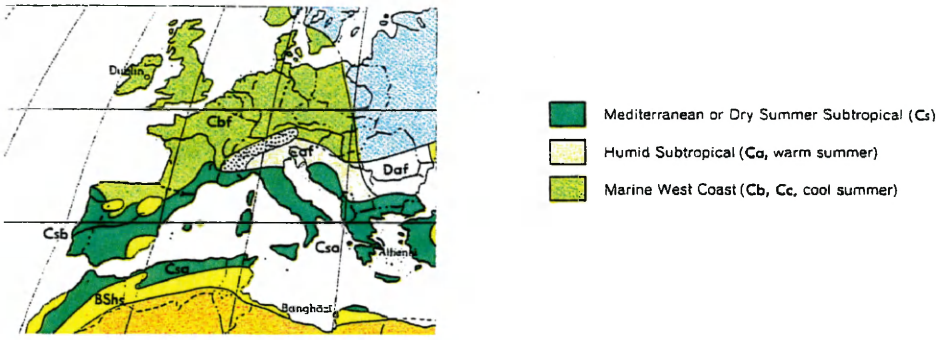


FIGURE 3.6

PRECIPITATION (MAY 1 TO OCTOBER 31) IN WESTERN EUROPE

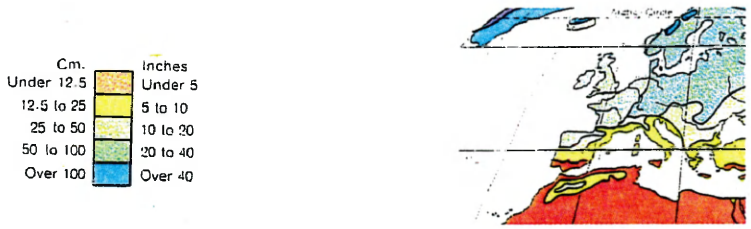


FIGURE 3.7

SURFACE TEMPERATURES IN WESTERN EUROPE

# FIGURE 3.8

## VEGETATION DISTRIBUTION IN WESTERN EUROPE

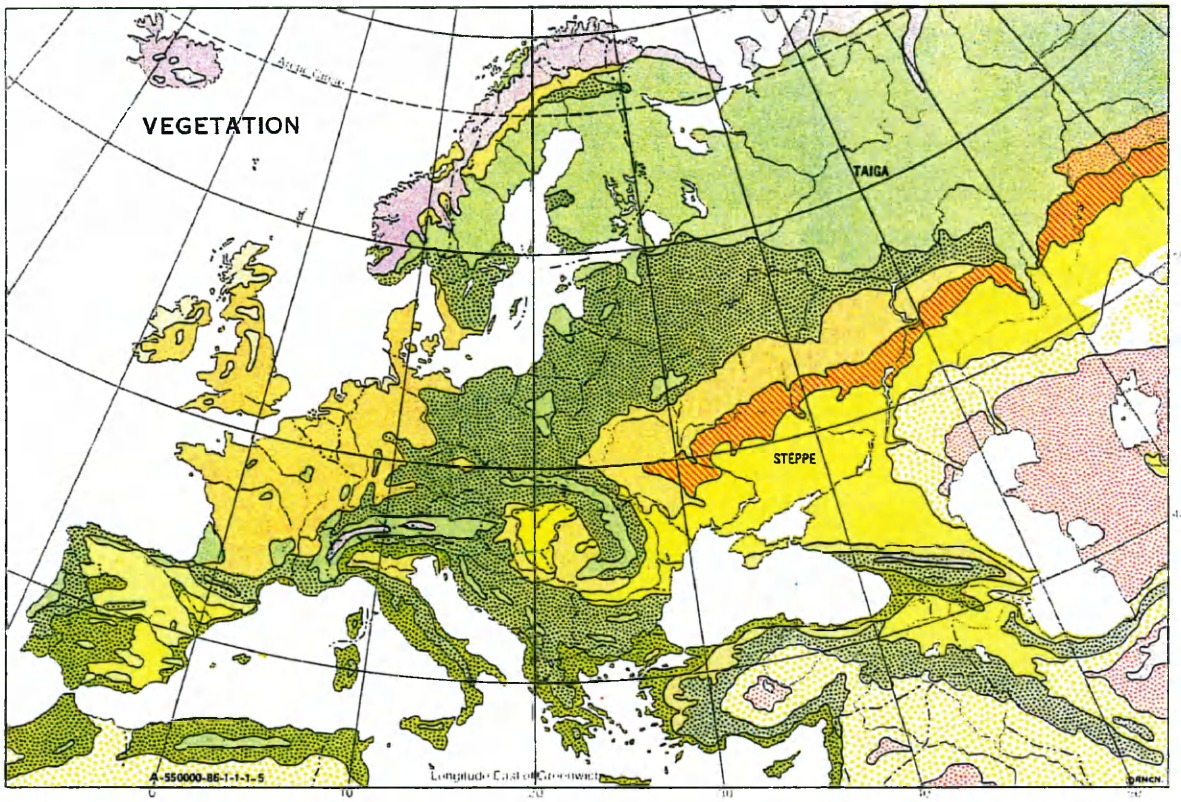


**VEGETATION**

- E — Coniferous forest
- M — Mediterranean vegetation
- M — Mixed forest: coniferous-deciduous
- S — Semi-deciduous forest
- D — Deciduous forest
- DG — Wooded steppe
- G — Grass (steppe)
- Gp — Short grass
- Dsp — Desert shrub
- L — Heath and moor
- L — Alpine vegetation, tundra
- b — Little or no vegetation

## NOTES TO CHAPTER III

1. Wallen, C., C. Climates of northern and western Europe.

2. Goode's World Atlas. 18th edition, Rand Mc Nally, 1992.

3. Warren, S., G., Hahn, C., J., London, J., Chervin, R., M., Jenne, R., L. Global distribution of total cloud cover and cloud type amounts over land. NCAR/TN-273+STR, 1986.

4. Wallace, J., M., Hobbs, P., V. Atmospheric Science: an introductory survey. Academic Press, 1977.

5. Forest Condition in Europe: Executive Summary of the 1992 Report. Economic and Social Council, EB.AIR/R.71, United Nations, New York, 1992.

# CHAPTER IV

# FOREST FIRES AND TRACE GAS ESTIMATES

Statistics of forest fires in Europe are computed every year by the United Nation's Economic Commission for Europe and the United Nation's Food and Agriculture Organization (FAO). The data used in the tables 4.1, 4.3, 4.4, 4.5, 4.6, 4.7, 4.8, and 4.10, comes from the Forest Fire Statistics 1985-1988 Report[1]. The data used in Table 4.9 comes from the Executive Summary of the 1992 Report on Forest Condition in Europe[2], whereas the data used in Table 4.2 comes from Goode's World Atlas[3].

The average area of forests and other lands burned in Europe over the period 1977-1987 is about 580 000 hectares (Table 4.1). The corresponding figure for 1987, year of interest in this study, is about 450 000 hectares. The year 1987 was not therefore particularly bad in western Europe in terms of biomass burning because the amount is under average. On the other hand, in the two previous years (1985 and 1986), western Europe experienced many more fires, especially in 1985 when the area burned was about twice the yearly average. In 1985, biomass burning in western Europe was therefore particularly severe.

In 1987, the amount of biomass burned in western Europe was one half of the total burned in Canada and one fourth of the total burned in the United States (Table 4.1). Since the total land area of Canada and of the United States are each twice as large as the European one (Table 4.2), the amount of burning in western Europe in 1987 was therefore proportionally as important as that in Canada and half as important as that in the United

States. However, since annual biomass burning is a highly variable phenomenon, the eleven year average may be used to draw a general conclusion. The 1977-1987 average area burned in western Europe is about half the average one in the United States and about one fourth the average one in Canada (Table 4.1). Considering the land areas of Canada, the United States and western Europe (Table 4.2), then the average amount of burning in western Europe is proportionately as important as in the United States and half as important as in Canada. The amount of burning in western Europe should therefore be studied because it is of comparable magnitude with the burning in the United States and in Canada.

In 1987, 432 977 hectares burned in the 24 countries of western Europe (Table 4.3). The total land area of the 24 countries is about 467 million hectares. In 1987 about one thousandth of the total land area burned. The number and area of fires depend upon the countries. Some countries have more or less forested areas and some countries get more or less precipitation. The six countries in western Europe, where the majority of the burning takes place are Spain with 33% of the total, Italy with 22%, Portugal with 17%, Greece with 10%, Yugoslavia with 5.5% and France with 2.3%. The other countries account each for less than 1% of the total amount. All the countries accounting for more than 1% of the total have a common denominator: they are located in the mediterranean region of Europe, where the climate is "mediterranean" or "dry summer tropical" (Chapter III).

Spain, Italy, Portugal, and Greece account for 87% of the total burning in western Europe and therefore should be separated from all the other countries. Biomass burning in these four countries will be discussed further in detail. Because year to year differences can be important, it is relevant to examine the fire statistics for these four countries over the eleven year period 1977-1987. It turns out that 1987 was not a bad year in terms of the

area burned in these four countries (Table 4.4). The 1987 amount is under average for each country except for Greece and Portugal which are slightly above average. Over the eleven year period, these four countries nevertheless still account for the majority of the burning in western Europe. Each year, the spatial distribution of the burning is similar.

The area burned can be separated into "forests & woodlands", and "other land" (Table 4.5). In Portugal, Spain and Greece, most of the burning occurs in the "forests & woodlands" category, unlike Italy, where the majority of the burning occurs in the "other land" category. Altogether, the "forests & woodlands" category, in these four countries, accounts for 63% of all the burning in Europe.

Even though the majority of the fires in Spain, Italy, and Greece have known causes (Table 4.6), the number of fires with unknown causes remains quantitatively important. Among the known causes are arson, negligence (agricultural operations, logging, prescribed forests fires, communications, industrial activities), and natural causes like lightning[3]. Since among the known causes arson is the most important in all the four countries, except in Greece (Table 4.6), it is estimated that arson is responsible for the majority of the fires with unknown causes. Table 4.7 displays the extent of the areas burned in terms of causes. In Spain and Italy, the extent of the burning attributed to known causes is greater than the extent of burning attributed to unknown causes. This just shows that the average area per fire due to known causes in Spain and Italy is greater that the average size of a fire due to unknown causes (Table 4.8). This last table shows the average area per fire depending upon the cause of the fire. Table 4.8 is obtained from the figures in the Tables 4.6 and 4.7.

Now it is important to study the distribution of the burning as a function of the ecosystem in the four countries which account for the majority of the burning in western

Europe. Each ecosystem has indeed different amounts of organic matter per unit area, different amounts of above ground biomass, and different burning efficiencies (Seiler and Crutzen)[5]. In consequence, each ecosystem releases to the atmosphere trace gases in different quantities. Table 4.9 contains the same information as Table 3.4, but just for Spain, Italy, Portugal, and Greece.

Table 4.10 displays the distribution of the area burned in terms of the type of vegetation. The amount of area burned for "other land" is greater than the sum of coniferous and broad-leaved forests and coppice for Spain, Greece, and Italy. Coppice, a closed forest composed of stool-shoots or root suckers with or without scattered trees of seedling origin[3], can be associated with the shrubform vegetation also called chaparral. "Other land" defines land which, although not falling within the definition of forest and other wooded land, has nonetheless been included in national forest fire statistics[3].

The goal of computing the average area of the fire according to the cause is to find out whether the cause of the fire has an influence upon the average size. In the case of Spain, Italy, and Portugal, the averages for fires caused by known and unknown reasons are similar to the total average. For Greece, the average size of a fire can greatly vary depending upon the cause (from 19.9 hectares for natural causes to 53.3 hectares for unknown causes, Table 4.8). This latter high average figure suggests that some fires are much larger than the average half a square kilometer in Greece. These numbers are important because remote sensing accuracy depends upon the size of the fires (Chapter V).

At this point, the fire statistics for the western European countries in 1987 and the major ecosystems in this part of the world are known. The mass of dry matter burned in western Europe can therefore be estimated with this information for the year 1987. It indeed depends upon the ecosystem where the burning takes place. Seiler and Crutzen[5]

estimate the mass of dry matter burned per year to:

$$M = AB\alpha\beta \qquad \text{Equation4a}$$

where A is the area burned ($m^2$), B is the average amount of dry matter per unit area in grams (g dm/$m^2$), $\alpha$ is the fraction of average above-ground biomass, and $\beta$ is the burning efficiency of the above-ground biomass. B, $\alpha$, and $\beta$ vary upon the ecosystems. Seiler and Crutzen[5] have estimated these coefficients for most ecosystems (Table 4.11). These coefficients differ slightly for deciduous and coniferous forests and the value of $\beta$ has been chosen for wildfires[5] since there are almost no prescribed fires in western Europe. According to Seiler and Crutzen[5], the burning efficiency is the most difficult figure to estimate because it can locally vary with particular weather conditions like wind, temperature, and air humidity. Moreover, in Europe, fires are usually put out as soon as possible. It is therefore estimated that the burning efficiency is 20% for wildfires whereas its counterpart for prescribed fires in temperate forests is 30% (Seiler and Crutzen)[5]. The only missing figure in Table 4.11 was the burning efficiency for shrubland. Since Seiler and Crutzen[5] estimate the burning efficiency for savannas to be as high as 80%, a similar figure can be used for shrublands because of the similarity of the two ecosystems.

In order to come up with an estimate for the mass of dry matter burned in Europe, an average biomass of 35 kg.$m^2$ is used (Seiler and Crutzen[5]). It is the average of the organic matter figures per unit area for deciduous and coniferous forests. The fraction of average above-ground biomass and the burning efficiency are those in Table 4.11. The total area of fires in western Europe in 1987 is 432 977 ha (Table 4.3). Equation 4a yields a mass of dry matter burned equal to 22.7 Tg dm (1 Tg = $10^{12}$ g). This figure will be used later in this chapter to estimate the total trace gas emissions in western Europe in 1987.

In a previous paragraph, a detailed study of the area burned in terms of ecosystems has been carried out in the four mediterranean countries which are the main contributors to the burning in Europe. Using these figures (Table 4.10), the mass of dry matter burned can be estimated for these four countries. The area burned was separated into four types of vegetation which are: coniferous forests, deciduous forests, coppice and "other land". Table 4.12 gives B, $\alpha$, $\beta$, and their product for these four types of vegetation. When multiplying these terms by the corresponding areas, the estimates of the mass of dry matter burned come out to: 6.1 Tg dm in Spain, 3.9 Tg dm in Portugal, 5.7 Tg dm in Italy and 1.9Tg dm in Greece. These figures are summarized in Table 4.13. The mass of dry matter burned is an important number because it is proportional to combustion gas estimates, which is one of the goals of this study. The principles of combustion chemistry that were discussed in Chapter II will be presently applied.

The dry biomass matter previously estimated in Europe consists of about 45% of carbon by weight (Levine)[6]. Then, the mass of carbon (M(C)) released by fires in western Europe is 10.2 Tg C ($10^{12}$ g of carbon). Among all the carbon containing particles in the plumes, carbon dioxide accounts for about 90% of the total mass of carbon and carbon monoxide accounts for about the remaining 10% (Levine)[6]. Then, the mass of $CO_2$ produced by forest fires in western Europe in 1987 is 9.2 Tg C and the mass of CO is 1.02 Tg C. The amount of $CO_2$ emitted is important since all the trace gas emission ratios will be expressed in terms of this quantity. These two last operations can be applied to the mass of dry matter burned in the four mediterranean countries previously mentioned and the corresponding results are shown in Table 4.13. In Spain, the major burning country of western Europe, the 6.1 Tg dm of dry biomass burned in 1987 yielded an amount of carbon released to the atmosphere of 2.75 Tg C. The latter is divided into the $CO_2$ emissions (2.47 Tg C) and the CO emissions (0.27 Tg C). It is now relevant to compare these $CO_2$ emissions with the industrial emissions in the top $CO_2$ emitting countries in western Europe.

The industrial emissions have different sources[7] (solid, liquid and gas fossil fuels, cement production, and gas flaring) and the five top $CO_2$ emitters are the former Federal Republic of Germany, the United Kingdom, Italy, France, and Spain. These five countries contribute 73% of the total regional $CO_2$ emissions[7]. In 1987, the total of $CO_2$ emitted in western Europe was 795 Tg C[7]. This figure is to be compared to the 9.2 Tg C of $CO_2$ emitted by biomass burning during this particular year. Biomass burning therefore represented in 1987 about 1.2% of the total $CO_2$ emissions in western Europe.

While this is a rather low percentage, it must be kept in mind that western Europe is an extensively industrialized region of the world. For Spain and Italy, the only two countries belonging, at the same time, to the five top industrial $CO_2$ emitters, as well as to the four top biomass burning contributors in western Europe, the results are shown in Table 4.14. In Spain, the 2.47 Tg C of $CO_2$ emitted by biomass burning represented about 5% of the 48 Tg C of total $CO_2$ emissions in this same country and in Italy, the 2.31 Tg C of $CO_2$ emitted by biomass burning represented about 2% of the 99.2 Tg C of the total $CO_2$ emissions in this same country.

The total $CO_2$ emissions for Portugal and Greece are not provided in the compendium[7] because they do not belong to the five top emitters. It can nevertheless be estimated that the ratio of $CO_2$ emissions by biomass burning to the total emissions will be much greater for these two countries than those previously mentioned because they have high $CO_2$ emissions due to biomass burning and low industrial $CO_2$ emissions.

In 1985, an exceptionally bad year in terms of fires (twice the average), the $CO_2$ emissions by biomass burning in western Europe were of 22.5 Tg C (Table 4.18), instead of 9.2 Tg C for 1987. As for industrial $CO_2$ emissions for this same year, they amounted to 803 Tg C[7]. Biomass burning therefore accounted for 2.8% of the industrial $CO_2$ emissions

in 1987. $CO_2$ emissions due to biomass burning can thus vary between 1% and 3% of the industrial emissions per year.

The amount of carbon dioxide emitted permits us to find out the amount of trace gases released to the atmosphere during biomass burning[6]. In order to carry out these estimates, emission ratios (ER) of the trace gases in the plumes are defined. The emission ratio of a trace gas relates to its own concentration and to the concentrations of $CO_2$, both in and out the plume. This relation is summarized in the following equation[6]:

$$ER = \frac{\Delta X}{\Delta CO_2} = \frac{(X)_{plume} - (X)_{background}}{(CO_2)_{plume} - (CO_2)_{background}} \qquad \text{Equation4b}$$

where (X) and ($CO_2$) are the concentrations in the plume and out of the plume (background), $\Delta X$ is the concentration of the trace gas X produced by biomass burning and $\Delta CO_2$ is the concentration of $CO_2$ produced by biomass burning.

The emission ratio of a particular gas depends upon the ecosystems, i.e., moisture, composition, and burning efficiency. Radke et al.[8] provide estimates for ecosystems in North America. The trace gas emissions from 17 fires in the temperate zone of northern America (34° N - 49° N) have been studied[8]. Out of the 17 fires, 14 occurred in coniferous forests and 3 in a chaparral environment (equivalent to the mediterranean vegetation). These ecosystems are very similar to the European ones and the latitude range corresponds exactly to that of western Europe. The available figures for northern American fires will therefore approximate the European situation. The average of the trace gas emissions for all 17 fires will be used in this study. Therefore no distinction will be made between the emissions from deciduous, coniferous, and mediterranean forests. The trace emission factors for the most important trace gases produced during the burning of temperate forests are shown in Table 4.15. The standard deviation is relatively high for ozone

($O_3$), ammonia ($NH_3$), and for the nitrogen oxide family ($NO_x$=NO+$NO_2$). The following estimations concerning these gases are therefore subject to large uncertainties. From the data in Table 4.15, the emission ratios for the corresponding trace gases can be estimated by using Equation 4b. The results are summarized in Table 4.16. Since carbon dioxide is the normalizing factor, the flux of the various trace gases due to biomass burning in western Europe can be estimated for the year 1987 by using the mass of $CO_2$ released in 1987 by biomass burning in Table 4.14, that is 9.2 Tg C. The results show up in Table 4.16. The total amount of CO released in western Europe comes out to 0.463 Tg C when using the average emission ratio calculated from the data provided by Radke et al.[8].

These particular amounts for the year 1987 should be compared to the annual average fluxes of the same trace gases in the world, data provided by Andreae[9]. That is done in Table 4.17. The amount of $CO_2$ produced by biomass burning in Europe is about 0.3% of the total amount emitted by biomass burning around the world. This confirms that 1987 was not a bad year in terms of fires in western Europe unlike in the rest of the world. For all the other trace gases the ratio is less than or equal to 0.1%. On a global scale, biomass burning in western Europe is negligible.

Since in western Europe the 11 year average area burned (586 467 ha) is slightly greater than the 1987 figure (432 977 ha), then the 11 year average mass of dry biomass burned and mass of carbon released to the atmosphere go up by 35% and are equal respectively to 30.6 Tg dm and 13.8 Tg dm (Table 4.18). In 1985, an exceptionally bad year in terms of fires (i.e., many fires), all the previously cited figures were 144% higher than those in 1987. The total area burned was indeed 1 058 342 ha (Table 4.1). The amount of $CO_2$ released to the atmosphere went up to 22.5 Tg C (Table 4.18). This represents 0.64% of the total annual average flux in the world estimated by Andreae[9]. Therefore even a bad year accounts for less than 1% of the total $CO_2$ emissions produced by biomass burning.

TABLE 4.1

TOTAL AREA BURNED IN CANADA, USA, AND EUROPE

| Year | Canada | United States | Europe |
|---|---|---|---|
| 1977 | 1438174 | 1172999 | 362971 |
| 1978 | 289413 | 710068 | 763513 |
| 1979 | 2700748 | 1033481 | 589264 |
| 1980 | 4822167 | 1254080 | 541242 |
| 1981 | 5413365 | 1691775 | 768453 |
| 1982 | 1697591 | 579545 | 451109 |
| 1983 | 1194175 | 793500 | 504655 |
| 1984 | 765382 | 1229887 | 397159 |
| 1985 | 757260 | 2125529 | 1058342 |
| 1986 | 950123 | 1291448 | 581454 |
| 1987 | 1085629 | 2017058 | 432977 |
| Total | 21114027 | 13899370 | 6451139 |
| Average | 1919457 | 1263579 | 586467 |

Source: Forest Fire Statistics 1985-1988[1]

TABLE 4.2

LAND AREAS (1000 SQ MILES) IN CANADA, USA, AND WESTERN EUROPE

| Country | Land area |
|---|---|
| USA | 3787 |
| Canada | 3850 |
| Europe | 1800[a] |

a. 467210000 ha = 1800000 sq miles

Source: Goode's World Atlas[3]

TABLE 4.3

Source: Forest Fire Statistics 1985-1988[1]

| Country | # fires | Area (ha) | Average area (ha) | % of the total area |
|---|---|---|---|---|
| Austria | 98 | 53 | .54 | <1 |
| Belgium | 95 | 114 | 1.20 | <1 |
| Bulgaria | 76 | 508 | 6.68 | <1 |
| Cyprus | 62 | 1550 | 25.00 | <1 |
| Czechoslov. | 249 | 265 | 1.06 | <1 |
| Finland | 285 | 153 | .54 | <1 |
| France | 2115 | 10393[a] | 4.91 | 2.32 |
| G.D.R | 609 | 466 | .77 | <1 |
| F.R.G | 484 | 319 | .66 | <1 |
| Greece | 1266 | 46315 | 36.58 | 10 |
| Hungary | 393 | 1349 | 3.43 | <1 |
| Ireland | 721 | 840 | 1.17 | <1 |
| Italy | 11972 | 120697 | 10.08 | 27 |
| Netherlands | 90 | 115 | 1.28 | <1 |
| Norway | 286 | 335 | 1.17 | <1 |
| Poland | 1222 | 1454 | 1.19 | <1 |
| Portugal | 6977 | 76268 | 10.93 | 17 |
| Romania | 52 | 172 | 3.31 | <1 |
| Spain | 8679 | 145793 | 16.80 | 33 |
| Sweden | 117 | 899 | 7.68 | <1 |
| Switzerland | 113 | 199 | 1.76 | <1 |
| U.K. | 384 | 157 | .41 | <1 |
| Yugoslavia | 1108 | 24563 | 22.17 | 5.5 |
| EUROPE | 37453 | 432977 | 11.56 | 100 |

a. In the mediterranean region alone.

TABLE 4.4

TOTAL AREA BURNED (HA) IN SPAIN, ITALY, PORTUGAL, AND GREECE FROM 1977 TO 1987

| Year | Spain | Italy | Portugal | Greece |
|---|---|---|---|---|
| 1977 | 67540 | 92739 | N/A | 53763 |
| 1978 | 434868 | 127577 | 97345 | 20002 |
| 1979 | 271718 | 114930 | 66330 | 21180 |
| 1980 | 265954 | 144302 | 44260 | 32965 |
| 1981 | 298436 | 242218 | 89797 | 81417 |
| 1982 | 151644 | 130239 | 39557 | 27372 |
| 1983 | 117599 | 223728 | 47812 | 19613 |
| 1984 | 164546 | 78326 | 52713 | 33655 |
| 1985 | 486327 | 189898 | 146255 | 105450 |
| 1986 | 277071 | 86420 | 99522 | 24514 |
| 1987 | 145793 | 120697 | 76268 | 46315 |
| Total | 2681496 | 1551074 | 759859 | 466246 |
| Average | 243772 | 141007 | 75986 | 42386 |

Source: Forest Fire Statistics 1985-1988[1]

TABLE 4.5

AREA BURNED (HA) ON FORESTS AND OTHER LANDS IN SPAIN, ITALY, PORTUGAL, AND GREECE IN 1987

| Country | Total | Forests & woodlands | Other lands |
|---|---|---|---|
| Spain | 145793 | 122270 (84%) | 23523 (16%) |
| Portugal | 76268 | 73934 (97%) | 2334 (3%) |
| Italy | 120697 | 48484 (40%) | 72213 (60%) |
| Greece | 46315 | 37271 (80%) | 9044 (20%) |

Source: Forest Fire Statistics 1985-1988[1]

TABLE 4.6

NUMBER OF FIRES BY CAUSES IN SPAIN, ITALY, PORTUGAL, AND GREECE IN 1987

| Country | Total | Known causes | Arson | Negligence | Natural causes | Unknown causes |
|---|---|---|---|---|---|---|
| Spain | 8679 | 4845 | 3284 | 1186 | 375 | 3834 |
| Italy | 7675 | 6920 | 4099 | 2791 | 30 | 755 |
| Portugal | 6977 | 501 | 305 | 162 | 34 | 6476 |
| Greece | 1266 | 817 | 204 | 554 | 59 | 449 |

Source: Forest Fire Statistics 1985-1988[1]

TABLE 4.7

AREA (HA) BURNED BY CAUSES IN SPAIN, ITALY, PORTUGAL,

AND GREECE IN 1987

| Country | Total | Known causes | Arson | Negligence | Natural causes | Unknown causes |
|---|---|---|---|---|---|---|
| Spain | 145793 | 83394 | 57499 | 21845 | 4050 | 62399 |
| Italy | 48484 | 44932 | 33089 | 11759 | 84 | 3552 |
| Portugal | 76268 | 7371 | 5399 | 1787 | 185 | 68897 |
| Greece | 46315 | 22384 | 4631 | 16580 | 1173 | 23931 |

Source: Forest Fire Statistics 1985-1988[1]

TABLE 4.8

AVERAGE FIRE AREA (HA) BY CAUSES IN SPAIN, ITALY, PORTUGAL,

AND GREECE IN 1987

| Country | Total | Known causes | Arson | Negligence | Natural causes | Unknown causes |
|---|---|---|---|---|---|---|
| Spain | 16.8 | 17.2 | 17.5 | 18.4 | 10.8 | 16.3 |
| Italy | 6.3 | 6.5 | 8.1 | 4.2 | 2.8 | 4.7 |
| Portugal | 10.9 | 14.7 | 17.7 | 11.0 | 5.4 | 10.1 |
| Greece | 36.6 | 27.4 | 22.7 | 29.9 | 19.9 | 53.3 |

Source: Forest Fire Statistics 1985-1988[1]

TABLE 4.9

FORESTED AREAS BY SPECIES IN SPAIN, ITALY, PORTUGAL, AND GREECE

| Country | Surface | High forest | Coniferous forest | Broad-leaved forest |
|---|---|---|---|---|
| Spain | 50471 | 11792 | 5637 | 6155 |
| Portugal | 8800 | 3372 | 1340 | 2032 |
| Italy | 30126 | 8675 | 1735 | 6940 |
| Greece | 13204 | 2034 | 954 | 1080 |

Source: Forest Condition in Europe: Executive summary of the 1992 Report[2]

TABLE 4.10

BURNED AREAS BY SPECIES IN SPAIN, PORTUGAL, ITALY,

AND GREECE IN 1987

| Country | Coniferous forest | Broad-leaved forest | Coppice | Other land |
|---|---|---|---|---|
| Spain | 29853 | 19040 | 10582 | 62795 |
| Portugal | 41866 | 2257 | 4308 | 25503 |
| Italy | 11562 | 10181 | 26741 | 72213 |
| Greece | 9912 | 3692 | 4322 | 19345 |

Source: Forest Fire Statistics 1985-1988[1]

TABLE 4.11

AMOUNT OF DRY MATTER (B), FRACTION OF ABOVE GROUND BIOMASS (α), AND BURNING EFFICIENCY (β), BY SPECIES

| Coefficients | Deciduous and Broad-leaved forests | Coniferous forests | Shrubland |
|---|---|---|---|
| B ($kg.m^{-2}$) | 33 | 38 | 7 |
| α (%) | 73 | 73 | 64 |
| β (%) | 20 | 20 | 75 |

Source: Seiler and Crutzen[5]

TABLE 4.12

PRODUCT Bαβ, BY ECOSYSTEM IN MEDITERRANEAN COUNTRIES

| Coefficients | Coniferous forests | Deciduous forests | Coppice | Other land |
|---|---|---|---|---|
| B ($kg.m^{-2}$) | 38 | 33 | 7 | 35 |
| α (%) | 73 | 73 | 64 | 73 |
| β (%) | 20 | 20 | 75 | 20 |
| Bαβ | 5.55 | 4.82 | 3.36 | 5.11 |

Source: Seiler and Crutzen[5]

TABLE 4.13

MASS OF DRY BIOMASS BURNED, CARBON AND $CO_2$ EMITTED BY BURNING IN SPAIN, ITALY, PORTUGAL, AND GREECE IN 1987

| Countries | M (Tg dm) | M(C) (Tg C) | M($CO_2$) (Tg C) |
|---|---|---|---|
| Spain | 6.1 | 2.75 | 2.47 |
| Portugal | 3.9 | 1.75 | 1.57 |
| Italy | 5.7 | 2.57 | 2.31 |
| Greece | 1.9 | 0.85 | 0.77 |

TABLE 4.14

BIOMASS BURNING AND INDUSTRIAL $CO_2$ EMISSIONS IN SPAIN, ITALY, PORTUGAL, AND GREECE IN 1987

| Country | $CO_2$ forest fire emission (Tg C) | $CO_2$ total emission (Tg C) | Ratio of forest fire emission to total emission (%) |
|---|---|---|---|
| Spain | 2.47 | 48 | 5.15 |
| Italy | 2.31 | 99.2 | 2.33 |
| western Europe | 9.2 | 795 | 1.16 |

TABLE 4.15

AVERAGE EMISSION FACTORS FOR TRACE GASES IN TEMPERATE FORESTS

| Species | $CO_2$ | CO | $O_3$ | $NH_3$ | $CH_4$ | $N_2O$ | $NO_x$ |
|---|---|---|---|---|---|---|---|
| EF | 1650±29 | 83±16 | 2.2±1.6 | 0.9±0.43 | 3.2±0.5 | 0.23±0.05 | 3.9±1.6 |

Source: Radke et al.[8]

TABLE 4.16

TRACE GASES FLUX IN WESTERN EUROPE IN 1987

| Species | Emission ratio[a] | Flux (Tg C) |
|---|---|---|
| CO | 0.05 | 0.463 |
| $O_3$ | 0.001 | 0.012 |
| $NH_3$ | 0.0005 | 0.005 |
| $CH_4$ | 0.002 | 0.018 |
| $N_2O$ | 0.0001 | 0.001 |
| $NO_x$ | 0.002 | 0.022 |

a. Source: Radke et al.[8]

TABLE 4.17

BIOMASS BURNING TRACE GASES FLUX IN THE WORLD

AND IN WESTERN EUROPE IN 1987

| Species | Annual average flux in the world (Tg C)[a] | Flux in western Europe (Tg C) in 1987 | Ratio of flux in Europe to flux in the world (%) |
|---|---|---|---|
| $CO_2$ | 3500 | 9.2 | 0.26 |
| CO | 350 | 0.463 | 0.13 |
| $CH_4$ | 38 | 0.018 | 0.05 |
| $NO_x$ | 8.5 | 0.022 | 0.03 |
| $NH_3$ | 5.3 | 0.005 | 0.01 |
| $O_3$ | 420 | 0.012 | 0.003 |

a. Andreae[9]

TABLE 4.18

MASS OF DRY BIOMASS BURNED, CARBON AND $CO_2$ RELEASED

BY BIOMASS BURNING IN WESTERN EUROPE IN 1985 AND 1987

| Year | M (Tg dm) | M(C) (Tg C) | M($CO_2$) (Tg C) |
|---|---|---|---|
| 1987 | 22.7 | 10.2 | 9.2 |
| Average 1977-87 | 30.6 | 13.8 | 12.4 |
| 1985 | 55.5 | 25 | 22.5 |

## NOTES TO CHAPTER IV

1. Forest Fire Statistics 1985-1988. Economic Commission for Europe, Food and Agriculture Organization, ECE/TIM/51, United Nations, New York, 1990.

2. Forest Condition in Europe: Executive Summary of the 1992 Report. Economic and Social Council, EB.AIR/R.71, United Nations, New York, 1992.

3. Goode's World Atlas. 18th edition, Rand Mc Nally, 1992.

4. Europe's green mantle: heritage and future of our forests. Commission of the European Communities, Newsletter on the Common Agricultural Policy, 1984, (n° 204).

5. Seiler, W. and P. J. Crutzen. Estimates of gross and net fluxes of carbon between the biosphere and the atmosphere from biomass burning. Climate Change, 2, 207-247, 1980.

6. Levine, J. S., Cofer III, W. R., Winstead, E. L., Rhinehart, R. P., Cahoon, Jr., D. R., Sebacher, D. I., Stocks, B. J. Global Biomass Burning: Atmospheric, Climatic, and Biospheric Implications. 264-271 Cambridge, Massachussets: MIT Press, 1991.

7. Trends'91 : a compendium of data on global change. Carbon Dioxide Information Analysis Center, ed. Boden, T. A., Sepanski, R. J., Stoss, F. W., December 1991.

8. Radke, L. F., Hegg, D. A., Hobbs, P. A., Nance, J. D., Lyons, J. H., Laursen, K. K., Weiss, R. E., Riggan, P. J., Ward, D. E. Global Biomass Burning : Atmospheric, Climatic, and Biospheric Implications. 209-224 Cambridge, Massachusset: MIT Press, 1991.

9. Andreae, M. O. Global Biomass Burning : Atmospheric, Climatic, and Biospheric Implications. 3-21 (Cambridge, Massachusetts: MIT Press, 1991.

# CHAPTER V

# FIRE MONITORING FROM SPACE

Remote sensing enables us to measure the reflected and emitted electromagnetic radiation (EMR) by the Earth from space. Properties of EMR, of materials on the Earth, and of the atmosphere are therefore important in understanding the principles of remote sensing.

EMR of a blackbody radiator (theoretical object that is a perfect absorber and emitter of EMR at all wavelengths) carries energy according to Planck's radiation law. This law relates the spectral characteristics and magnitude of the emission to the temperature of the emitting body. Unfortunately, in the reality, "blackbodies" do not exist. Real objects are called "graybodies" and their spectral emission is proportional to that of "blackbodies" at the same temperature with a factor ε, called emissivity. The relation is:

$$E_{gb} = \varepsilon E_{bb}$$

The expression of the EMR emitted by a "graybody" at any wavelength is therefore:

$$E_\lambda = \varepsilon \frac{C_1}{\lambda^5 \left(e^{(C_2/(\lambda T))} - 1\right)}$$

$E_\lambda$ is the spectral emission in $W/m^2.m$ at a wavelength $\lambda$ in meters.

T is the absolute temperature in degree Kelvin.

$C_1$ and $C_2$ are the first and second radiation constants.

$C_1 = 3.74\ 10^{-6}\ W.m^2$ and $C_2 = 1.44\ 10^{-2}\ m.K$

All bodies at a temperature T emit radiation depending upon the considered wavelength. This can be illustrated by the spectral distribution curves of blackbodies at different temperatures (Figure 5.1). The Sun with a surface temperature of about 6000°K has a much wider and more energetic emission curve than the Earth with an average temperature of 288°K. The total energy $E_{t,T}$, emitted by a "graybody" at a temperature T, is the sum of the emissions over the full electromagnetic spectrum and its expression is:

$$E_{t,T} = \varepsilon \int E_{\lambda,T} d\lambda$$

A simpler way to find out this quantity is to use the Stefan-Boltzmann law which says that the total emitted energy is proportional to the fourth power of the temperature:

$$E_{t,T} = \varepsilon \sigma T^4$$

$\sigma$ ($5.67\ 10^{-8}$ W/m$^2$.K$^{-4}$) is the Stefan-Boltzmann constant.
T is the temperature in degrees Kelvin and $\varepsilon$ is the emissivity.

Another feature in Figure 5.1 is the position of the maxima of the spectral emission curves. The Wien's displacement law relates the wavelength of the maximum energy to the temperature of the blackbody with the equation:

$$\lambda_{max} = \frac{W}{T}$$

W is the Wien's constant (W = 2897 μm.K) and T the temperature in degree Kelvin.

Therefore, for the Sun, the maximum energy wavelength is 0.48 μm and for the Earth it is 10.06 μm. The Sun's maximum radiation is in the visible range and the Earth's maximum radiation is in the infrared.

In the atmosphere, the EMR is subject to gaseous and aerosol absorption, and to scattering. The entire spectrum of the incident, reflected, and emitted EMR therefore interacts with gases in the atmosphere. Certain gases in the atmosphere indeed trap the incoming and outgoing radiation at selected wavelengths[1]. This absorption is due to vibrational and rotational transitions in the molecules. Four gases (oxygen ($O_2$), ozone ($O_3$), carbon dioxide ($CO_2$), and water vapor ($H_2O$), are responsible for most of the absorption and each of these gases absorbs at different wavelengths (Figures 5.2). In consequence, the solar irradiation curve at sea level differs from the solar radiation curve outside the atmosphere. The fraction absorbed ($I_{mol.absorption}$) can be quantified by Beer's law:

$$I_{mol \cdot absorption} = I_0 e^{-\tau_{mol \cdot absorption}}$$

$I_0$ is the EMR before absorption.

$\tau_{mol.absorption}$ is the optical density for absorption and is equal to:

$$\tau_{mol \cdot absorption} = \sum_{gas_i} N(gas_i)\, \sigma_{absorption}(gas_i)$$

with $gas_i$ being $O_2$, $O_3$, $CO_2$, and $H_2O$.

$N$ is the column density and $\sigma_{absorption}$ is the absorption cross-section.

$\sigma_{absorption}$ depends upon the wavelength.

The energy available for interactions with matter at the surface of the Earth is then divided into atmospheric windows separated by bands of atmospheric absorption (Figure 5.3). The major atmospheric windows are the visible window (0.4 mm - 0.7 mm) and several infrared windows like (0.8 μm - 0.9 μm), (1.0 μm - 1.1 μm), (1.2 μm - 1.3 μm), (1.5 μm - 1.7 μm), (2.0 μm - 2.5 μm), (3.3 μm - 4.1 μm), and (10 μm - 12 μm). Only radiation reflected and emitted in these windows can be measured by remote sensors in space. Fortunately enough, the visible reflected energy from the Sun and the Earth's emitted radiation are in these atmospheric windows.

EMR can also be scattered without being absorbed. There are two kinds of scattering: the Rayleigh scattering and the Mie scattering. The Rayleigh scattering (molecular scattering) of EMR at the wavelength $\lambda$ works for molecules of which the radius (r) verifies $\alpha << 1$ with:

$$\alpha = \frac{2\pi r}{\lambda}$$

On the other hand, the Mie scattering works for larger particles, that verify: $0.05 < \alpha < 50$. The intensity of the EMR scattered ($I_s$) is:

$$I_s = I_0 e^{-\tau_s}$$

$\tau_s$ is the optical density for scattering and is given by the expression:

$$\tau_s = \sum_i N(gas_i)\,\sigma_s(gas_i)$$

$N(gas_i)$ is the column density of the gas i and $\sigma_s$ is the scattering cross section of the gas i. The EMR is then scattered in all directions.

Remote sensing examines the ways in which material reflects and absorbs visible and infrared radiation from the Sun. Part of the shortwave radiation coming from the Sun is absorbed by the surface and heats up the Earth. Once heated, the surface reemits some of the energy as longwave or thermal radiation. Remote sensing then measures the sum of the reflected and emitted radiation by the Earth in different wavelength bands which correspond to atmospheric windows. To this reflected and emitted radiation must be added the back scattered radiation.

The emitted radiation from the Earth can be separated from the reflected solar radiation in certain channels. Since the solar radiation peaks in the visible band and since the emitted radiation from the Earth is negligible in the visible band because it peaks in the infrared band (Figure 5.1), then the visible band will only measure the reflected radiation by the Earth. Although the solar power (P) in the infrared band is still much more important than the emitted radiation (E) of the Earth (Figure 5.1), which peaks in this band, the 10 μm - 12 μm band will only measure the emitted radiation from the Earth because the Earth's reflectivity (R) in this band is very small. This is illustrated by the following equation:

$$PR \ll E$$

Different objects have different reflectance spectrums. Figure 5.4 shows the reflectance spectrum of several different materials. The reflectance of a body depends upon the wavelength. As an example, snow reflects about 80% in the visible band but less than 10% in the infrared band. In general, the reflectance of solar radiation by any object in the 10 μm - 12 μm band is much less than the emitted radiation by these same objects in this same wavelength band because the reflectivity in the far infrared band is very small. Figure 5.5 shows also the reflectance of different materials and concentrates on the visible wavelengths. Snow reflects about 80% and vegetation, water, and soils reflect all about 10% to 20% in the 0.4 μm - 0.7 μm band and therefore can not be easily differentiated from another in this wavelength band. On the contrary, in the 0.7 μm - 0.9 μm band, vegetation reflects about 60%, whereas soil's and water's reflection do not change much. In this range, vegetation will therefore stand out clearly.

The reflectance of the vegetation depends upon the species (Figure 5.6). The reflectance in the 0.4 μm - 0.7 μm range is similar for all species but varies greatly in the 0.7 μm - 0.9 μm range. It goes from 30% for coniferous forests up to 70% for deciduous

forests. However, it is still greater than the background and this permits to make a distinction between species when using remote sensing techniques.

The reflectance of the vegetation also depends upon the health of the plant (Figure 5.7). For deciduous vegetation, the normal reflectance in the range 0.7 μm - 0.9 μm is about 70%. If the deciduous vegetation suffers from an incipient damage, then the reflectance in the 0.7 μm - 0.9 μm range lowers down to 50%. If this same vegetation suffers from a chronic damage, then the peak of 20% reflectance at the 0.55 μm wavelength shifts to the right to 0.6 μm. If the leaf is dead, as happens when the vegetation experiences fire, then the average reflectance in the 0.7 μm - 0.9 μm range decreases down to 30%. In Figures 5.6 and 5.7, the maximum radiation intensity in the visible range peaks at about 0.55 μm, in the green. Green is therefore the color of healthy vegetation. Due to chronic damage, the color goes from green to yellow (0.6 μm) and when the leaf is dead, the color is then red (0.7 μm).

There are several remote sensing tools which use the principles previously mentioned. Multispectral scanners equipped with electro-optical sensors onboard planes or satellites can measure or store data in several different regions of the electromagnetic spectrum. Satellites currently in use can be classified as Earth resources satellites with a high spatial but low temporal resolutions (LANDSAT-4,5, SPOT, MOS-1, IRS-1) or as meteorological satellites with a coarse spatial but high temporal resolutions (METEOSAT, NOAA-9,10, NIMBUS-7,GOES-7). They can also be classified as sun synchronous polar orbiting satellites (LANDSAT-4,5, SPOT, MOS-1, IRS-1, NOAA-9,10, and Nimbus-7) or as geostationary satellites (METEOSAT, GOES-7). The full names of all these satellites are given in Table 5.1. The measure tools onboard these satellites have very different characteristics[1]. The most important differences like the number of bands, the spatial resolution, and the sampling frequency are summarized in Table 5.2.

Biomass burning can be remotely sensed by the AVHRR sensor onboard the NOAA-9,10 satellites, by the TM and MSS sensors onboard LANDSAT-4,5, by the HRV-P and HRV-XS sensors onboard SPOT, and by the OLS sensor onboard the DMSP satellite. For each one of these sensors, their application for remote sensing is very specific. The OLS tool senses active fires on a regional scale. This satellite provides low-light imagery and is especially useful at night[4]. The TM and MSS tools sense small fires due to their high spatial resolution, but on a local scale[5,9], because of the high price of the imagery[10]. The NOAA-AVHRR tool can sense active fires on a regional scale with its infrared channel and fire scars with its visible and near-infrared channels[6].

The remote sensing of fires from space can be carried out by four forms of measurements. Tools onboard satellites can remotely sense either the direct radiation from the fires, the smoke produced by the fires, the postfire char, or finally the altered vegetative structure of vegetation. Each method has its own advantages and faults.

Remote sensing of active fires is carried out by the use of a mid-infrared channel in the 3 μm - 4 μm range. Due to their high thermal radiation, active fires are enhanced in this wavelength band and therefore stand out clearly. Thermal radiation is so enhanced, that fires, even less than a pixel, can be detected and often saturate the sensor[6]. Dozier[7] devised a method to compute the size of active fires using these properties. According to his work, the measured emitted radiation of a surface area, represented in the imagery by a pixel, relates both to the radiation of the active fire and to the radiation of the background. The relation is:

$$E(T) = pE(T_f) + (1-p)E(T_b)$$

$E(T)$ is the measured radiation in the mid-infrared channel.

$E(T_f)$ is the estimated radiation of the fire at the apparent temperature $T_f$.

$E(T_b)$ is the estimated radiation of the background at the temperature $T_b$.

$p$ is the part of the radiation corresponding to the fire.

By estimating $E(T_f)$ and $E(T_b)$, $p$ can be deduced and, knowing the size of the area represented by a pixel ($S_p$), the area attributed to the actual fire can be estimated to $S_f$, with:

$$S_f = pS_p$$

The major problem with this size estimation is the saturation of the sensor by small but highly radiant fires. As an example[6], with a background temperature of 300°K, a fire temperature of 400°K saturates the AVHRR sensor with p=0.05, whereas a fire temperature of 700°K saturates this same sensor with p=0.0007. Very small fires can therefore saturate the sensors.

Remote sensing of smoke is based on the scattering and absorption of radiation by particles in the smoke plume. The main problem turns out to be that the signal is sometimes not strong enough to be separated from the background[8]. Moreover the sizes of the plumes are not necessarily related to the fire area.

Remote sensing of chars is quite reliable for estimating large fire sizes because they are sensed at scale, not like the active fires and the smoke plumes. According to Robinson[8], high resolution imagery is required for scars less than 10 to 30 $km^2$ but other studies show that good estimations can nevertheless be made with smaller fire sizes[11].

Remote sensing of the altered structure of the vegetation is largely used because fires do not always produce distinct chars but sometimes less distinct scars. The main problem in sensing scars is that scar behavior is sensitive to local plant ecology and an ecological understanding of the studied region is required[8]. Moreover chars and scars have variable lifetimes. After burning, vegetation regrows and has a higher reflectance than non-burned, and therefore older, vegetation[9].

One objective of this study is to remotely sense burn scars on a regional scale. Spain and Portugal are selected for this study because these two countries accounted for 50% of the total burning in western Europe in 1987. The area involved implies the use of a regional scale tool. Otherwise, the price of the data would be prohibitive if high resolution data was to be acquired[10]. If Landsat scenes were to be acquired for Spain and Portugal in 1988, about 20 scenes (185 km by 170 km) would be needed to cover the two countries (50 471 000 ha for Spain and 8 800 000 ha for Portugal). Since each single scene costs about $4 000, the total would amount to $80 000. In comparison, a LAC scene covering all of western Europe only costs $100. The price of the data is indeed proportional to its ground resolution. Therefore, the area conditions simply discard the use of the TM, MSS, and OLS imagery. The only affordable and appropriate imagery to Europe is the NOAA-AVHRR imagery because of its low price and its high temporal resolution, even though this sensor does not provide the highest available spatial resolution. In the next chapter, the properties of the NOAA-AVHRR detector will be discussed fully.

TABLE 5.1

NAME OF THE MOST IMPORTANT REMOTE SENSING SATELLITES AND THEIR SENSORS

| | |
|---|---|
| GOES-7 | Geostationary Operational Environmental Satellite |
| VISSR | Visible Infrared Spin Scan Radiometer |
| NOAA | National Oceanographic and Atmospheric Administration |
| AVHRR | Advanced Very High Resolution Radiometer |
| LAC | Local Area Coverage |
| GAC | Global Area Coverage |
| CZCS | Coastal Zone Color Scanner |
| TM | Thematic Mapper |
| MSS | Multi Spectral Sensor |
| SPOT | System Pour l'Observation de la Terre |
| HRV P | High Resolution Visible Panchromatic |
| HRV XS | High Resolution Visible multispectral |
| MOS | Marine Observation Satellite |
| MESSR | Multispectral Electronic Self Scanning Radiometer |
| VTIR | Visible and Thermal Infrared Radiometer |
| DMSP | Defense Meteorological Satellite Program |
| OLS | Operational Linescan System |
| IRS | Indian Remote Sensing |
| LISS-I | Linear Imaging Self Scanning Sensor-I |

From A Guide to Remote Sensing: Interpreting Images of the Earth[1]

TABLE 5.2

MAIN CHARACTERISTICS OF COMMON SENSORS

| Satellite | Sensor | # bands | Spatial resolution | Sampling frequency |
|---|---|---|---|---|
| GOES-7 | VISSR | 2 | 8 km | 30 mn |
| METEOSAT | | 2 | 900 m (visible)<br>7 km (IR) | 3 hours |
| NOAA-9,10 | AVHRR | 5 | 1 km (LAC)<br>4 km (GAC) | 12 hours |
| NIMBUS-7 | CZCS | 6 | 800 m | 6 days |
| LANDSAT-4,5 | TM<br><br>MSS | 7<br><br>5 | 30 m (visible)<br>120 m (IR)<br>80 m (visible)<br>240 m (IR) | 18 days<br><br>18 days |
| SPOT | HRV P<br>HRV XS | 1<br>3 | 10 m<br>20 m | 26 days<br>26 days |
| MOS-1 | MESSR<br>VTIR | 4<br>4 | 50 m<br>900 m (visible)<br>2,7 km (IR) | 17 days<br>17 days |
| DMSP | OLS | 2 | 0.6 km (LAC)<br>2.7 km (GAC) | daily |
| IRS-1 | LISS-I | 4 | 73 m | 22 days |

From A Guide to Remote Sensing: Interpreting Images of the Earth[1]

FIGURE 5.1

SPECTRAL EMISSION OF BLACKBODIES AT DIFFERENT TEMPERATURES

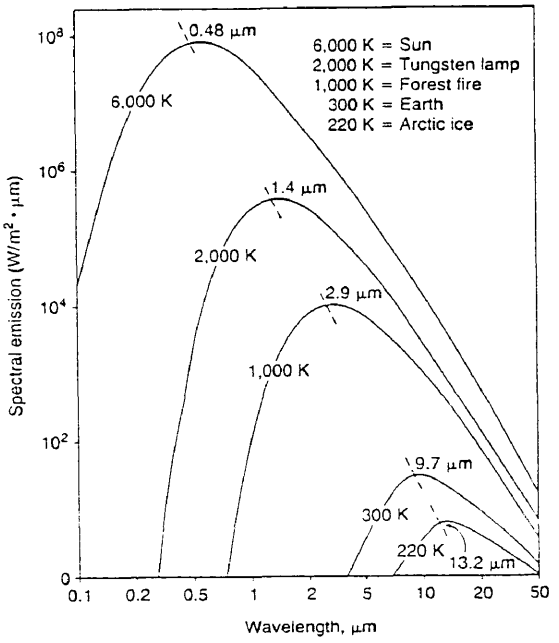


FIGURE 5.2

SOLAR IRRADIATION OUTSIDE THE ATMOSPHERE AND AT SEA LEVEL

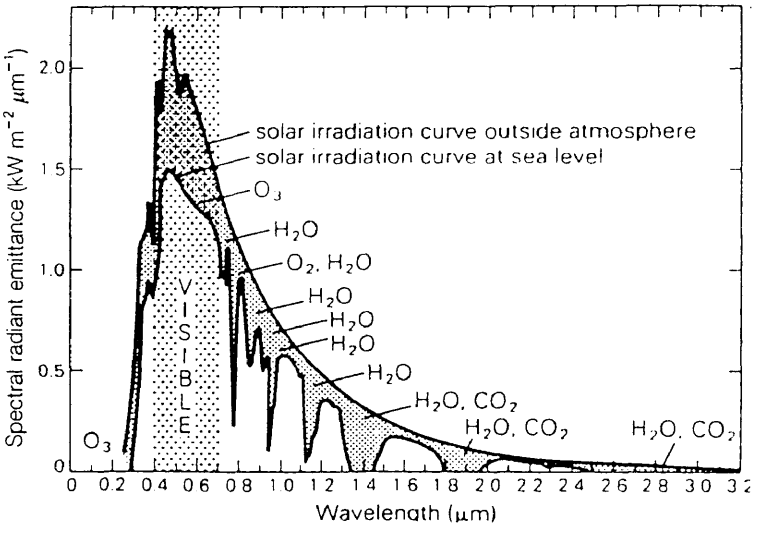

FIGURE 5.3

ATMOSPHERIC WINDOW

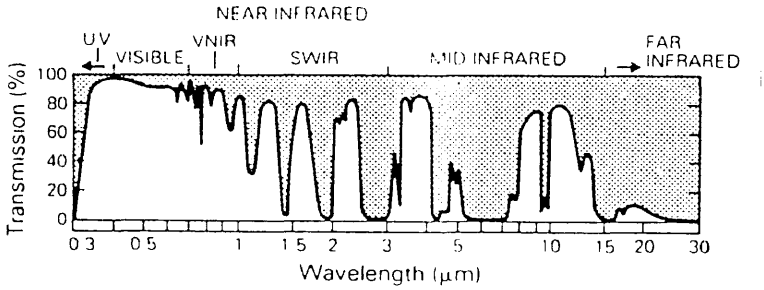


FIGURE 5.4

REFLECTANCE IN VISIBLE TO FAR INFRARED WAVELENGTHS

OF VEGETATION, WATER, AND SOIL

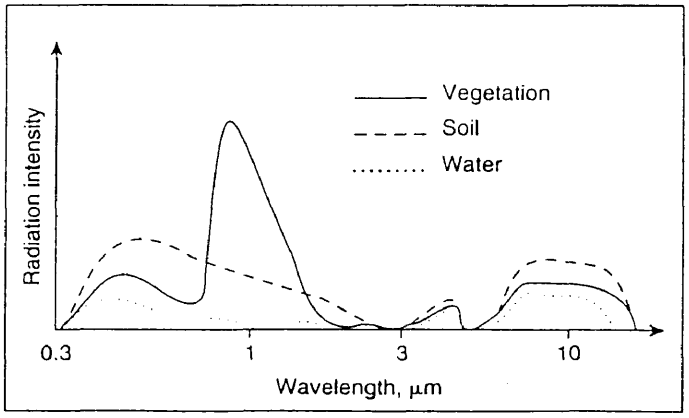

FIGURE 5.5

REFLECTANCE IN VISIBLE AND NEAR INFRARED WAVELENGTHS OF 6 MATERIALS

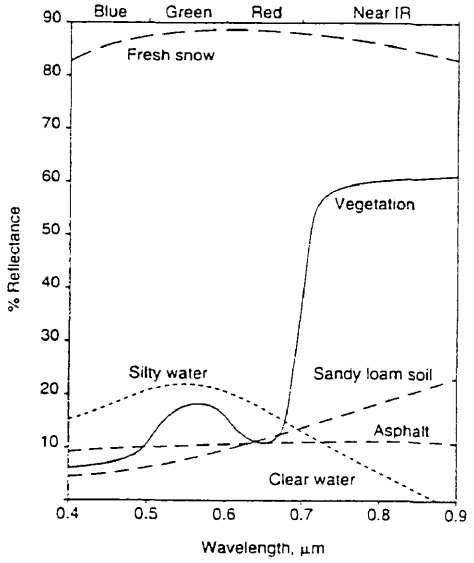


FIGURE 5.6

REFLECTANCE IN VISIBLE AND NEAR INFRARED WAVELENGTHS OF TREE SPECIES

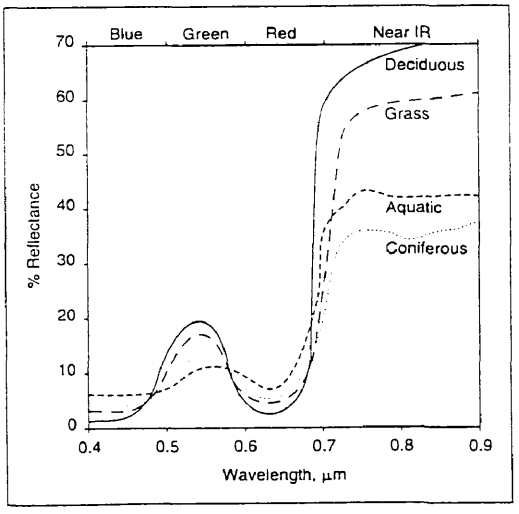

FIGURE 5.7

REFLECTANCE OF VEGETATION FOLLOWING BURNING

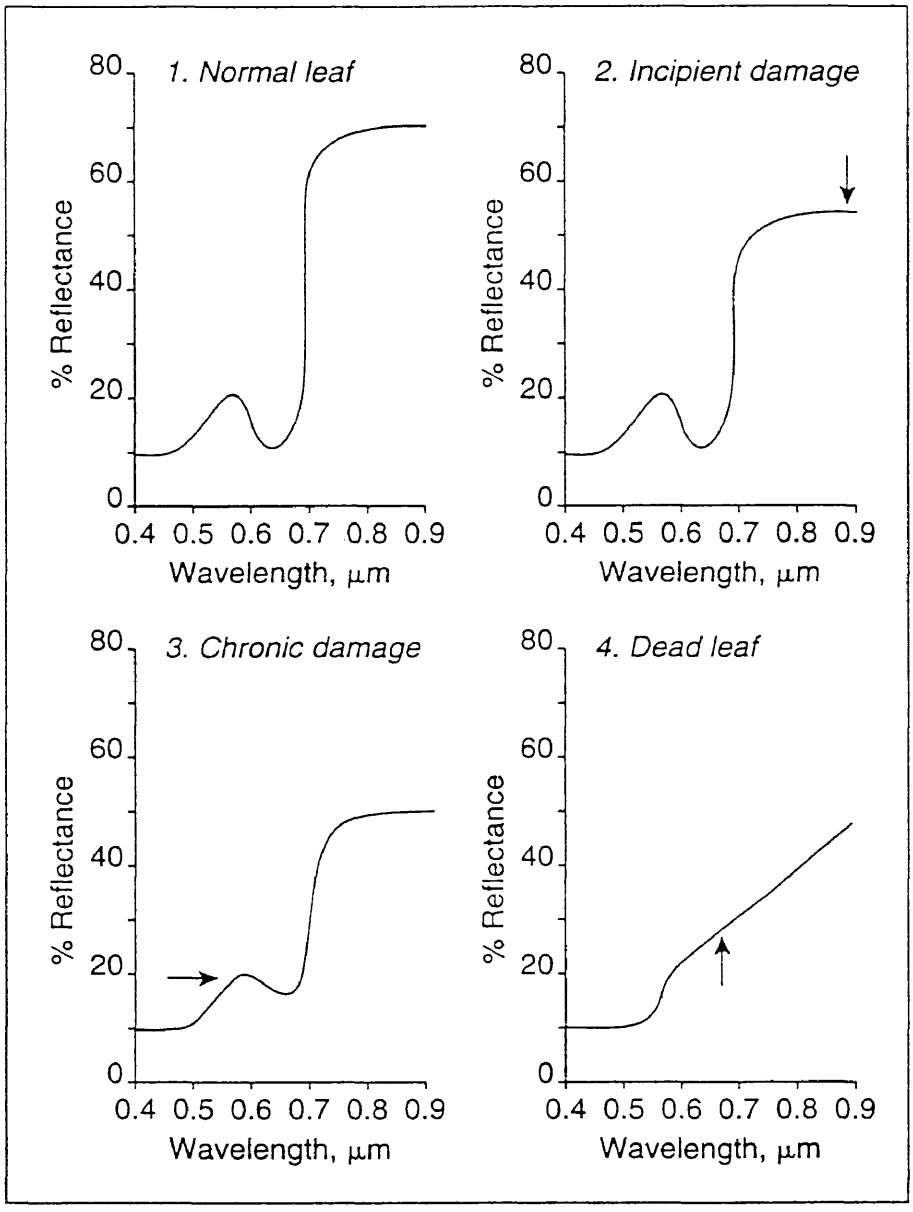

## NOTES TO CHAPTER V

1. Drury, S. A. A Guide to Remote Sensing: Interpreting Images of the Earth. Oxford Science Publications, 1990.

2. Avery, T. E., Berlin, G. L. Fundamentals of Remote Sensing and Airphoto Interpretation. 5th edition, Macmillan Publishing Company, 1992.

3. Wallace, J. M., Hobbs, P. V. Atmospheric Science: an introductory survey. Academic Press, 1997.

4. Cahoon, Jr., D. R., Stocks, B. J., Levine, J. S., Cofer III, W. R., O'Neill, K. P. Seasonal Distribution of African Savanna Fires. Nature, Vol 359, 812-815.

5. Brustet, J. M., Vickos, J. B., Fontan, J., Podaire, A., Lavenu, F. Global Biomass Burning: Atmospheric, Climatic, and Biospheric Implications. 53-60 Cambridge, Massachusetts: MIT Press, 1991.

6. Brustet, J. M., Vickos, J. B., Fontan, J., Manissadjan, K., Podaire, A., Lavenu, F. Global Biomass Burning: Atmospheric, Climatic, and Biospheric Implications. 47-52 Cambridge, Massachusetts: MIT Press, 1991.

7. Dozier, J. A Method for Satellite Identification of Surface Temperature Fields of Subpixel Resolution. Remote Sensing of Environment, 11, 221-229, 1981.

8. Robinson, J. Global Biomass Burning: Atmospheric, Climatic, and Biospheric Implications. 67-73 Cambridge, Massachusetts: MIT Press, 1991.

9. Lopez Garcia, M. J., Caselles V. Geocarto International: a Multi-disciplinary Journal of Remote Sensing. Vol. 6, 1, 1991.

10. EOSAT, Purchasing Guide.

# CHAPTER VI

# THE NOAA AVHRR DETECTOR

The use of the NOAA-AVHRR sensor was shown to be appropriate in the previous chapter to remotely sense burn scars in the mediterranean countries of Europe because of its high sampling frequency and because of the affordable price of the data it provides. Before ordering and processing the data, a thorough insight of the main characteristics of the NOAA-9 satellite and of the data measured by the sensor AVHRR is needed in order to have a better understanding of the imagery provided. All the mentioned information in this chapter concerning the satellites and the sensors can be found in the Users Guide of the NOAA Polar Orbiter Data[1].

The satellite NOAA-9 belongs to the TIROS-N series, composed of eight satellites. The first one was launched in 1978 and the following ones were launched at the rate of about one every other year. They have a lifetime of a few years and are expected to operate two at a time in order to enhance the sampling frequency.

In 1987 and 1988, the satellites NOAA-9 and NOAA-10 were operational. They are sun-synchronous near-polar orbiting satellites at an average altitude of 833 km. The altitude may vary because of the slightly elliptic trajectory. A near-polar orbiting satellite circles the Earth in a plane tilted from the polar axis by a few degrees. A sun-synchronous satellite flies over all places on the Earth having the same latitude at approximately the same local time. Consequently, the solar illumination during identical seasons in different years should be the same[2].

The NOAA-9 satellite has an ascending node (northbound equatorial crossing) at 2:20 pm and a descending node (southbound equatorial crossing) at 2:20 am, both in local solar time. On the other hand, the NOAA-10 satellite has an ascending node at 7:30 pm and a descending node at 7:30 am, both in local solar time. The NOAA-10 passes over Europe will therefore take place a few minutes later than the northbound equator crossing in the evening and a few minutes sooner than the southbound equator crossing in the morning. In both cases, the sun's elevation angle above the horizon will be too low to provide a proper contrast in the visible and near-infrared channels. Therefore, the data from the NOAA-10 satellite was not used in this study. The data used will be exclusively provided by the NOAA-9 satellite and, out of the two daily passes, only the afternoon pass (a few minutes after 2:20 pm, solar time) will be useful because the morning pass occurs at night (before 2:20 am). Since the orbital period of the NOAA-9 satellite is 102 minutes, it will take the satellite approximately 7 minutes to fly over Europe from $30^{o}$ north latitude to $55^{o}$ north latitude.

The AVHRR sensor onboard the NOAA-9 satellite is an across-track scanning device (Figure 6.1). It means that the scanned line is perpendicular to the forward motion of the satellite. The AVHRR tool senses 2048 samples per scan line and its scanning rate is of 360 scans per minute (0.0167 seconds per scan line). Since the centers of the samples in a scan line are 0.95 milliradians apart, then the angular field of view (AFOV) of the sensor is $111.5^{o}$. Using this angular field of view, one can calculate the nominal ground swath which turns out to be about 2800 km (Figure 6.2).

The AVHRR tool simultaneously senses radiation in five different wavelength bands called channels. These correspond to atmospheric windows (Chapter V). The wavelengths corresponding to the five channels are listed in Table 6.1. Channel 1 senses visible radiation, channel 2 senses near-infrared radiation, channel 3 senses middle-infrared radi-

ation, and both channels 4 and 5 sense far infrared-radiation (thermal radiation). Each channel of the AVHRR tool has a slightly different instantaneous field of view (IFOV). They are also listed in Table 6.1. The IFOV determines the ground cell resolution of the sensor. It defines the angle of measure from the satellite of a sample on the ground (Figure 6.1). Since the satellite flies at an altitude of about 833 km and since the average IFOV can be approximated to 1.40 milliradians, then the central ground cell resolution can be approximated to a square of 1.17 km by 1.17 km at nadir. At the far ends of the ground swath, the ground cell resolution will be much higher due to the curvature of the Earth. The corresponding edge ground cell area is about 18 $km^2$ (Cahoon[3]), instead of 1.4 $km^2$ at nadir.

The data, provided by the sensor in the five different channels, is transmitted to acquisition stations in three formats which are:

-the HRPT format (High Resolution Picture Transmission)
-the LAC format (Local Area Coverage)
-the GAC format (Global Area Coverage)

The HRPT format is a direct readout format and is therefore continually broadcast to Earth. Only the acquisition stations in the satellite's emission range will be able to record the HRPT data. The two Command and Data Acquisition stations in the United States (Wallops Island, VA and Fairbanks, Alaska) cannot record HRPT data of Europe.

The LAC data is HRPT data recorded onboard the satellite and then later broadcast when in the transmission range of one selected station. The TIROS-N satellites carry five digital tape recorders which can record only 10 minutes of full resolution data. All of Europe can therefore be recorded since it only takes 7 mn to fly over Europe. But the LAC

data has to be selectively ordered in advance because the recording time is short compared to the total time of revolution. That is the reason why there are few available LAC scenes of Europe in the United States.

The last available format is the GAC format. The GAC data is a degraded sampling of the full resolution. Only one out of three original lines is conserved and the data is further reduced by averaging every four adjacent samples and skipping the fifth one along each selected scan line. Therefore, only four out of fifteen samples are recorded. Thus the volume is 4/15 times less important and the resolution is 15/4 times larger than for the LAC data. The number of samples in a scan line is reduced by a factor of five and comes out to 409. The ground cell resolution is equal to 4.4 km at nadir. Thus, the ground cell area at nadir is 19 $km^2$. As for the LAC data, the edge ground cell area of the GAC data at both the far right and left ends of the ground swath will be much higher. It has been estimated by Cahoon[3] to be equal to about 220 $km^2$. Also, the GAC data is first recorded and then later transmitted but, unlike the LAC data, the volume of storage being less important, the digital tapes onboard the satellite can record 110 minutes of data (more than a full orbit). Therefore this data does not have to be requested in advance.

The whole GAC data for the year 1987 is available at the NASA Langley Research Center. This GAC data was used by Cahoon[4] to study the Great Chinese Fire of 1987. Since the area burned was estimated to be as high as 4.7 million hectares, the GAC data turned out to be precise enough for this study. However, this is not true for small fires. According to Cahoon[3], areal burn scars can be estimated with a low percentage error when using GAC imagery with a target size over 800 $km^2$. That was the case in China and the former Soviet Union but this is certainly not the case in Europe. Indeed, in Italy, Portugal, Spain, and Greece, the average fire's areas are respectively 6.3 ha, 10.9 ha, 16.8 ha, and 36.6 ha (Table 4.9). Even when using the LAC imagery (1.1 km resolution at nadir),

the majority of the scars in these European countries won't appear. The resolution of 140 ha at nadir is indeed much larger than the fire averages in the mentioned countries. Nevertheless, the assumption can be made that the fires larger than 140 ha account for the majority of the burning. Moreover, still according to Cahoon[3], target sizes less than 100 $km^2$ can be easily located in the LAC imagery. That is the reason why LAC data has been preferred to GAC data in this study.

The AVHRR data is available at the NOAA/NESDIS (National Environmental Satellite Data and Information Service) office in Washington D.C.. The LAC data is provided on 6250 BPI magnetic tapes (storage capacity: 180 Mbytes) and is referred to as level 1b data base. Since images are called data base only after preprocessing, the data provided at the archives has been corrected for geometric distortions, noise patterns, variations in solar illumination angles, and atmospheric haze[2]. The record structure of each file is thoroughly detailed in the Users Guide of the NOAA Polar Orbiter Data[1].

In order to study the distribution of biomass burning for the year 1987 in Spain and Portugal, which account for the majority of the burning in Europe, LAC data in early 1987 and early 1988 was needed. It was decided to acquire LAC data for both years during the months of April and May in order to span the fire season which usually begins in summer and ends in autumn. The months of April and May correspond to spring in Europe, and it is in this period of the year when vegetation regrows. Therefore, vegetation will reflect much more than scars and chars allowing the latter to stand out clearly. Moreover, when choosing scenes of a particular area at the same period of two different years, the position of the Sun and its luminance are expected to be identical. This will facilitate the comparison.

The NOAA/NESDIS office provided the listings of the available LAC scenes over Europe for April and May 1987 and April and May 1988. Only 86 scenes were available in April 87, but 127 in may 1987, 109 in April 1988, and 125 in May 1988. The goal of this computer search was to select clear scenes of the few countries we are interested in. Unfortunately, all these scenes are not equally distributed in terms of days and of geographical areas because they were ordered in advance for specific purposes which are now unknown to us. Moreover, April and May of 1987 turned out to be pretty cloudy over most of Europe. The cloud cover during these months shows up very clearly on METEOSAT images. The METEOSAT images of Europe for these four months have been studied. In order to get useful LAC scenes of the selected regions, the available scenes must be cloudless. This requirement drastically lowers the number of useful scenes. Clear scenes of some countries could not even be found during the months of April and May and therefore had to be looked for in the preceding and following months of March and June.

The scenes, selected according to these criteria, are designated by the year followed by the Julian date of the day they were taken. The scenes 87128 (8 May 1987) and 88085 (25 March 1988) display clearly Spain and Portugal (Images 6.1 and 6.2), whereas the scenes 87107 (17 April 1987) and 88101 (10 April 1988) display clearly the mediterranean part of France (Images 6.3 and 6.4). In the next chapters these scenes will be processed and interpreted.

IMAGE 6.1

METEOSAT IMAGE OF WESTERN EUROPE ON MAY 8, 1987

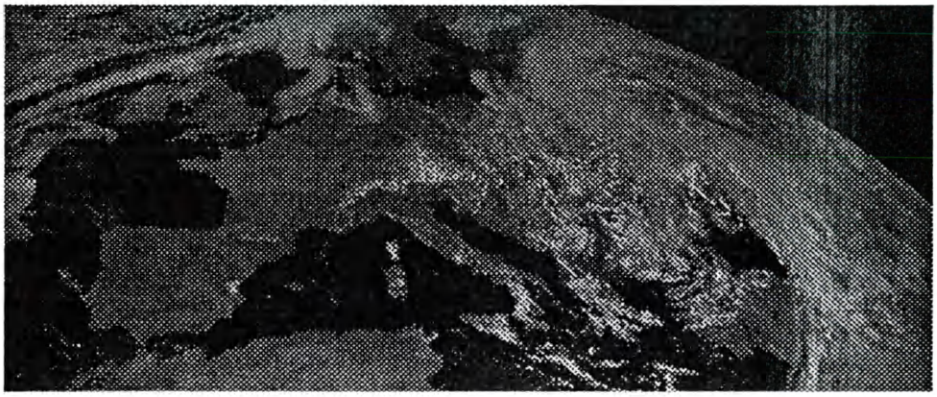

IMAGE 6.2

METEOSAT IMAGE OF WESTERN EUROPE ON MARCH 25, 1988

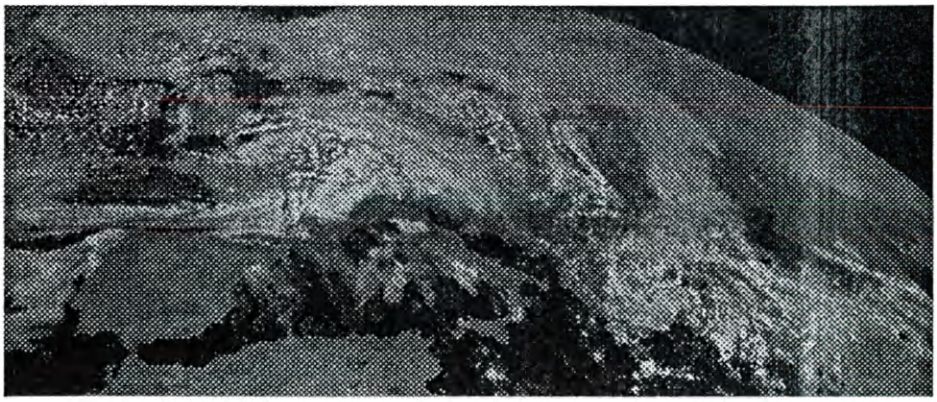

IMAGE 6.3

METEOSAT IMAGE OF WESTERN EUROPE ON APRIL 17, 1987

IMAGE 6.4

METEOSAT IMAGE OF WESTERN EUROPE ON APRIL 10, 1988

TABLE 6.1

WAVELENGTH BANDS AND IFOV OF THE AVHRR SENSOR

| Channel # | Wavelength band (μm) | IFOV (millirads) |
|---|---|---|
| 1 | 0.58 - 0.68 | 1.39 |
| 2 | 0.72 - 1.10 | 1.41 |
| 3 | 3.55 - 3.93 | 1.51 |
| 4 | 10.3 - 11.3 | 1.41 |
| 5 | 11.5- 12.5 | 1.30 |

From the NOAA Polar Orbiter Data Users Guide[1]

FIGURE 6.1

IFOV AND AFOV OF THE NOAA-9 AVHRR SENSOR

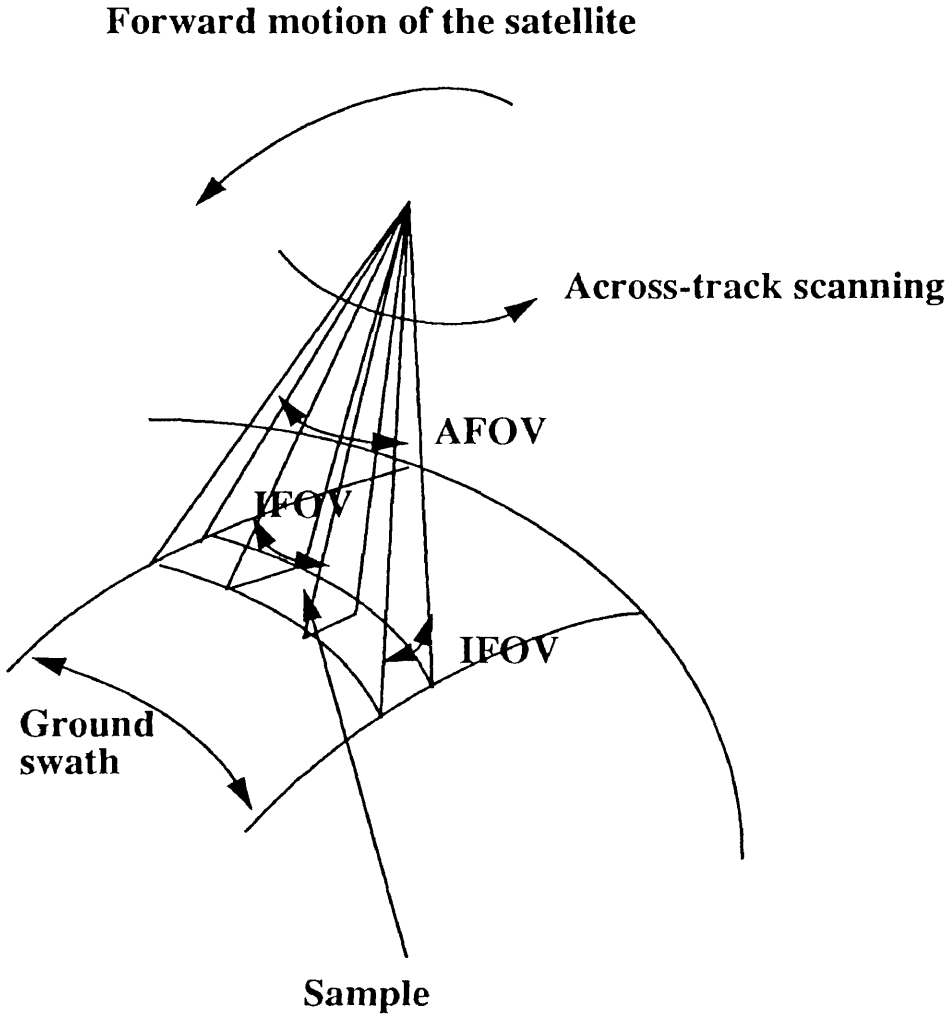

FIGURE 6.2

GROUNDSWATH OF THE NOAA-9 AVHRR SENSOR

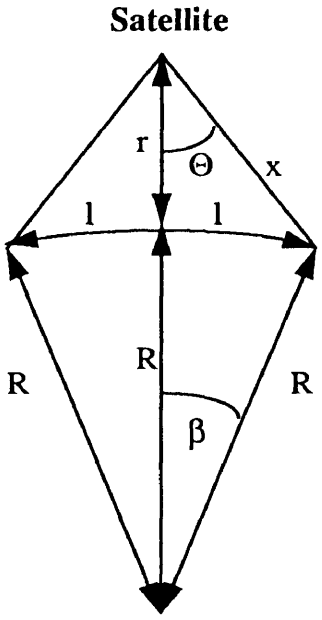


**Θ= 55.75 °**
**r = 833 km**
**R = 6400 km**

**x = 1697 km**
**b = 12.66 °**
**l = 1414 km**

## NOTES TO CHAPTER VI

1. Kidwell, K. B. NOAA Polar Orbiter Data Users Guide. National Oceanic and Atmospheric Administration, Satellite Data Services Division, U. S. Department of Commerce, 1991.

2. Avery, T. E., Berlin, G. L. Fundamentals of Remote Sensing and Airphoto Interpretation. 5th edition, Macmillan Publishing Company, 1992.

3. Cahoon, Jr., D. R., Stocks, B. J., Levine, J. S., Cofer III, W. R., Chung, C. C. Journal of Geophysical Research. vol. 97, no. D4, 3805-3814, 1992.

4. Cahoon, Jr., D. R., Levine, J. S., Cofer II, W. R., Miller, J. E., Minnis, P., Tennille, G. M., Yip, T. M., Stocks, B. J., Heck, P. W. Global Biomass Burning: Atmospheric, Climatic, and Biospheric Implications. 61-66 Cambridge, Massachusetts: MIT Press, 1991.

# CHAPTER VII

# SATELLITE IMAGE PROCESSING

The satellite imagery has to be processed in order to yield specific information relative to scars and chars following forests fires. The first thing to do is to unpack and calibrate the data so that the imagery can be visualized. Then, the images will be processed in order to accurately compare different scenes of the same area and in order to enhance scars and chars. Finally, the spectral signatures of well located scars will be studied. In this chapter, this rationale is applied in detail to southern France as an example, although this country does not belong to the top four emitters of $CO_2$ released by biomass burning in western Europe (Chapter IV). The reason for studying France first is that the location of selected large fires in this country is well known, whereas, for other mediterranean countries it is not known at all. The two scenes that will presently be used are the AVHRR scenes 87107 and 88101 (Chapter VI).

The data on the nine track tapes obtained from NOAA/NESDIS are packed and non calibrated. This means that, for each sample scanned, the data from different channels follow each other. The unpacking consists in the rearrangement of the data so that the data for each channel will be put together in a distinct block for all the samples scanned in the scene. Thus, the data for channel 1 will be followed by the data for channel 2 and so forth.

The unpacked data will be calibrated at the same time with information provided in the NOAA Polar Orbiter Data Users Guide[1]. The data in channels 1 and 2, the visible

and near infrared channels, will be converted to reflectances using the relation:

$$A_i = S_i C + I_i$$

$A_i$ represents the reflectance measured in channel i, with i equal to 1 or 2, and $C$ is the value of the radiation measured in this channel for a particular sample. Since $C$ is a 10 bit number, its value ranges from 0 to 1023 counts. $S_i$ and $I_i$ are the slope and the intercept of the calibration curve. They are provided in the NOAA Polar Orbiter Data Users Guide[1]. Once calculated, it turns out that $A_i$ ranges between 0 and 25 for the majority of the surface samples. Therefore, in order to have the maximum contrast offered by an 8 bit imagery, the $A_i$ values are multiplied by 10. The majority of the surface samples therefore have a pixel intensity between 0 and 250. Clouds and snow, which have an original measured reflectance greater than 25, do not fit in the 0 to 255 output range when multiplied by 10. They are assigned the value 255.

The data in channels 3, 4, and 5, the middle and far infrared channels, will be converted to surface temperature values. The thermal channel calibration is:

$$E_i = S_i C + I_i$$

$E_i$ represents the energy value of the sample. $S_i$, and $I_i$ have the same significance as that for the channel 1 and 2 calibration but have different values. The conversion to brightness temperature from energy is performed using the inverse of Planck's radiation equation (Chapter V). Therefore the temperature is equal to:

$$T(E_i) = \frac{C_2}{\lambda_i ln\left(1 + \frac{C_1}{E_i \lambda_i^5}\right)}$$

$\lambda_i$ is the central wavelength of the channel i and $C_1$ and $C_2$ are the first and second Planck's constants.

The dimensions of the AVHRR files are given by the relation:

*dimension = number of samples × number of lines × number of channels*

Since the file 87107 has 2065 lines, its dimension are 2048×2065×5 or 21 145 600 bytes. Similarly, since the file 88101 has 1684 lines, its dimension are 2048×1684×5 or 17 244 160 bytes. The 87107 scene therefore spans a south-north distance greater than that spanned by the 88101 scene. For the 87107 scene, the NOAA-9 satellite flew northward over Europe from 13:42:10 to 13:47:54 (5 mn 44 sec) and for the 88101 scene, it flew over Europe from 14:25:38 to 14:30:20 (4 mn 42 sec). The difference of 58 seconds accounts for the difference of 381 lines (6 scan lines per second, Chapter VI).

Once the data has been unpacked and calibrated, it can be visualized. There are two main ways to visualize the imagery. Each channel can be separately displayed (8 bit imagery) or a combination of channels 1, 2 and 4 can be displayed (24 bit imagery). Software and hardware are different for these two visualizations.

The 8 bit imagery will be visualized using the XV software developed by John Bradley at the University of Pennsylvania. Each sample in the scene will be assigned a pixel on the screen. Pictures of the scenes in the different channels will now be discussed.

The channel 1 images of the 87107 and 88101 scenes display the reflected radiation in the visible band. They look darker and show less contrast than the corresponding channel 2 images. Therefore, emphasis in the discussion will be put on the channel 2 images.

The channel 2 image (Image 7.1) for the 87107 scene and the channel 2 image (Image 7.2) for the 88101 scene display the measured reflectance in the near-infrared channel (0.72 μm - 1.10 μm) of the NOAA-9 AVHRR sensor. Since water reflects about 5% of the incoming radiation (Chapter V), it appears dark on the image. Vegetation reflects from 30% for coniferous species to 70% for deciduous species (Chapter V). Coniferous vegetation will therefore appear darker than deciduous vegetation, but lighter than water. A good example is the forest of Landes in southwestern France, which is surrounded by deciduous vegetation (Figure 3.8). The contrast appears clearly on Image 7.1. Snow reflects about 85% (Chapter V) and therefore appears white like clouds which reflect about 100% of the incoming radiation. The data provided by channel 3 won't be used because measurements in this channel are subject to an instrument problem[1].

The channel 4 image (Image 7.3) for the 87107 scene and the channel 4 image (Image 7.4) for the 88101 scene display the surface temperature using the data in the far-infrared channel (10.5 μm - 11.5 μm) of the NOAA-9 AVHRR sensor. On these two images the contrast has been enhanced. During daytime, water is colder than land. Therefore water emits less radiation and appears slightly darker than land. Snow's temperature ($0^{o}C$) is much less than water's temperature, and as a result snow appears darker than water. The Alps show up clearly on both images. Clouds are much colder than snow because they are high in the troposphere. They therefore appear completely black. The data provided by channel 5 was not used because this channel is very similar to channel 4. The images are therefore redundant.

The major large scale difference between the 87107 and 88101 scenes is the cloud cover. On the $10^{th}$ of April 1988, there were more clouds over western Europe than on the $17^{th\ of}$ April 1987. This is confirmed by the Meteosat images for these two days (Images 6.3 and 6.4).

In order to display the 24 bit imagery, a different software routine is used. The System 600 Image Processing Software, Version 4.0, by International Imaging Systems is available at the NASA Langley Research Center. It operates on a Sun Sparc 330 and it is an integrated multi-spectral spatial data analysis system. It supports a specific hardware called Interactive Viewing and Analysis Station or IVAS. It is a user programmable image and graphics display processor. The display resolution is 1024 by 1024 and a combination of at most three channels can be displayed through the three guns of the screen (red, green, and blue). Among the five channels available with the LAC imagery, channel 1, 2 and 4 are chosen. Channel 3 is discarded because it is noisy and channel 5 is not selected because it is very similar to channel 4. Therefore, channels 1, 2, and 4 are displayed respectively through the red, green and blue guns of the screen. Color reconstruction can be implemented with the color additive process. The resulting image is called a false color image. The number of different colors available in the 24 bit imagery is $2^{24}$ or 16 777 216. When displayed as described and with a unit weight for the output intensity in each channel, the 87107 scene is shown on Image 7.5. The blue shade is due to the unit weight attributed to each channel and to the high pixel intensity in channel 4 compared to that in other channels. In order to enhance the contrast of the false color imagery, the output pixel intensity has to be independently modified in each channel. The pixel intensity of a representative 10 000 pixel sample is displayed in Figure 7.1. In channel 1, the original pixel intensity of this sample ranges from 50 to 110. Therefore, the output pixel intensity in this corresponding range must be enhanced so that more red may be displayed. This modification is illustrated on chart a (Figure 7.2). In channel 2, the original pixel intensity of this same sample ranges from 90 to 180. Therefore, the output pixel intensity in this corresponding range must be slightly enhanced so that more green may be displayed. This modification is illustrated on chart b (Figure 7.2). Finally, in channel 4, the original pixel intensity of the sample ranges from 180 to 210. Therefore, the output pixel intensity in this corresponding range must be lowered so that less blue may be displayed. This modifica-

tion is illustrated on chart c (Figure 7.2). The resulting image with this new color table is displayed in Image 7.6. The 88101 scene is also displayed with the same color table in Image 7.7.

Once the new color map has been applied, a visual and qualitative "false-color" interpretation can be made. Water appears blue-red, snow appears white, clouds appear white-yellow, coniferous vegetation appears blue, and deciduous vegetation appears green.

The next step is to compare corresponding areas in the two scenes. In order to implement this comparison, the ground resolution of the selected areas must be identical. That is far from being the case in Image 7.6 and Image 7.7 because the satellite path was not the same for the two scenes. The ground resolution depends upon the distance of the sample from the nadir (Chapter VI). To resolve this difference, the two scenes have been mapped with the same ground resolution. The mapping procedure takes an image and its location data in latitudes and longitudes and then linearizes the original data to produce a flat equidistant projection. The resulting projection is called cylindrical equal area projection[2]. Therefore, a new coordinate system has to be used. A 100 pixel resolution per degree of latitude and longitude is chosen. More pixels result in a higher resolution. However, the original LAC resolution was less than that. It is therefore useless to artificially overenhance the resolution because no new data are provided. Moreover, with a larger resolution, the sizes of the files would be so huge that they would hinder the data processing. For each pixel in the new coordinate system, the mapping procedure finds the nearest pixel in the old one and assigns the looked up value to the new pixel.

The 87107 scene will then be mapped with a latitude resolution of 100 pixels, starting at $40^{o}$N and ending at $55^{o}$N, and with a longitude resolution of 100 pixels per degree, starting at $5^{o}$W and ending at $20^{o}$E. The dimension of the mapped image is of 2500 pixels longitudinally and of 1500 pixels latitudinally whereas the dimension of the non mapped image was of 2048× 2065 for a slightly larger area. The resolution has been artificially enhanced by extrapolation. The 88101 scene will be mapped according to the same longitudinal and latitudinal resolutions. Nevertheless, the boundary latitudes and longitudes do not have to be the same as those for the 87107 scene. The best fitting parallelepiped inscribed in the original image can be chosen for both scenes if the total scene is to be mapped, but a much smaller area can be mapped if desired. For the 88101 scene, the largest best fitting inscribed parallelepiped happens to have the same boundaries as for the 87107 scene. The two resulting mapped images are displayed in Image 7.8 for the 87107 scene and Image 7.9 for the 88101 scene.

When comparing the nonmapped and mapped images for the 87107 scene (respectively Image 7.6 and Image 7.8), one notices that the skewness in the nonmapped image disappears in the mapped image and that some missing scan lines show up in the mapped image. Their curvature is characteristic of a scan line. The black lower left angle in the mapped image corresponds to one of the parallelepiped's edges being outside of the original data scanned.

The dimensions of the two resulting files for the mapped scene are both equal to 2500×1500×4 or 15 000 000 bites. Channel 5 is discarded due to its similarity to channel 4. As a result, corresponding areas in the 87107 and 88101 scene are represented by the same number of pixels. Therefore the ground resolution no longer depends on the satellite path and on the date the image was taken.

What precedes is best illustrated when a $1^{o}\times1^{o}$ grid is superimposed on the mapped images. Image 7.10 displays part of France with such a grid for the 87107 scene on the left and for the 88101 scene on the right. With the screen split this way, the visual comparison of the same areas, one year apart, is much easier. When looking at this last image, it can be noticed that there are more clouds in the 88101 scene covering central France. Nevertheless, the main patterns such as cities, forests, and snow, are similar.

In France, most of the fires occur in the mediterranean forests. In 1987, about 10 393 ha burned in the mediterranean region of France out of a total of 14 108 ha[3]. That is a ratio of 74%. In 1986, about 45347 ha burned in the mediterranean forest out of 51 859 ha[3]. That was about 87% of the total area burned in France. It is estimated that, on average, 80% of the total burning occurs in the mediterranean region[3]. Therefore, this region should be thoroughly studied. The 25 year average area burned in France is 41 297 ha[3]. 1986 was an above average year in terms of burned areas and 1987, the year of interest in this study, was a below average year.

In order to study the small differences in the imagery of a particular area, the size of the display is enhanced until only a $1^{o}\times1^{o}$ area, belonging to a 1988 scene, fits in the right half the screen, the left half of the screen being for the same area in a 1987 scene. The resulting image is displayed in Image 7.11. Side by side are two close-ups of the same area which goes from $43^{o}$N to $44^{o}$N and from $6^{o}$E to $7^{o}$E. The two central squares have a 100×100 pixel resolution following the mapping procedure. When comparing the two images of the same area, one can notice that the same pattern shows up for the snow in the Alps (top half squares). The snow cover is similar because it is the same month (April) for both years. The bottom half squares represent the Mediterranean sea with sparse clouds for the 88101 scene. In the central squares, the vegetation pattern is quite similar but there are local differences which will be studied later in this chapter. Dense vegetation (forests)

corresponds to blue areas whereas sparse vegetation (shrubland, coppice) corresponds to green areas.

The two major differences are two reddish spots, one in the 87107 scene and another one in the 88101 scene. The reddish spot in the 87107 scene is a few tens of miles inland and at equal distance from the two cities of S$^t$ Raphaël and Cannes. It disappeared in the course of 1987 (it is no longer visible in the 88101 scene). The reddish spot in the 88101 scene is right on the coast at equal distance from S$^t$ Raphaël and Cannes. It appeared in the course of 1987 because it is not visible in the 87107 scene. These two reddish spots are interpreted as scars because they appear and disappear right in the middle of dense vegetation. The spot in the 88101 scene has been confirmed as a scar by a computer search through the Reuter database. This search provided a listing of the major fires that occurred in the course of 1987. One of them occurred on the 25$^{th}$ of August between S$^t$ Raphaël and Cannes and its surface was 2000 ha. That is why a scar appears on the 88101 scene whereas nothing shows up on the 87107 scene. The spot in the 87107 scene has been confirmed as a scar by a map of a fire[3] which occurred in the Tanneron forest on the 23$^{th}$ and 24$^{th}$ of August in 1986 (Figure 7.8). The extent of this fire was 7000 ha and had 8 different starting points. The severity of this fire was attributed to a very low air humidity and to a very strong "mistral" of 70 km/h (Chapter III).

A confirmation of the presence of scars in this region will be given by the Normalized Difference Vegetation Index or NDVI. It combines the data provided by channels 1 and 2 in such a way that variations in the state of the vegetation show up distinctively. The equation[4] for the NDVI is:

$$NDVI\,(pixel_{xy}) = \frac{A_2\,(pixel_{xy}) - A_1\,(pixel_{xy})}{A_2\,(pixel_{xy}) + A_1\,(pixel_{xy})}$$

where $A_1$ and $A_2$ are the reflectances corresponding to channels 1 and 2, which are defined previously in this chapter. The difference in the numerator emphasizes the properties of vegetation in channel 2 (Chapter V) and the summed denominator compensates for the changing illumination conditions[4]. The NDVI values for vegetation range from 0.1 to 0.2[4]. High values are associated with dense, healthy vegetation (Chapter V). Clouds, snow, and water have a negative NDVI value because they reflect more in channel 1 than in channel 2 (Chapter V). Rocks and soils reflect about the same amount and therefore have an NDVI value close to zero[4].

For each single pixel, among the 2500×1500 or 3 750 000 pixels which constitute the 87107 and 88101 mapped scenes, a substraction, an addition, and a division have to be carried out in order to get its NDVI value. The software CANTATA (University of New Mexico) has been used to apply this transformation. CANTATA is a visual programming environment for the Khoros system. The sequence of operations is illustrated on Figure 7.3. The values of the channel 1 and 2 data are first added and subtracted separately and then divided. The range for this intermediary result is [-1, 1]. The latter is then offset by adding 1 and becomes [0, 2]. This resulting range is finally scaled by multiplying by 150 so that the 8 bit display range be used at best. When applying the same offsetting and scaling to the NDVI range for specific surfaces, the estimated ranges are: [165, 240] for vegetation with the higher values corresponding to dense and healthy vegetation, and [<150] for clouds, snow, and water.

The NDVI image is a 3 750 000 pixel image. Since it is a one band image, the false color processing can not be applied. Nevertheless, in order to visualize the pixel intensity, a monochrome image is useless. That is the reason why a pseudo color image on IVAS is used. It allows the user to assign a spectrum of colors to a monochrome image. Three variables have to be set: hue, loops, and steps. Hue specifies the color assigned to pixel value

1. The range for hue is [0, 359] and 0 corresponds to red, 120 to green, and 240 to blue. The number of loops specifies the number of times the transform will loop through the entire color range. The number of steps defines the number of different colors assigned. If it is equal to 255, then a unique color will be assigned to each pixel value because the NDVI image is an 8 bit image.

The values selected in this study are 40 for hue, 3 for loops, and 255 for steps. The colors assigned to the full range are displayed in Figure 7.4. The NDVI images of France for the 87107 and 88101 scenes are displayed on the left and right halves of Image 7.12. This image is the counterpart of the false color image displayed in Image 7.10.

Image 7.13 displays the same two close ups as Image 7.11. On this image, the vegetation pattern shows up clearly for both years and, more importantly, it looks similar. Healthy vegetation appears blue and its actual pixel intensity ranges from 200 to 210. Nondense vegetation appears green and its actual pixel intensity ranges from 190 to 200. Snow appears magenta and its actual pixel intensity is 150. Water appears blue-magenta and its actual pixel intensity ranges from 130 to 140. All the intensity ranges fit in the estimated ranges following the NDVI transformation previously discussed and in the color assignment illustrated on Figure 7.4. Once the NDVI procedure is fully understood, the differences between the 87107 and 88101 scenes in Image 7.13 can be discussed. On these two NDVI images, the two scars, previously located with the false color imagery, show up in red. The red area between $S^t$ Raphaël and Cannes along the coast in the 88101 scene has a pixel intensity of 170 which corresponds to an original NDVI value of about 0.1. This figure indicates that the vegetation has been severely damaged. The red area inland, at equal distance from $S^t$ Raphaël and Cannes, in the 87107 scene, has a pixel intensity value of 160 which corresponds to a NDVI value of less than 0.1. Therefore, the area is probably also deprived of vegetation.

After the qualitative visualization of scars and healthy vegetation, a quantitative study of their spectral properties is required, in order to classify, later on, regions of interest in terms of their spectral characteristics. Each material has specific spectral properties depending upon the wavelength (Chapter V) and therefore their histograms in different wavelength bands are different. A histogram of a particular material in a channel represents the number of counts as a function of their intensity. Only the histograms for channels 1, 2, and 4 will be used because these channels are involved in the false color processing.

As an example, Figure 7.5 shows the three histograms, corresponding to channels 1, 2, and 4, for an area made up of water surrounded by land. In the 87107scene, Lake Geneva, on the border between France and Switzerland, has been cropped with some land surrounding it. When the number of counts are added up for each channel, the sum comes out to the total number of pixels cropped or 68×22 or 1496. The histograms in the three channels turn out to show a bimodal distribution due to the presence of two very spectrally different bodies which are land and water. The first peak in channels 1, 2 and 4 is characteristic of water because water reflects less than land and because water is colder than land during day. The second peak in the three channels is therefore characteristic of land.

This characterization will be applied to the scar visually located on the 88101 scene. The spectral signature of the scar in the 88101 scene is then to be compared with the spectral signature of the same area before the fire occurred, in the 87107 scene. The same square of 10×10 pixels has therefore to be cropped in both scenes. To the three histograms corresponding to channels 1, 2, and 4 has been added the histogram of the same area in the NDVI image. Figure 7.6 displays the four histograms for the scene 87107 whereas Figure 7.7 displays the histograms of the corresponding areas for the scene 88101. In channel 1, the reflection of the cropped area ranges between 60 and 90 for the

87107 scene whereas it ranges between 40 and 70 for the 88101 scene. In channel 2, the reflection of the cropped square ranges between 90 and 120 for the 87107 scene whereas it ranges between 80 and 110 for the 88101 scene. In channel 2, the scar reflects in average less than healthy vegetation. In channel 4, the average temperature for the cropped square is about 292°K for the 87107 scene whereas it is about 295°K for the 88101 scene. Differences in wind can be responsible for this discrepancy but also the lack of the cooling effect due to evapotranspiration can enhance the temperature of charred forests. This explains the higher temperature in the 88101 scene. In the NDVI histograms, there is a bimodal distribution for both years. In the 88101 scene, there are many more pixels in the left peak of the bimodal distribution than in the corresponding left peak in the 87107 scene. This means that the vegetation in the 88101 scene is not as healthy as in the 87107 scene. Pixels that were in the right peak for the 87107 scene have been included in the left peak for the 88101 scene because the vegetation they stood for was damaged by burning.

The information in the four histograms previously mentioned for both years confirms that a fire occurred along the coast between $S^t$ Raphaël and Cannes in the course of 1987. However, there is no obvious bimodal distribution separating the scar from the background in all four histograms like for water and land (lake Geneva). This is due to the relatively small size of the fire in terms of pixels (about 17), although this fire has been the largest one in France in the course of 1987. Another reason for the weakness of the signals is the degree of damage occasioned to the vegetation following the burning. The degree of damage can be at times so low that the signal measured does not differ much from that provided by the background. The pixels relative to the burned area must therefore be separated from the pixels characteristic of the background and the statistics of the former must be studied alone. This will be implemented in the training session of classes, first step for the classification of burn scars. The following steps will be developed in the next chapter.

Both the 88101 and 87107 scenes are trained in terms of burned and non burned vegetation. The training session defines the contours of local areas characteristic of burned and non burned vegetation and their statistics in the different channels. Statistics need to be produced in order to assess the general spectral properties of the selected training sets and in order to assess the usefulness of the information provided by each single channel. The usefulness is measured by the correlation coefficients.

The two selected training sets are called "scar" and "vegetation". In the 87107 scene, the training set "scar" consists of the area burned in the Tanneron Forest on the 23$^{rd}$ and 24$^{th}$ of August 1986. The corresponding training set is made up of the 17 pixels which appear reddish in the false color image (Image 7.11, left side). Knowing that the average ground size of a pixel in this part of France is 88 ha (since the $1^{o}\times1^{o}$ considered square represents an area of 110 km$\times$ 80 km, then the average pixel area is 0.8 km$\times$1.1 km or 0.88 km$^2$), the estimated size of this burned area, after 8 months, is 1500 ha. The original size of the fire was 7000 ha (about 80 pixels with the 88 ha average). This means that, for this particular fire, only one fourth of the original size of the fire is noticeable from space 8 months later. Therefore, either the vegetation has quickly regrown or the damage was not very pronounced. Nevertheless, only the pixels that have the spectral signature of a scar are picked up in the training session because the purpose is to study the spectral signature of a well defined scar. In this same scene, the class "vegetation" consists of a forested area next to the Tanneron forest and its training set is made up of 224 pixels. Statistics for these training sets give, in each one of the four channels of the mapped image, the mean pixel intensity, the standard deviation and the covariance matrix of the two classes. This information is summarized in Table 7.1 for the class "scar" and in Table 7.2 for the class "vegetation". The covariance matrices, the terms of which produce the correlation coefficients, are discussed later.

The average reflectance in channel 1 is greater for the class "scar" than that for the class "vegetation" (81.5 versus 52.5). On the other hand, the average reflectance in channel 2 is less for the class "scar" than that for the class "vegetation" (99 versus 101.5) and the estimated temperatures both in channels 3 and 4 are less for the class "scar" than those for the class "vegetation" (302.5°K versus 295°K for channel 3 and 295.5°K versus 292.5°K for channel 4). These average differences, though small in some channels, will enable us to spectrally differentiate the two classes.

The covariance matrix of a training set in four channels is of the form:

$$\Sigma = \begin{bmatrix} \sigma_1^2 & \sigma_{12} & \sigma_{13} \\ \sigma_{21} & \sigma_2^2 & \sigma_{23} \\ \sigma_{31} & \sigma_{32} & \sigma_3^2 \end{bmatrix}$$

The matrix is symmetric. The diagonal terms are the variances (the standard deviations squared) of the training set in the four channels. The off-diagonal terms indicate a correlation estimation of the pixel intensity in the different channels and are calculated from a sample of N pixels in the training set by the relation[5]:

$$\sigma_{ij} = \sum_{l=1}^{N} \frac{(x_i(l) - \mu_i)\,(x_j(l) - \mu_j)}{N-1}$$

$x_i(l)$ and $x_j(l)$ are the pixel intensity of the pixel $l$ in channels $i$ and $j$,

$\mu_i$ and $\mu_j$ are the averages of the training set in channels $i$ and $j$.

The correlation coefficient between channels $i$ and $j$ is[5]:

$$\rho_{ij} = \frac{\sigma_{ij}}{(\sigma_{ii}\sigma_{jj})^{1/2}}$$

If $\rho_{ij}$ is close to 1 or -1, then there is a strong linear dependence between the data of bands $i$ and $j$, whereas if it is close to 0, there is little dependence[5]. Furthermore, an average correlation coefficient for a particular channel can be defined by the relation:

$$\rho_i = \frac{\sum_{j=1, j\neq i}^{n} |\rho_{ij}|}{n-1}$$

where n is the number of channels. An average correlation coefficient close to 0 for a channel indicates that this channel provides usefull new information. On the other hand, an average correlation coefficient close to 1 indicates that the information provided by this channel is redundant with that of the other channels.

The covariance matrix for the training set "scar" in the 87107 scene is:

$$\begin{bmatrix} 11.640 & -5.158 & 4.107 & 2.610 \\ -5.158 & 30.434 & -3.474 & -0.218 \\ 4.107 & -3.474 & 3.009 & 1.579 \\ 2.610 & -0.218 & 1.579 & 1.013 \end{bmatrix}$$

The correlation coefficient for the training set "scar" in the 87107 scene are:

| $\rho_{12}$ | $\rho_{13}$ | $\rho_{14}$ | $\rho_{23}$ | $\rho_{24}$ | $\rho_{34}$ |
|---|---|---|---|---|---|
| -0.27 | 0.69 | 0.76 | -0.36 | -0.04 | 0.90 |

and the average correlation coefficients, for each single channel, are:

| $\rho_1$ | $\rho_2$ | $\rho_3$ | $\rho_4$ |
|---|---|---|---|
| 0.57 | 0.22 | 0.65 | 0.56 |

It turns out that channel 3 is the more correlated to the other ones ($\rho_3 = 0.65$). Since channel 3 is subject to noise and since channels 3 and 4 are calibrated to give the same information, channel 3 would be the channel to discard to avoid redundancy and

misclassifications of pixels if a classification of the scars was to be implemented with this training set. Other training sets will confirm this statement.

The covariance matrix for the training set "vegetation" in the 87107 scene is :

$$\begin{bmatrix} 59.900 & 69.821 & 15.488 & 8.861 \\ 69.821 & 101.700 & 18.111 & 10.249 \\ 15.488 & 18.111 & 4.546 & 2.607 \\ 8.861 & 10.249 & 2.607 & 1.760 \end{bmatrix}$$

The correlation coefficient for the training set "vegetation" in the 87107 scene is:

| $\rho_{12}$ | $\rho_{13}$ | $\rho_{14}$ | $\rho_{23}$ | $\rho_{24}$ | $\rho_{34}$ |
|---|---|---|---|---|---|
| 0.89 | 0.94 | 0.86 | 0.84 | 0.76 | 0.92 |

and the average correlation coefficients, for each single channel, are:

| $\rho_1$ | $\rho_2$ | $\rho_3$ | $\rho_4$ |
|---|---|---|---|
| 0.89 | 0.83 | 0.90 | 0.84 |

Once more, it turns out that channel 3 is the more correlated to the other ones ($\rho_3$ = 0.90). It confirms the conclusion drawn for the previous training set.

In the 88101 scene, the class "scar" consists of the area burned on the 25$^{th}$ of August 1987 along the coast between S$^t$ Raphaël and Cannes. The corresponding training set is made up of the 25 pixels which appear reddish in the false color image (Image 7.11, right half). These 25 pixels correspond to a ground area of 2200 ha, whereas the original size of the fire, which occurred 8 months before the satellite image was taken, was about 2000 ha. Unlike the Tanneron fire, which occurred the previous year, vegetation must not have regrown in the 8 month period and/or the damage must have been severe. The class "vegetation" consists of the same forested area than that chosen in the training session for the 87107 scene. Therefore, it is also made of 224 pixels. Statistics also give, in each one

of the four channels, the mean pixel intensity, the standard deviation and the covariance matrices of the two classes. This information is summarized in Table 7.3 for the class "scar" and in Table 7.4 for the class "vegetation". The results are similar to those of the training sets in the 87107 scene. The average reflectance in channel 1 for the class "scar" is greater than that for the class "vegetation" (64 versus 47.5), the average reflectance in channel 2 is less for the class "scar" than that for the class "vegetation" (85.5 versus 104.5), and the estimated average temperatures in channels 3 and 4 are higher for the class "scar" than those for the class "vegetation" (298°K versus 293°K in channel 3, 293°K versus 291.5°K in channel 4). These differences will also enable us to spectrally differentiate the two classes.

The covariance matrix for the training set "scar" in the 88101 scene is:

$$\begin{bmatrix} 25.290 & 27.518 & 8.232 & 5.896 \\ 27.518 & 94.173 & 9.244 & 11.072 \\ 8.232 & 9.244 & 3.426 & 2.514 \\ 5.896 & 11.072 & 2.514 & 2.512 \end{bmatrix}$$

The correlation coefficient for the training set "scar" in the 88101 scene are:

| $\rho_{12}$ | $\rho_{13}$ | $\rho_{14}$ | $\rho_{23}$ | $\rho_{24}$ | $\rho_{34}$ |
|---|---|---|---|---|---|
| 0.56 | 0.88 | 0.74 | 0.51 | 0.72 | 0.85 |

and the average correlation coefficients by channel are:

| $\rho_1$ | $\rho_2$ | $\rho_3$ | $\rho_4$ |
|---|---|---|---|
| 0.72 | 0.59 | 0.74 | 0.77 |

These correlation coefficients are slightly different from those of the training set "scar" in the 87107 scene. In this particular case, the average correlation of channel 3 with the other channels is less than that of channel 4.

The covariance matrix for the training set "vegetation" in the 88101 scene is:

$$\begin{bmatrix} 35.083 & 37.287 & 5.697 & 2.541 \\ 37.287 & 63.444 & 7.418 & 3.430 \\ 5.697 & 7.418 & 2.035 & 1.139 \\ 2.541 & 3.430 & 1.139 & 0.839 \end{bmatrix}$$

The correlation coefficients for the training set "vegetation" in the 88101 scene are:

| $\rho_{12}$ | $\rho_{13}$ | $\rho_{14}$ | $\rho_{23}$ | $\rho_{24}$ | $\rho_{34}$ |
|---|---|---|---|---|---|
| 0.79 | 0.67 | 0.47 | 0.65 | 0.47 | 0.87 |

and the channel average correlation coefficients are:

| $\rho_1$ | $\rho_2$ | $\rho_3$ | $\rho_4$ |
|---|---|---|---|
| 0.64 | 0.63 | 0.73 | 0.60 |

Like for the two first training sets, channel 3 turns out to be the more correlated to the other channels. This confirms, once more, the uselessness of this channel to the classification process.

The separability of the classes depends upon the number of channels taken into account. The statistical separability of the training classes can be evaluated using various combinations of the available spectral bands. To estimate the separability, a new quantity called divergence is introduced. Its expression is[6]:

$$D_{ij} = \frac{tr\left( (C_i - C_j)\ (C_j^{-1} - C_i^{-1}) \right) + tr\left( (C_i^{-1} - C_j^{-1})\ (M_i - M_j)\ (M_i - Mj)^T \right)}{2}$$

This divergence can be scaled and is then called transformed divergence[6]:

$$D'_{ij} = 100\,(1 - exp\,(-D_{ij}0.125))$$

$M_i$ and $M_j$ are the $nb$ mean vector of the $i^{th}$ and $j^{th}$ class,

$nb$ is the total number of bands and, in this study, is equal to 4,

$C_i$ and $C_j$ are the $nb \times nb$ covariance matrices.

A high transformed divergence results in a good separability[6]. This figure allows us to predict which combination of bands would best maintain the separability of the classes. The corresponding results for the two training sets are displayed in Table 7.7. The highest separability (100%) occurs for the two training sets when combining the four available channels (1, 2, 3, and 4) or only channels 1, 2, and 4. A combination of only two channels results in a lower separability. For a two band combination (channels 3 and 4), the transformed divergence is lowered to 99.2% for the training sets in the 88101 scene and to 91.41% for the training sets in the 87107 scene.

The contours of the training set that was used for the Tanneron fire in the 87107 scene are now used in the 88101 scene in order to study the evolution of the reflectance of burned vegetation over a one year period of time. Table 7.5 summarizes the new statistics for this new training set in the 88101 scene. The average reflectance in channel 1 decreases by 37% (51.5 versus 81.5), whereas the average reflectance in channel 2 increases by 1.5% (101.5 versus 99). The estimated temperatures in channels 3 and 4 decrease by 3.8% and 2.2% (291°K versus 302.5°K in channel 3, 289°K versus 295.5°K in channel 4). The properties of burned vegetation therefore change drastically over a one year period. Vegetation regrows because the damage was not too severe or new trees are planted, which is a common practice in western Europe.

These 1988 statistics (Table 7.5) for an area burned in 1986 are moreover very close to those produced by the class "vegetation" in the 88101 scene (Table 7.4). In channel 1, the average reflectance differs by 4 units (51.5 versus 47.5), whereas in channel 2 it differs by 3 units (101.5 versus 104.5). In channels 3 and 4, the estimated mean temperatures differ respectively by 2 (291°K versus 293°K) and 2.5 (289°K versus 291.5°K). The area where the Tanneron fire took place in 1986, but the few remaining most damaged pixels, will be considered as a forested area in the 88101 scene due to the similarity of its spectral properties with those of vegetation. Therefore, one and a half year old scars do not show up well with the LAC imagery. This implies that only the 1988 imagery will be used to locate the scars of the fires that occurred in 1987.

All along, the estimated average temperatures in channels 3 and 4 have been different. This is due to the presence of noise in channel 3. Moreover, channels 3 and 4 are highly correlated. Therefore, the data provided by channel 3 will not be used in the classification process developed in the next chapter.

The statistics for the two classes called "scar" in the 87107 and 88101 training session are quite different in terms of the average reflectances in channels 1 and 2. The differences are illustrated in Table 7.6. There is a difference of 21.5% in channel 1 and of 13.7% in channel 2. This shows that the spectral signatures of scars are not unique and that they can vary in a great range due to the different damage experienced by the vegetation (Chapter V). This difference is also due to the impossibility of determining the exact contour of the scar because the resolution of the sensor employed is not very high (Chapter VI). This will therefore impinge upon the confidence of the classification of the burned areas. Nevertheless, common features between scars appear. All the burned areas reflect more than non burned vegetation in channel 1 and less in channel 2. Also, the estimated temperatures are higher for burned vegetation than for non burned vegetation.

TABLE 7.1

STATISTICS OF THE TRAINING SET "SCAR" IN THE 87107 SCENE

| Channel | 1 | 2 | 3 | 4 |
|---|---|---|---|---|
| Mean | 81.5 | 99 | 302.5 | 295.5 |
| Standard deviation | 3.5 | 5.5 | 1.5 | 1 |

TABLE 7.2

STATISTICS OF THE TRAINING SET "VEGETATION" IN THE 87107 SCENE

| Channel | 1 | 2 | 3 | 4 |
|---|---|---|---|---|
| Mean | 52.5 | 101.5 | 295 | 292.5 |
| Standard deviation | 8 | 10 | 2 | 1.5 |

TABLE 7.3

STATISTICS OF THE TRAINING SET "SCAR" IN THE 88101 SCENE

| Channel | 1 | 2 | 3 | 4 |
|---|---|---|---|---|
| Mean | 64 | 85.5 | 298 | 293 |
| Standard deviation | 5 | 10 | 2 | 1.5 |

TABLE 7.4

STATISTICS OF THE TRAINING SET "VEGETATION" IN THE 88101 SCENE

| Channel | 1 | 2 | 3 | 4 |
|---|---|---|---|---|
| Mean | 47.5 | 104.5 | 293 | 291.5 |
| Standard deviation | 6 | 8 | 1.5 | 1 |

TABLE 7.5

STATISTICS OF THE TANNERON SCAR IN THE 88101 SCENE

| Channel | 1 | 2 | 3 | 4 |
|---|---|---|---|---|
| Mean | 51.5 | 101.5 | 291 | 289 |
| Standard deviation | 4 | 9 | 1.5 | 1 |

TABLE 7.6

DIFFERENCES BETWEEN THE TRAINING SETS "SCAR"

IN THE 87107 AND 88101 SCENES

| Training set "scar" | 87107 | 88101 | Difference (%) |
|---|---|---|---|
| Mean reflectance channel #1 | 81.5 | 64 | 21.5 |
| Mean reflectance channel #2 | 99 | 85.5 | 13.7 |
| Mean temperature channel #3 | 302.5 | 298 | 1.5 |
| Mean temperature channel #4 | 295.5 | 293 | 0.8 |

TABLE 7.7

TRANSFORMED DIVERGENCE FOR THE TRAINING SETS "SCAR" AND "VEGETATION" IN THE 87107 AND 88101 SCENES

| Combination | 87107 | 88101 |
|---|---|---|
| 1234 | 100 | 100 |
| 123 | 100 | 100 |
| 124 | 100 | 100 |
| 134 | 99.98 | 100 |
| 234 | 99.84 | 100 |
| 12 | 100 | 100 |
| 13 | 99.76 | 99.96 |
| 23 | 99.01 | 100 |
| 14 | 99.95 | 96.03 |
| 24 | 82.98 | 100 |
| 34 | 91.41 | 99.20 |

FIGURE 7.1

HISTOGRAMS OF A 100×100 PIXEL SAMPLE IN CHANNELS 1, 2, AND 4

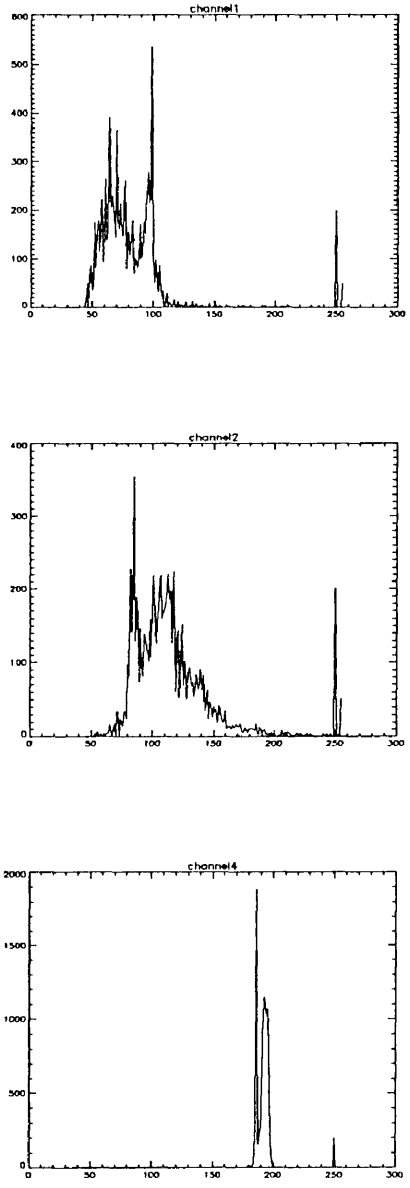

FIGURE 7.2

FALSE COLOR TABLE

**Chart a**

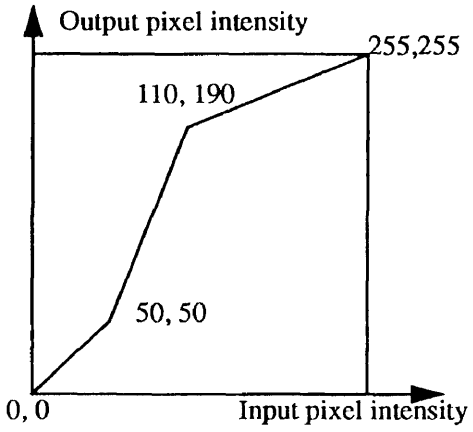


**Chart b**

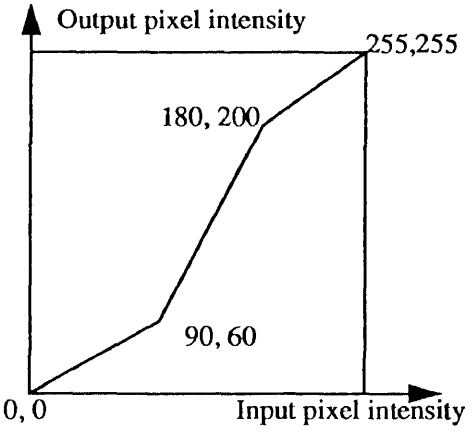


**Chart c**

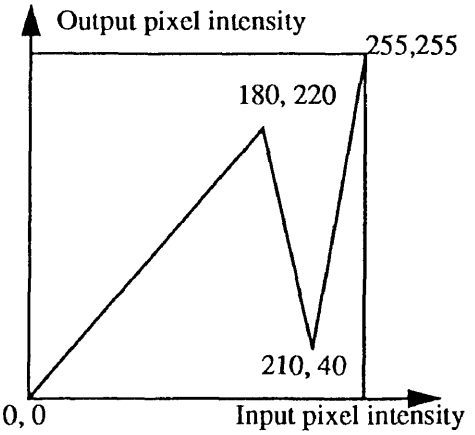

FIGURE 7.3

SYNOPTIC OF THE NDVI CALCULATION WITH CANTATA

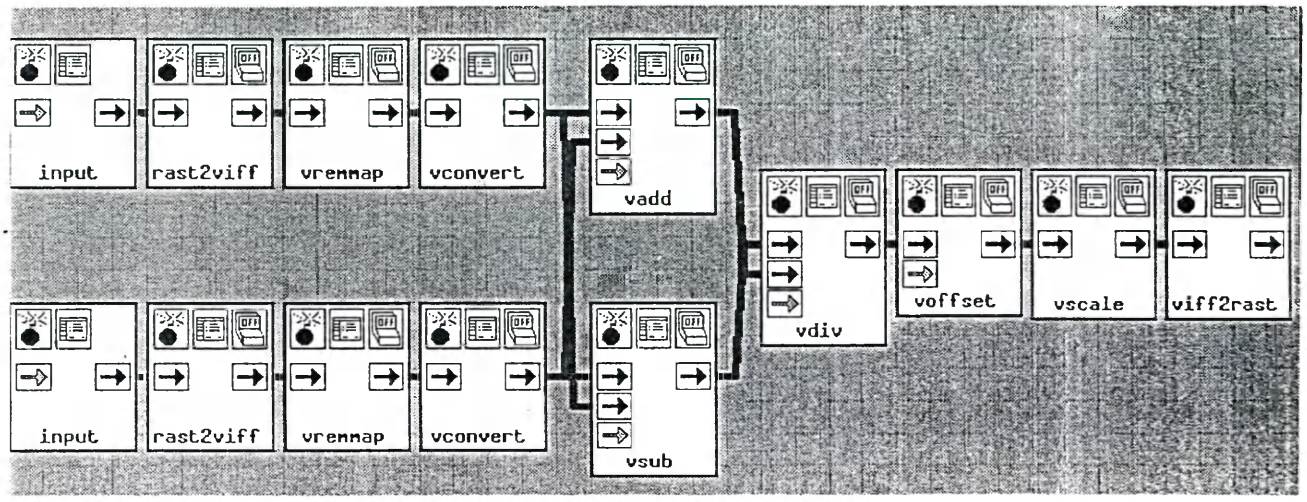


FIGURE 7.8

MAP OF THE TANNERON FIRE (AUGUST 23 & 24, 1986)

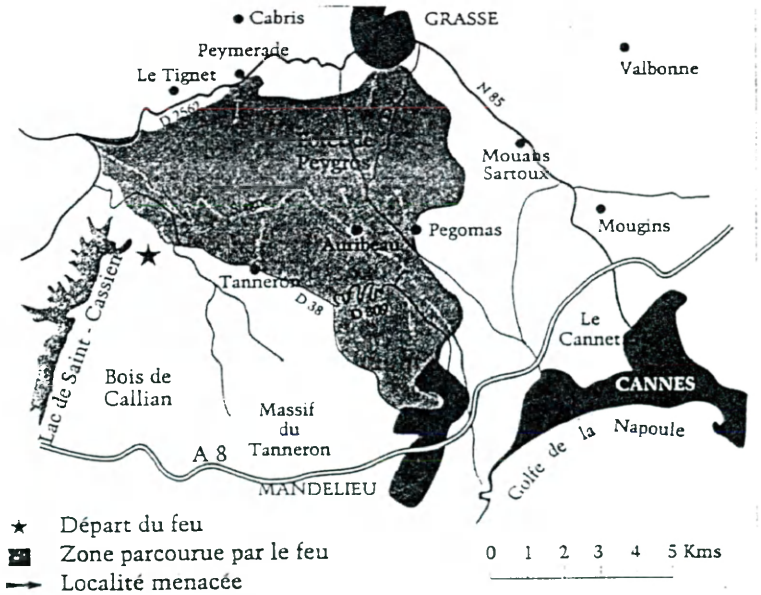

FIGURE 7.4

PSEUDO COLOR TABLE

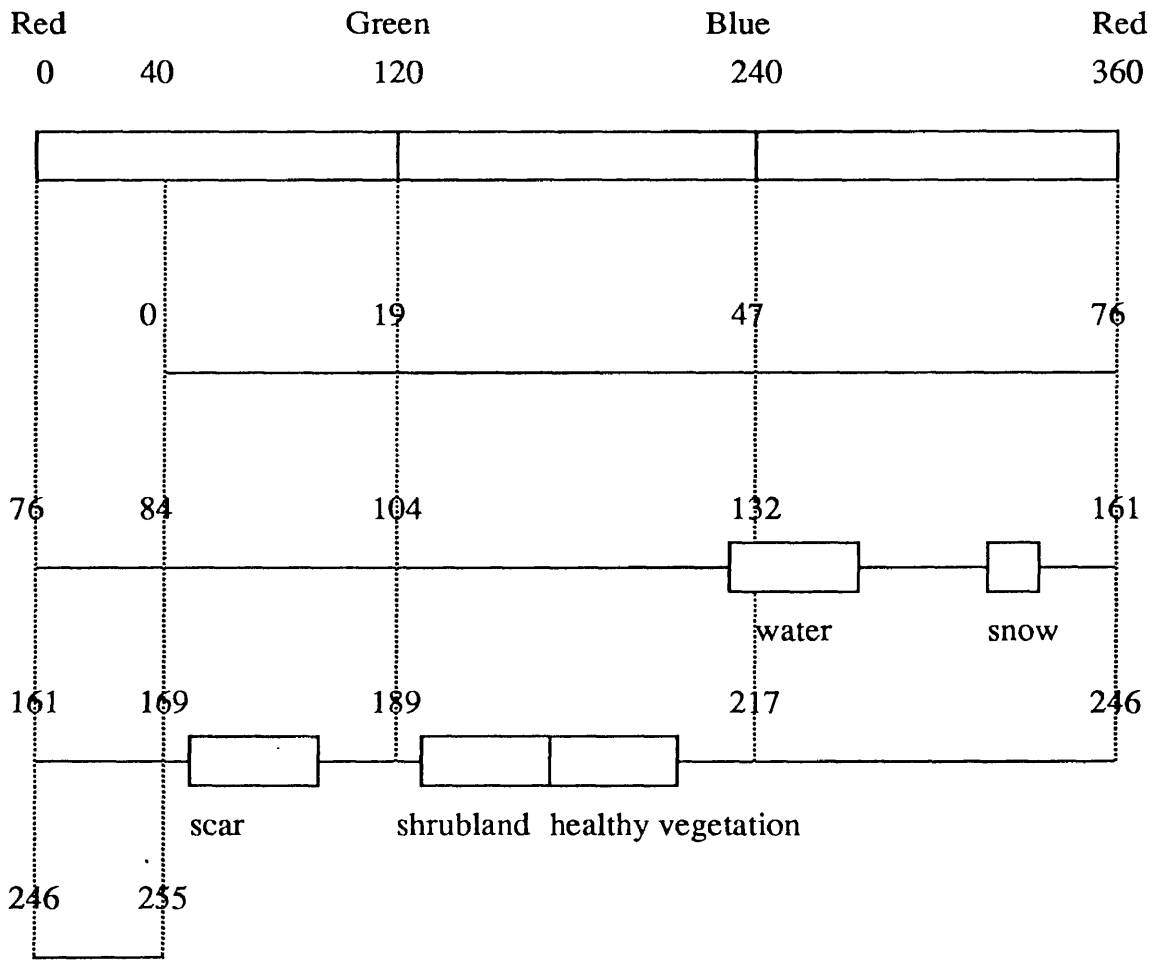

FIGURE 7.5

HISTOGRAMS OF WATER SURROUNDED BY LAND IN CHANNELS 1, 2, AND 4

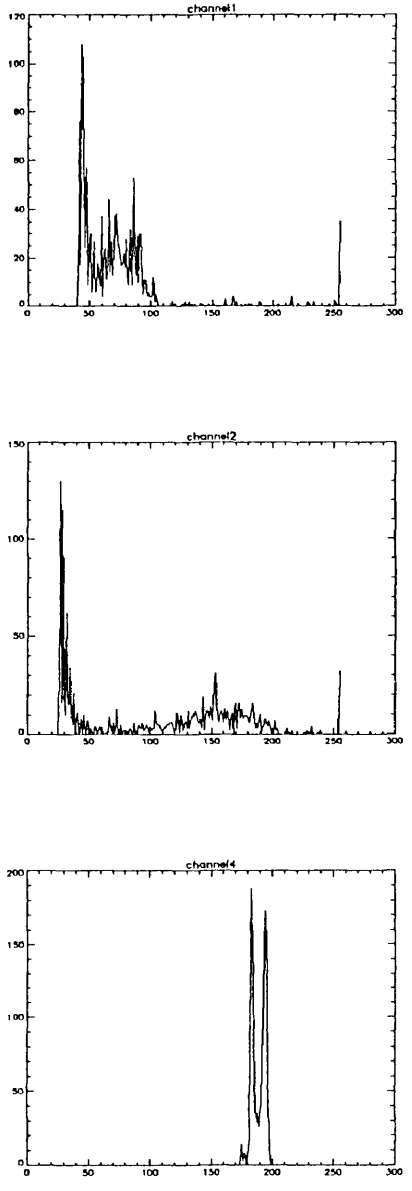

FIGURE 7.6

HISTOGRAMS IN THE 87107 SCENE OF AN AREA THAT BURNED IN 1987

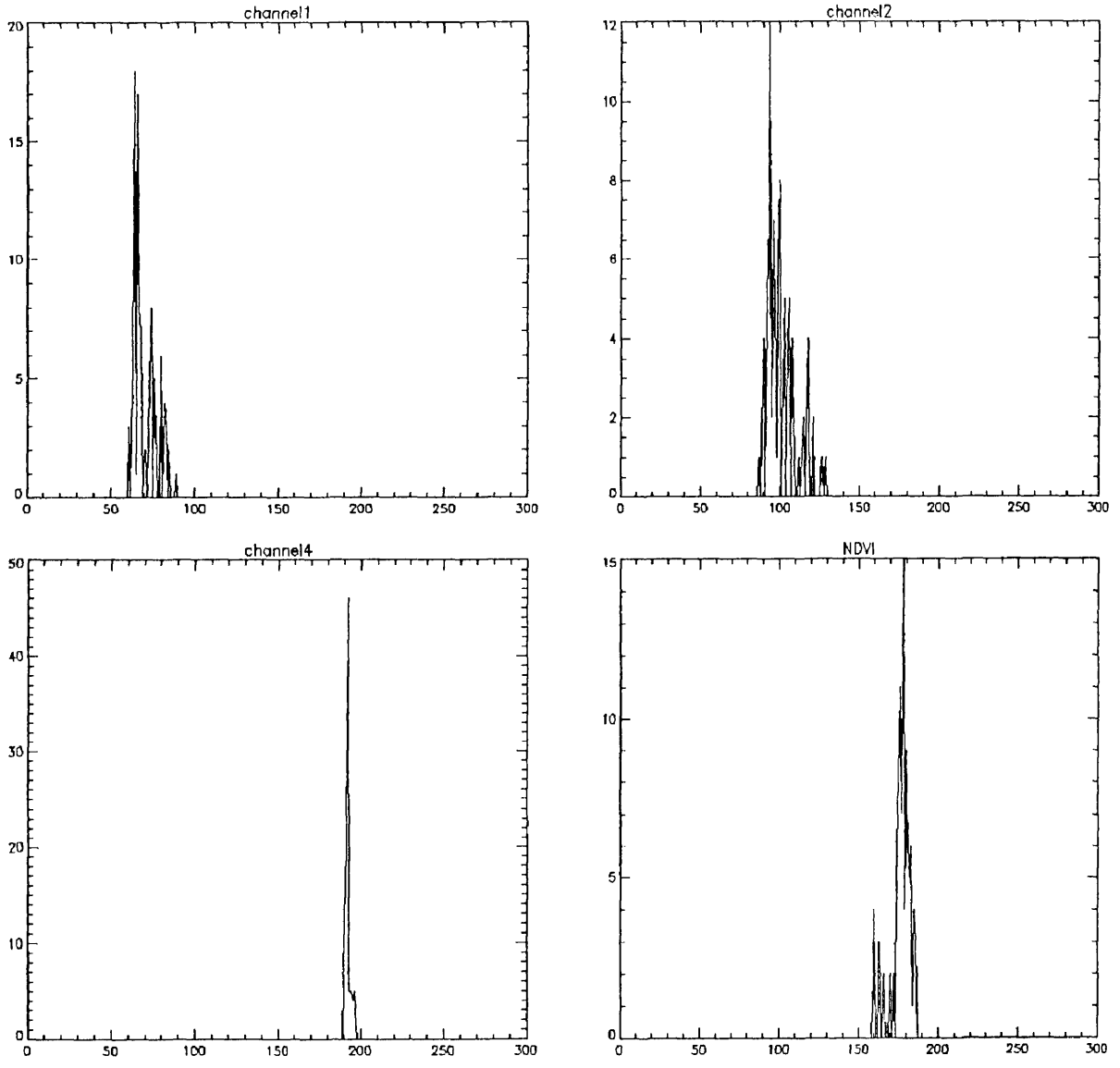

FIGURE 7.7

HISTOGRAMS IN THE 88101 SCENE OF AN AREA THAT BURNED IN 1987

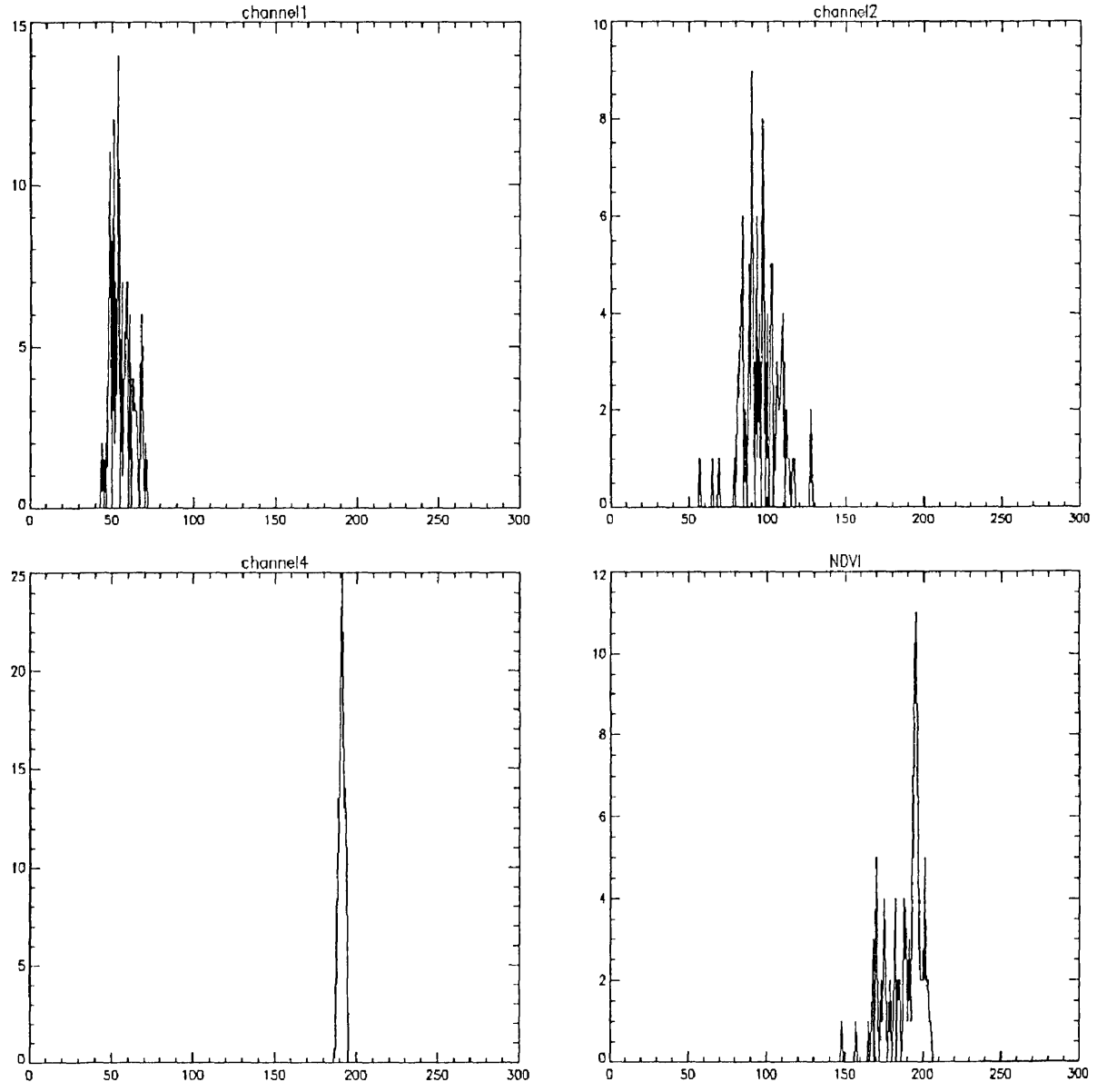

IMAGE 7.1

LAC IMAGE, APRIL 17, 1987, CHANNEL 2

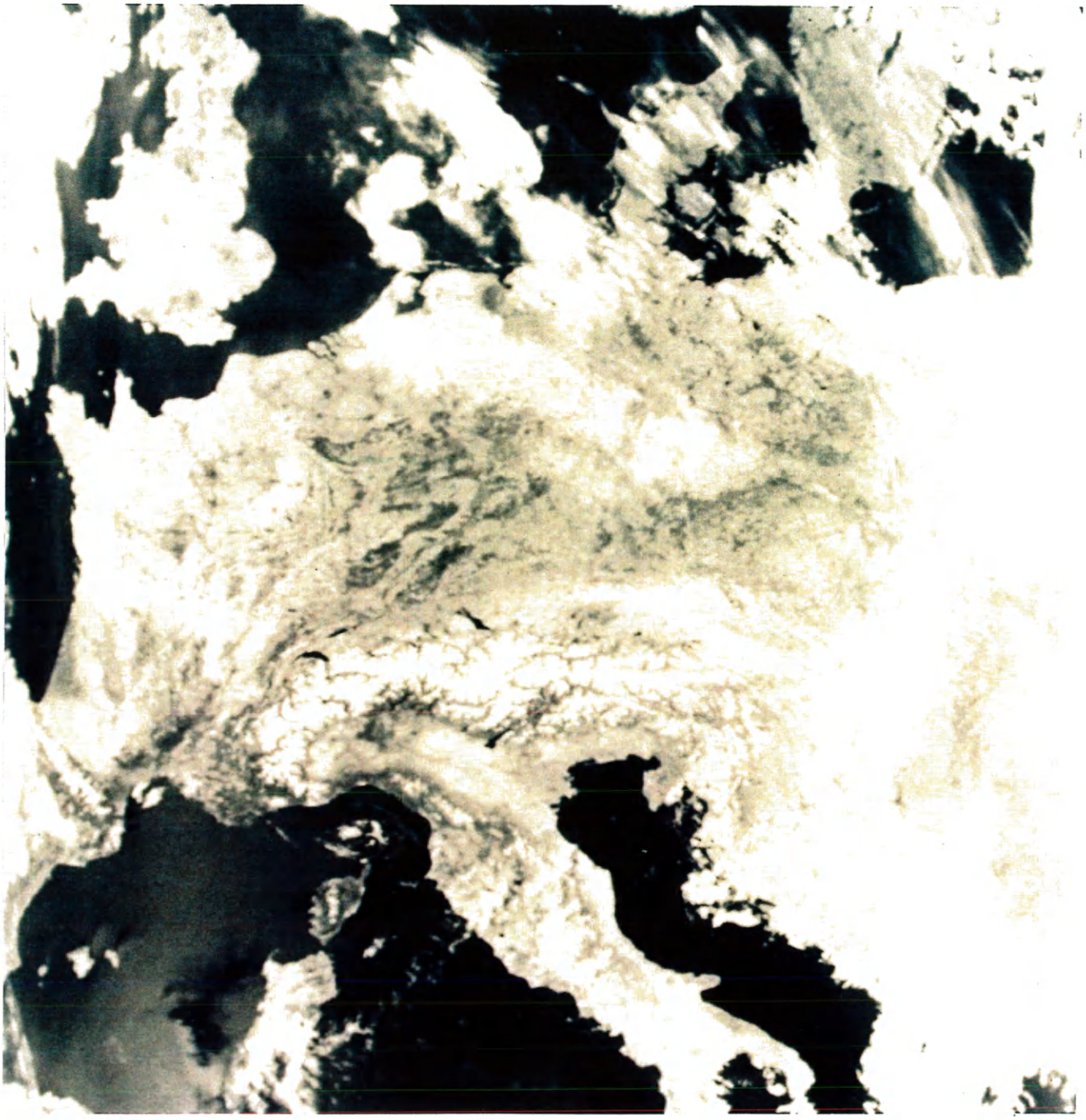

IMAGE 7.2

LAC IMAGE, APRIL 10, 1988, CHANNEL 2

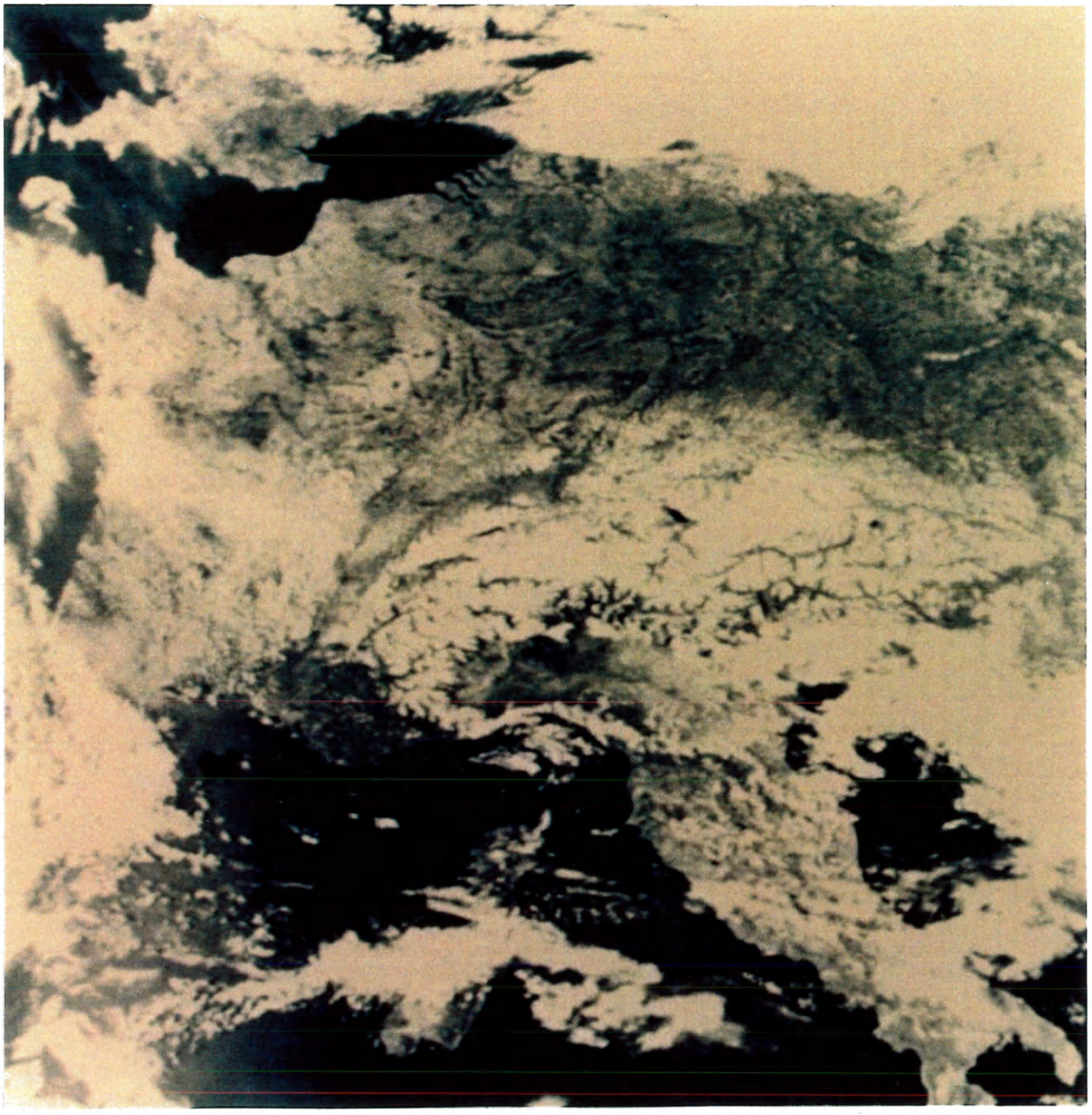

IMAGE 7.3

LAC IMAGE, APRIL 17,1987, CHANNEL 4

IMAGE 7.4

LAC IMAGE, APRIL 10, 1988, CHANNEL 4

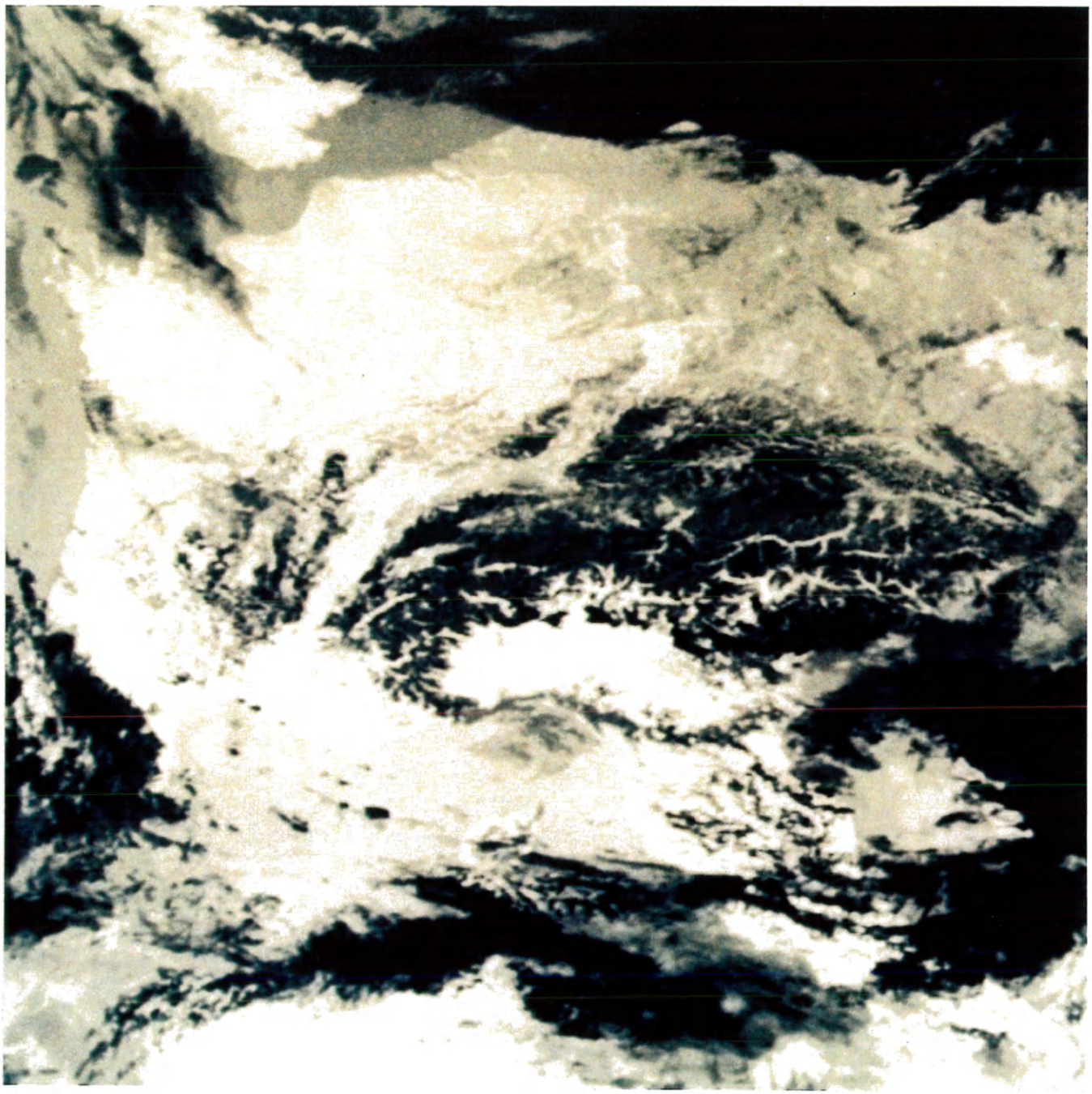

IMAGE 7.5

LAC IMAGE, APRIL 17, 1987, CHANNELS 1, 2, AND 4

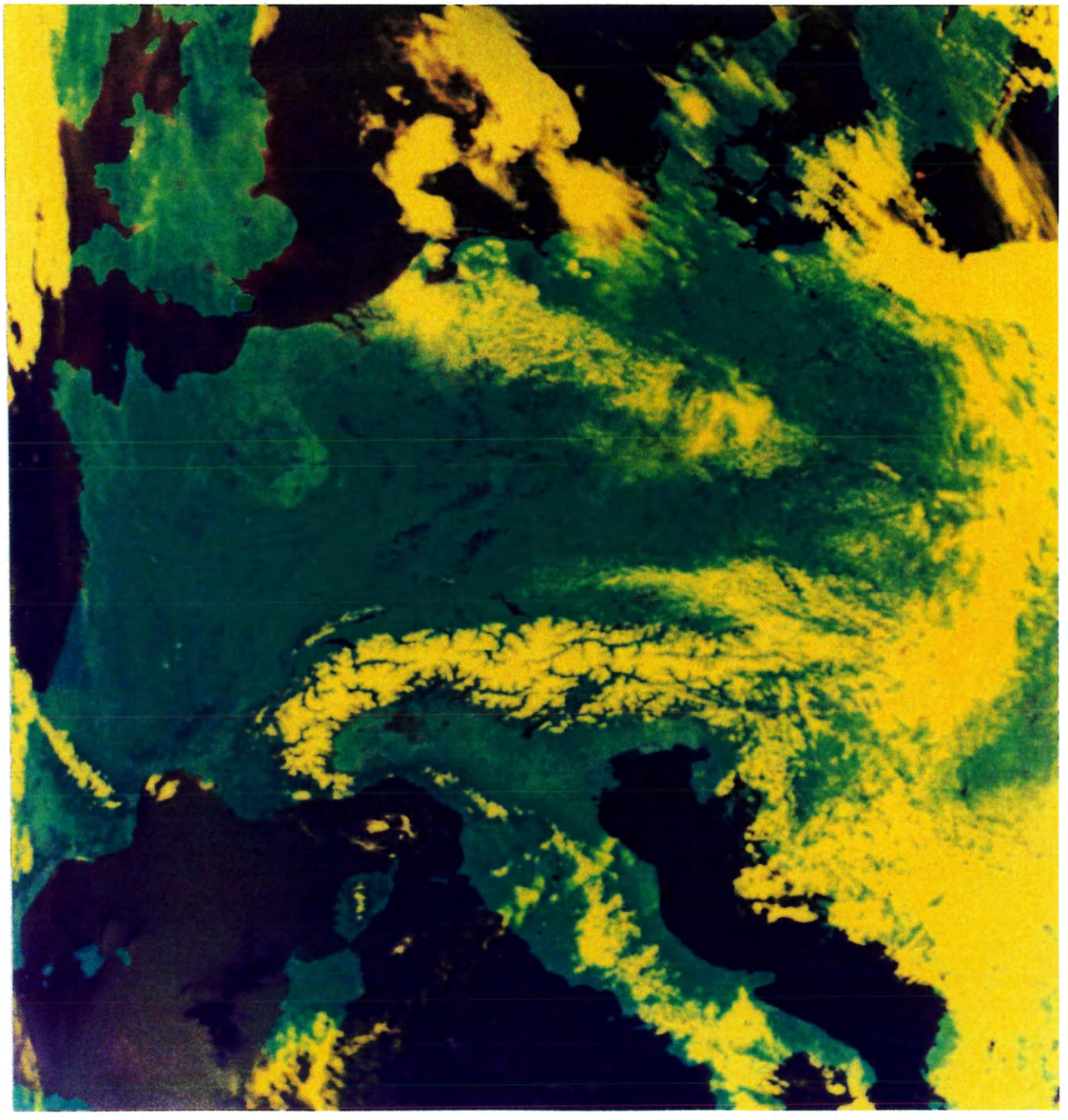

IMAGE 7.6

LAC IMAGE, APRIL 17, 1987, CHANNELS 1, 2, AND 4, COLOR TABLE

IMAGE 7.7

LAC IMAGE, APRIL 10, 1988, CHANNELS 1, 2, AND 4, COLOR TABLE

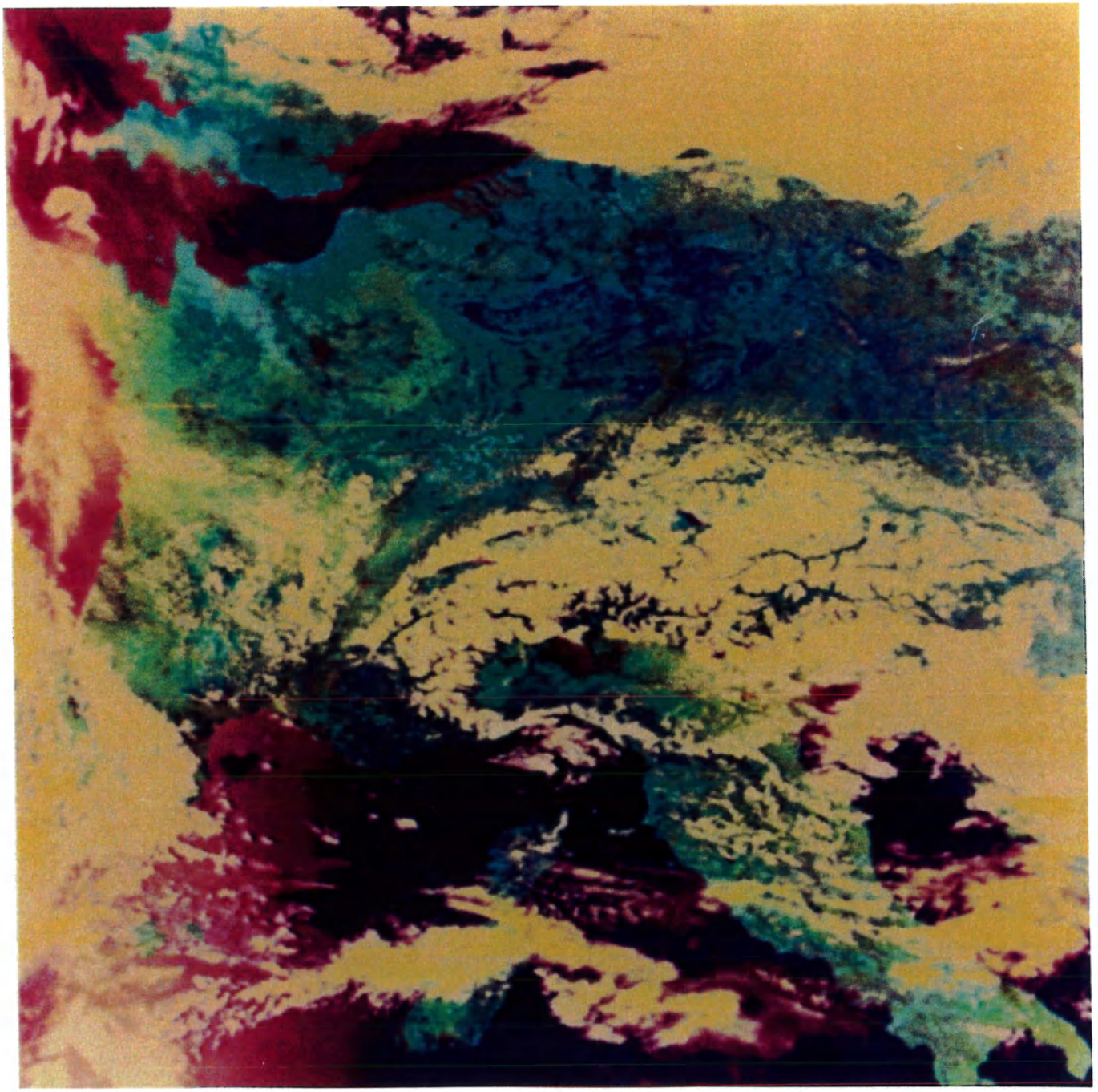

IMAGE 7.8

MAPPED LAC IMAGE, APRIL 17, 1987, CHANNELS 1, 2, AND 4

COLOR TABLE, (87107 SCENE)

IMAGE 7.9

MAPPED LAC IMAGE, APRIL 10, 1988, CHANNELS 1, 2, AND 4

COLOR TABLE (88101 SCENE)

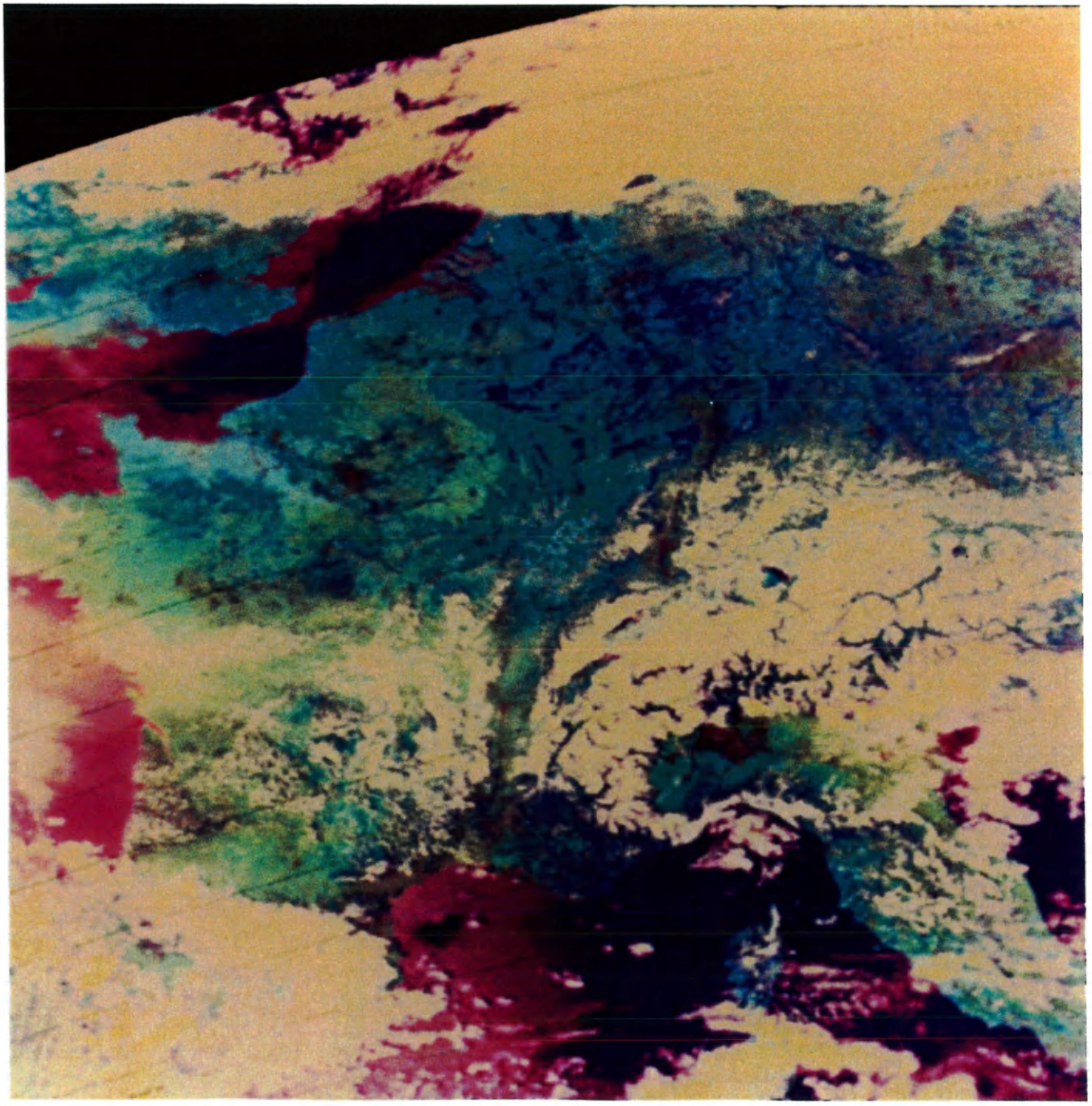

IMAGE 7.10

FRANCE, 87107 SCENE / 88101 SCENE

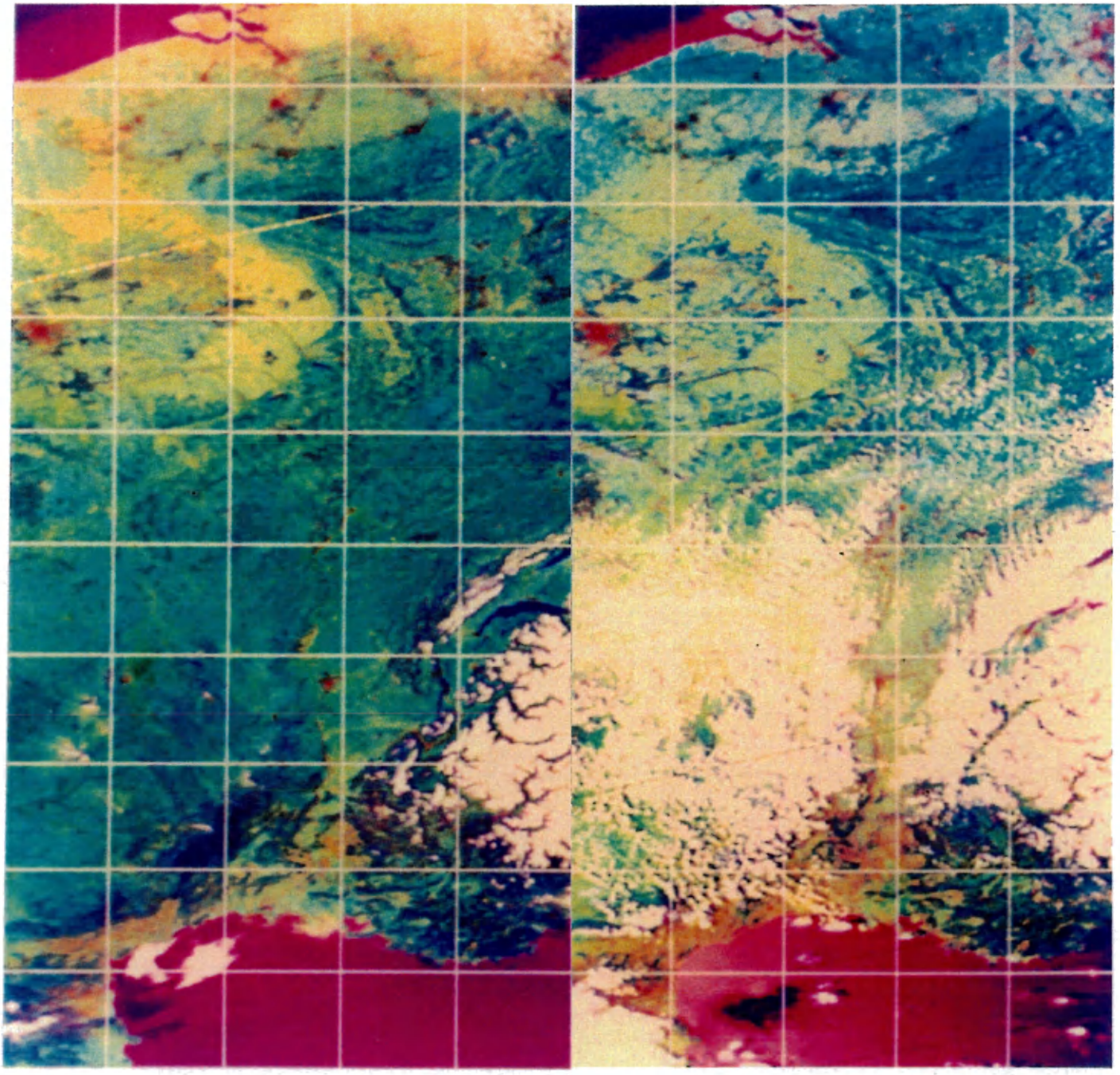

IMAGE 7.11

[43°N->44°N, 6°E->7°E], 87107 SCENE / 88101 SCENE

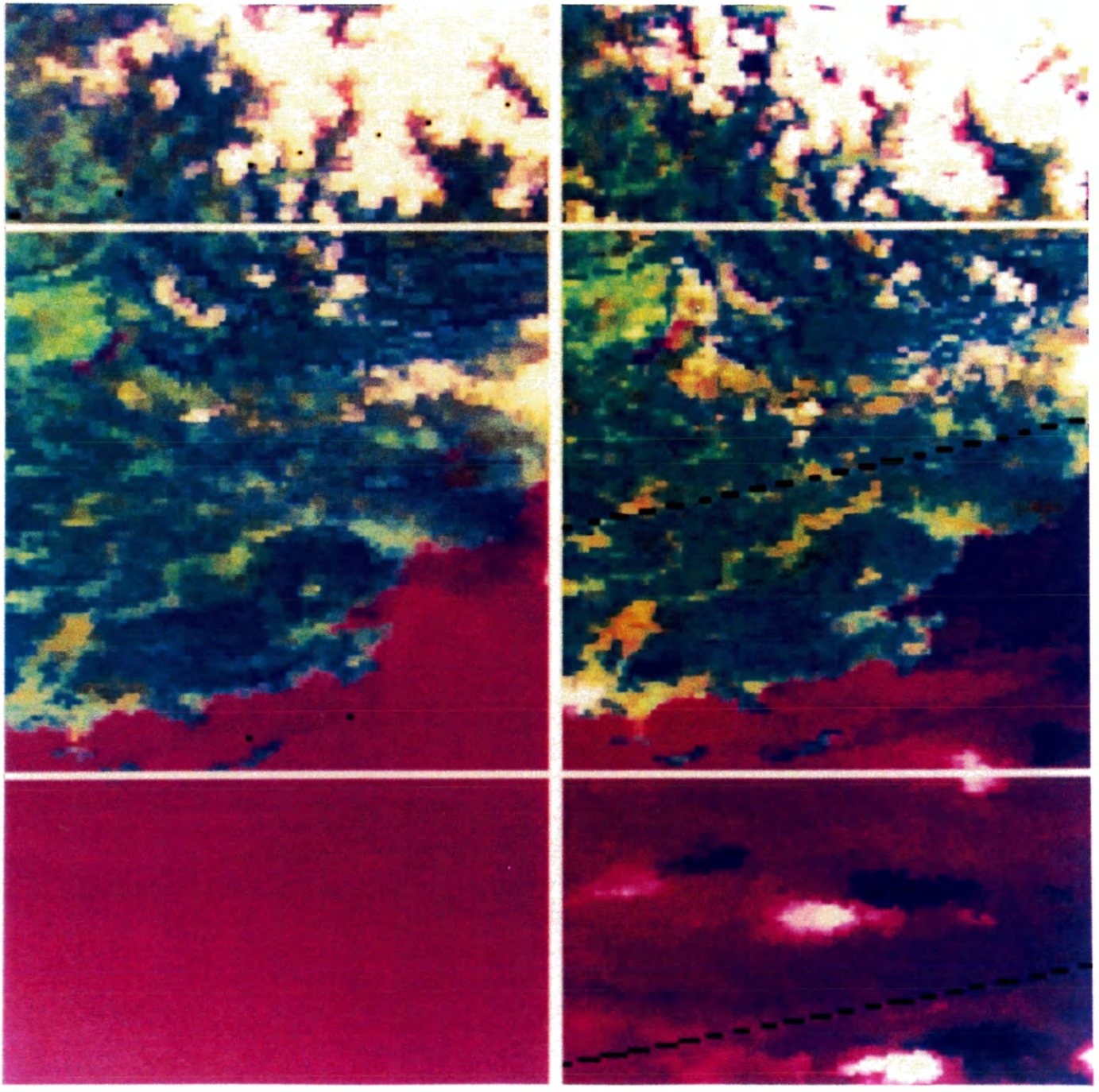

IMAGE 7.12

FRANCE, NDVI IMAGE, 87107 SCENE / 88101 SCENE

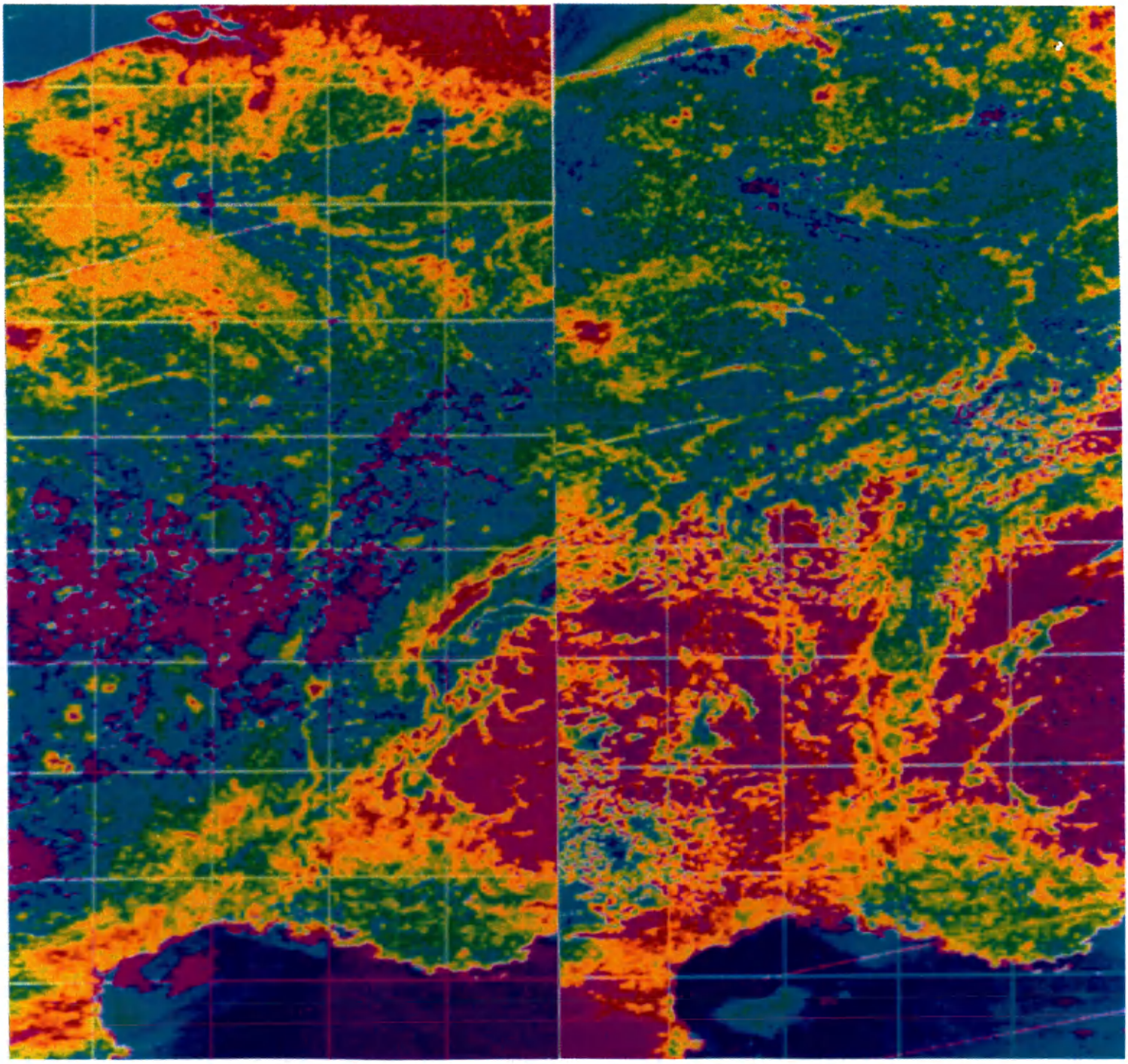

IMAGE 7.13

[43°N->44°N, 6°E->7°E], NDVI, 87107 SCENE / 88101 SCENE

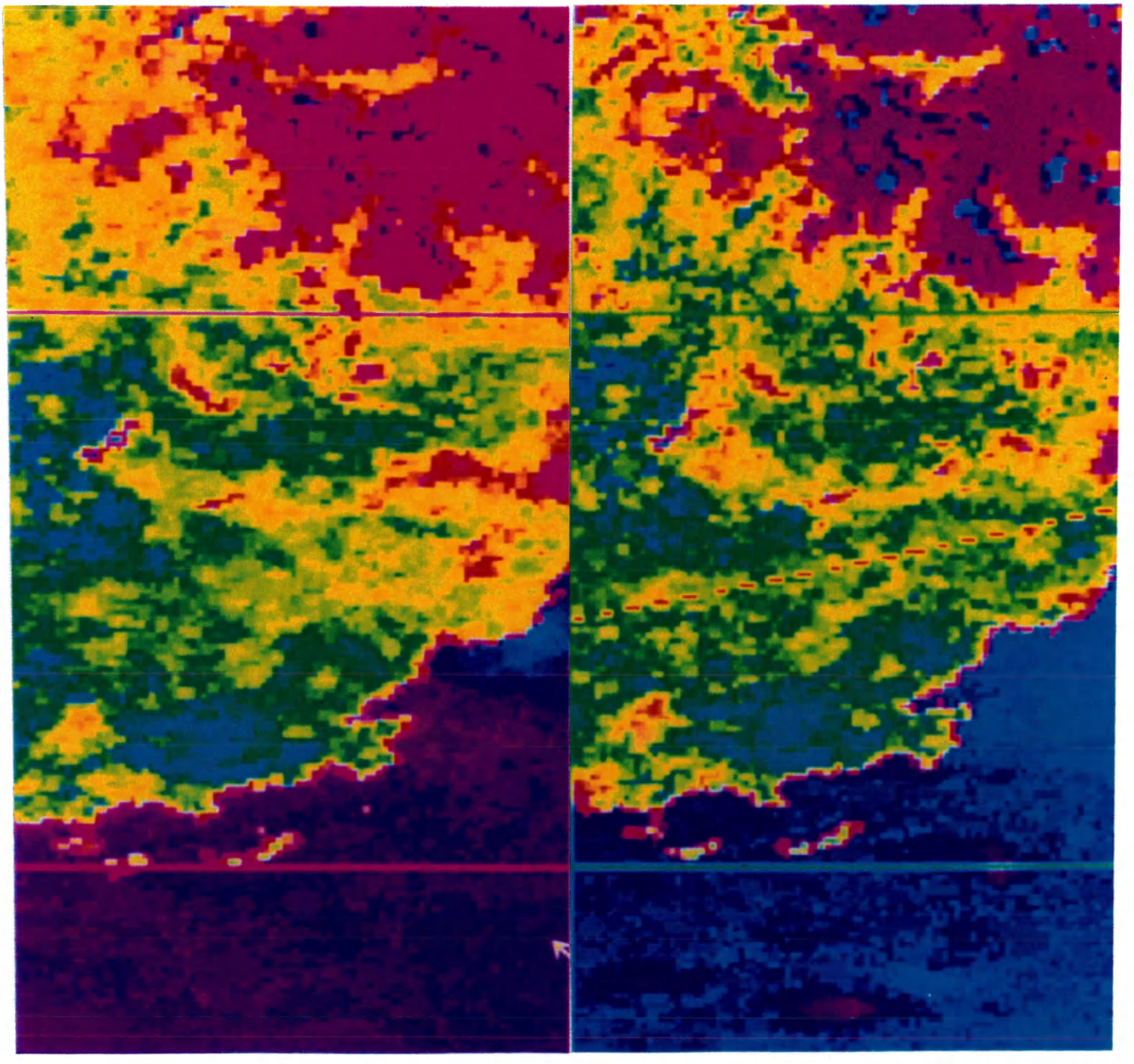

## NOTES TO CHAPTER VII

1. Kidwell, K. B. NOAA Polar Orbiter Data Users' Guide. National Oceanic and Atmospheric Administration, Satellite Data Services Division, U. S. Department of Commerce, 1991.

2. Pearson, II, F. Map Projections: Theory and Applications. Boca Raton, Florida: CRC Press, Inc., 1990.

3. Les Feux de Forêts. SECRETARIAT d'ETAT chargé de l'ENVIRONNEMENT et de la PREVENTION des RISQUES TECHNOLOGIQUES et NATURELS MAJEURS, Centre Régional de documentation pédagogique, Dijon, France, 1991.

4. Avery, T. E., Berlin, G. L. Fundamentals of Remote Sensing and Airphoto Interpretation. 5th edition, Macmillan Publishing Company, 1992.

5. Schowengerdt, R. A. Techniques for Image Processing and Classification in Remote Sensing. Academic Press, Inc., 1983.

6. System 600 Version 4.0 Command Reference CPU I (A-K) Volume II. International Imaging Systems, 1990.

# CHAPTER VIII

# REGIONAL CLASSIFICATION OF BURN SCARS

Spain and Portugal were chosen to implement the regional classification of burn scars because they account for 50% of the total forest burning in western Europe (Chapter IV). Therefore, they are likely to show more and larger scars than any other European country (Table 4.8). If this scar classification is not successful in the Iberian Peninsula, then it won't be applicable on a regional scale for the rest of Europe because there is less burning in the other countries and the scars in the rest of Europe are likely to be smaller than in Spain and Portugal (Table 4.8).

The two scenes that are presently used are the NOAA AVHRR 87128 and 88085 scenes (Images 8.1 and 8.2). This choice has been justified in Chapter VI. All the steps described in the previous chapter and leading to the mapped scenes have also been applied but will not be explained in full detail again. The 87128 and 88085 scenes are both mapped with a latitude resolution of 100 pixels per degree, starting at $35^{o}$N and ending at $45^{o}$N, and with a longitude resolution of 100 pixels per degree, starting at $10^{o}$W and ending at $5^{o}$E. The dimension of the mapped images is therefore 1500 pixels $\times$1000 pixels. The mapped scenes are displayed in Image 8.3 for the 87128 scene and in Image 8.4 for the 88085 scene.

Two factors that will effect the accuracy of the scar classification can be pointed out when looking at these two mapped images. Firstly, there are some sparse clouds on both images. They will eventually reduce the scar classification accuracy. However, these

clouds were not visible on the corresponding Meteosat images (Images 6.1 and 6.2). Secondly, overall reflectance differences between the western and eastern part of the Iberian Peninsula reflect differences in ecosystems (Figure 3.8).

The classification of the burned scars in Spain and Portugal will be carried out using the System 600 by International Imaging Systems, available at the NASA Langley Research Center. The classification can be supervised or unsupervised[1]. On the one hand, the unsupervised classification uses the computer to generate class statistics based on the histograms of the whole scene and then to iteratively process the image[1]. This unsupervised classification will be implemented later in this chapter and its results will be compared to those of the supervised classification. On the other hand, the supervised classification is made up of four steps[2]. In the first step, the user defines the contours of areas that are samples of particular classes in a training session and saves them in a file. A class is a cluster of pixels that have the same spectral properties and that are supposed to be characteristic of the same surface. For example, the class "scar" represents the burned areas. In the second step, the System 600 generates a pixel value file with all the pixels inside the contours previously defined. In the third step, the computer generates a statistics file from the pixel value file. The statistics of the classes will be assumed equal to those of the corresponding samples (training sets). These three steps have already been applied for known scars in southern France (Chapter VII). The fourth and last step is the classification itself. The classification can be based on several principles, i.e. the minimum distance principle or the maximum likelihood principle[1]. The former is characterized by its computational simplicity and will be implemented first. The latter, more complex, will be applied later in this chapter. The results from the two principles will finally be compared. For both classifications, training sets and statistics, like those for the scars in southern France, have first to be computed.

The first step in carrying out a supervised classification, whatever the principle is, is to define training sets which are characteristic of the classes desired. As in the previous chapter, two training sets are defined and are called: "scar" and "vegetation". The training set "vegetation" has to be selected so that actual vegetation be classified as vegetation and not as scar due to a possible spectral overlap of the training sets. This step, as demonstrated in the previous chapter, is very important. Unlike southern France (Chapter VII), no specific information pertaining to actual fires, which occurred in Portugal and Spain in 1987, has been found. However, with the case study of the two large fires in southern France in 1986 and 1987, it is possible to pick up a scar in the 88085 scene by comparing same areas in the two false color images (87128 and 88085 scenes) and using the same color table. The reference scar is found in Portugal and its center coordinates are: $7^{o}$ 40' W and $40^{o}$ 10' N. The reddish spot in the right half of Image 8.5, which is a close-up of a forested area in Portugal from the 88085 scene, appeared sometime in 1987 because no such spot exists in the left half of Image 8.5 (87128 scene) . This is confirmed by the corresponding NDVI images (Image 8.6). The scar appears red in the 88085 scene (right half), whereas it does not show up in the 87128 scene (left half). Therefore, training sets for the two classes can be defined. Their contours are shown on Image 8.7. The training set for the class "scar" (green contour) is made of 59 pixels and the training set for the class "vegetation" (blue contour) is made of 544 pixels. The statistics in channels 1, 2, and 4 give the average pixel intensity, the standard deviation, and the covariance matrix of the two training sets. These statistics, for the training sets "scar" and "vegetation", are summarized in Table 8.1 and in Table 8.2. The covariance matrices are discussed later.

The data in channel 3 has been discarded following the results of the case study in Chapter VII. Because this channel is subject to much noise (Chapter VII) and because it is supposed to give the same information as channel 4 (high correlation), it will not be used in the classification step.

Similar to the two scars studied in southern France, the mean reflectance in channel 1 of the training set "scar" is greater than that of the training set "vegetation" (69 versus 52.4) and the mean reflectance in channel 2 of the training set "scar" is less than that of the training set "vegetation" (94.5 versus 109.8). The estimated temperature provided by channel 4 is greater for the training set "scar" than that for the training set "vegetation" (295.6$^{o}$K versus 294.7$^{o}$K). This is due to the cooling effect of the evapo-transpiration of vegetation.

The covariance matrix for the training set "scar" in the 88085 scene is:

$$\begin{bmatrix} 80.137 & 69.189 & 11.367 \\ 69.189 & 170.116 & 14.222 \\ 11.367 & 14.222 & 4.619 \end{bmatrix}$$

The corresponding correlation coefficients are:

| $\rho_{12}$ | $\rho_{14}$ | $\rho_{24}$ |
|---|---|---|
| 0.59 | 0.62 | 0.51 |

All three channels are moderately correlated. The average correlation on the three channels is 0.57. The correlation coefficient between channels 1 and 2 is very similar to that of the training set "scar" in the 88101 scene (0.59 versus 0.56 for $\rho_{12}$). On the other hand, $\rho_{14}$ and $\rho_{24}$ are not similar (0.62 versus 0.74 and 0.51 versus 0.72, respectively) because the data in channel 4 depends upon the temperature. The way channels 1 and 2 are correlated is similar although the covariance matrices are not equal. On the other hand, the correlation coefficient $\rho_{12}$ is very different from that of the training set "scar" in the 87107 scene (0.59 versus 0.27). This shows that these two scars are spectrally different.

The covariance matrix for the training set "vegetation" in the 88085 scene is:

$$\begin{bmatrix} 34.552 & 35.839 & 3.504 \\ 35.839 & 100.676 & 4.414 \\ 3.504 & 4.414 & 3.609 \end{bmatrix}$$

The corresponding correlation coefficients are:

| $\rho_{12}$ | $\rho_{14}$ | $\rho_{24}$ |
|---|---|---|
| 0.61 | 0.28 | 0.23 |

All three channels are not very correlated for the training set "vegetation" in the 88085 scene, unlike those in the 87107 and 88101 scenes (Table 8.4). It is an indication of a slightly different vegetation.

In order to establish that the spotted reddish area in the 88085 scene results indeed from a fire that occurred in the course of 1987, the statistics of this area in the 87128 scene must be compared to those of the 88085 scene. If the same contours for the training sets "scar" and "vegetation" as those displayed in Image 8.7 are used, then new statistics for these two sets are obtained for the 87128 scene. They are summarized in Tables 8.5 and 8.6. These training sets are very much alike because the average reflectances in channel 1 and 2 are similar (49.3 versus 55.4 and 123.8 versus 116.2 respectively) and the average temperatures in channel 4 are also similar (298.8°K versus 300.2°K). The two training sets are thus both characteristic of vegetation because their spectral properties in channels 1 and 2 are similar to those of the training set "vegetation" in the 88085 scene (Table 8.2).

To better assess the similarity between two training sets, the spectral properties (assumed to be normal distribution curves) of both training sets have to be compared channel by channel. The overlap of two normal distributions is illustrated in Figure 8.1. The estimation of the overlap is based on the value of the area under the two curves. In

order to find the value of the crossover points ($x_1$ and $x_2$), the following equation (expressions for normal distribution curves) has to be solved:

$$\frac{1}{\sigma_1\sqrt{2\pi}}exp\left(-\frac{1}{2}\left[\frac{x-\mu_1}{\sigma_1}\right]^2\right) = \frac{1}{\sigma_2\sqrt{2\pi}}exp\left(-\frac{1}{2}\left[\frac{x-\mu_2}{\sigma_2}\right]^2\right)$$

where $\sigma_1$ and $\mu_1$ are the standard deviation and the average pixel intensity, in one particular channel, of the normal distribution for the training set "vegetation" in the 87128 scene, whereas $\sigma_2$ and $\mu_2$ are the standard deviation and the average pixel intensity, in the same channel, of the normal distribution for the training set "vegetation" in the 88085 scene. Once $x_1$ and $x_2$ are known, the probability that x be more than $x_1$ and less than $x_2$ for both distribution is represented by the area A, the probability that x be less than $x_1$ for both distribution is represented by the area B, and the probability that x be greater than $x_2$ for both distribution is represented by the area C. These three probabilities can be looked up in a "normal curve areas" table[3] when using the intermediary variable $z_i$ defined by:

$$z_i = \frac{x-\mu_i}{\sigma_i}$$

The three resulting probabilities are then added up to yield the overlap between the two training sets in one particular channel. This operation has to be repeated in all three channels. The results are displayed in Table 8.7 for the training set "vegetation" in the 87128 and 88085 scenes. In channels 1 and 2, the overlap is: 80% and 76.3%, respectively. On the other hand, in channel 4, the overlap is small because the temperature can vary considerably between two different days. An average overlap of 75% is therefore characteristic of identical areas temporally separated.

The spectral properties of the training set "scar" in the 88085 scene (Table 8.1) can be compared, using the same method, to those of training sets "scar" in the 87107 and

88101 scenes (Tables 7.1 and 7.3). The spectral overlaps between the scar in Portugal and the scars in France are quantified for each channel in Tables 8.8 and 8.9. The average overlap in channels 1 and 2 between the scar in Portugal and the scar in the 88101 scene is about 65%. Although it is less than for the two training sets "vegetation" previously mentioned, it is an indication of the similarity of these two scars. On the other hand, the average overlap for channels 1 and 2 between the scar in Portugal and the scar in the 87107 scene is low (42%). These two last scars are not very much alike.

Table 8.10 shows the transformed divergence for the two training sets "scar" and "vegetation" in the 87128 and 88085 scenes. The transformed divergence in the 88085 scene is greater than that for the 87128 scene for all combinations but one because the training set "scar" in the 88085 scene is characteristic of an actual scar whereas, in the 87128 scene, it is not. The fire, at this particular location, occurred indeed in 1987. The statistical separability of the two training sets "scar" and "vegetation" in the 87128 scene is low because they both are characteristic of vegetation.

The fourth and final step of the classification process is the classification itself. It can be now implemented in the 88085 scene using the two training sets and their statistics. It will not be implemented in the 87128 scene because it has been established in the previous chapter that one and a half year old and relatively small scars do not show up in general with the LAC imagery. The minimum distance classification is first explained and then implemented.

The minimum distance principle assumes that the covariance matrices for the two different classes are equal and that the off diagonal terms are null[1]. If they are not, then

they are forced to zero. Therefore, the considered covariance matrix is of the form:

$$\Sigma_0 = \begin{bmatrix} \sigma_1^2 & 0 & 0 \\ 0 & \sigma_2^2 & 0 \\ 0 & 0 & \sigma_3^2 \end{bmatrix}$$

The classification decision is based on the following equation[4]:

$$Cl\,(x, y) = MIN_{c=1}^{nc} \left[ \sum_{b=1}^{nb} \left( \frac{X_b\,(x, y) - \mu_{b,c}}{\sigma_{b,c}} \right)^2 \right]$$

*Cl* is the class number assigned the pixel with coordinates *x,y*,

*c* is the class number being currently tested,

*nc* is the total number of classes,

*b* is the band number being currently tested,

*nb* is the total number of bands,

$X_b\,(x,y)$ is the input pixel with coordinates *x,y*, in band *b*, being tested,

$\mu_{b,c}$ is the mean vector of the class *c*, in band *b*, being tested,

$\sigma_{b,c}$ is the standard deviation of the class *c* being tested,

*MIN* returns the value of the class *c* that produces the minimum.

Now the scene 88085 can be classified using this last principle in terms of burned and non burned vegetation. In order to prevent misclassifications, a threshold is used. Since the classes are defined by a three dimensional normal distribution of points, the rejected points will be outside a three dimensional volume delimited by the threshold value, proportional to the standard deviation $\sigma$ of the three dimensional normal distribution. For different values of the threshold, the number of pixels classified as "scar" or as "vegetation" is shown in Table 8.11.

The populations of the training sets "scar" and "vegetation" vary greatly with the threshold selected. A large threshold results in an important population. The population distribution of the class "scar" tends to concentrate on the coast and in cloud shadows when the threshold is greater than one standard deviation. Since these pixels are evidently not scars, they should not be included in the class "scar". Therefore, the best class population is that which includes the maximum number of pixels inland and the minimum on the coast. After visualization, the threshold of one standard deviation turns out to be the one that minimizes the number of pixels on the coast and maximizes the number of pixels inland (Image 8.8). Nevertheless, since the training set "scar" was located in the western part of the Iberian peninsula, most of the pixels that belong to the class "scar" show up also in the western part. This confirms that the ecosystems between the eastern and western part are different.

Since the results of the minimum distance classification are not very satisfying due to the presence of coastal pixels, a more complex classification method, called the maximum likelihood principle, is now introduced. This principle will be implemented with the same training sets as those previously used for the minimum distance classification. The advantage of this new method is that the class decision minimizes the average probability of classification error[1]. The pixels are represented by three element vectors $[X] = [x_1, x_2, x_3]^T$. Since the training sets are assumed to have a normal distribution in all three channels, they are represented by a mean vector $[\mu] = [\mu_1, \mu_2, \mu_3]^T$ and a standard deviation vector $[\sigma] = [\sigma_1, \sigma_2, \sigma_3]^T$. The three dimensional probability functions of the two classes "scar" and "vegetation" overlap in every channel. The probability of classification error is proportional to the three dimensional overlapping portions of the probability functions. The multivariate form for the probability function of a three dimensional normal distribu-

tion is[1]:

$$P([X]|i) = \frac{1}{|\Sigma_i|^{1/2}(2\pi)^{3/2}} exp\{-\frac{1}{2}(([X]-[\mu_i])^T \Sigma_i^{-1}([X]-[\mu_i]))\}$$

P([X]|i) is the probability that a vector [X] belongs to class i,

$\sum_i$ is the covariance matrix of class i,

$|\sum_i|$ is the determinant of the covariance matrix,

$\sum_i^{-1}$ is the inverse covariance matrix.

In order to minimize the overlapping, and consequently to minimize the classification error, each three dimensional probability density function may be scaled by a priori probabilities p(i). The a priori probability is the probability that the class i occurs in the image. The new term P([X]|i) p(i) is the probability that a pixel has a vector [X] and is in class i. If this last term is divided by p([X]) with $p([X]) = \sum p([X]|i)\, p(i)$, then it yields the a posteriori probability p(i|[X]). Therefore, the a posteriori probability is defined by the expression[1]:

$$P(i|[X]) = \frac{P([X]|i)\,P(i)}{P(X)}$$

This is the new probability that the pixel belongs to each of the training classes, given that it has a vector [X]. The Bayes decision rule can now be stated as[1]:

*A pixel belongs to class i if* $\forall j, j \neq i, p(i|[X]) > p(j|[X])$

Since p([X]) is constant for all the classes, the decision rule becomes:

*A pixel belongs to class i if* $\forall j, j \neq i, p([x]/i)\, p(i) > p([x]/j)\, p(j)$

Maximizing p([x]|i) p(i) is equivalent to maximizing $D_i([x])$ defined by[1]:

$$D_i([x]) = \frac{P(i)}{|\Sigma_i|^{1/2}(2\pi)^{3/2}} exp\{-\frac{1}{2}(([x]-[\mu_i])^T \Sigma_i^{-1}([x]-[\mu_i]))\}$$

At this point, it can be shown that the minimum distance classification is a simplified case of the maximum likelihood classification. In the minimum distance classification, the a priori probabilities are taken equal, the covariance matrices are also taken equal, and moreover the off diagonal terms are assumed to be zero. Thus, the following quantity is a constant for all classes i:

$$\frac{P(i)}{|\Sigma_i|^{1/2}(2\pi)^{3/2}} = constant$$

Maximizing $D_i([X])$ is then equivalent to minimizing $([X] - [\mu_i])^T \Sigma_0^{-1} ([X] - [\mu_i])$ with:

$$\Sigma_0 = \begin{bmatrix} \sigma_1^2 & 0 & 0 \\ 0 & \sigma_2^2 & 0 \\ 0 & 0 & \sigma_3^2 \end{bmatrix}$$

If the previous expression is developed, it yields what was used in the minimum distance classification:

$$([x]-[\mu_i])^T \Sigma_0^{-1} ([x]-[\mu_i]) = \left(\frac{x_1-\mu_1}{\sigma_1}\right)^2 + \left(\frac{x_2-\mu_2}{\sigma_2}\right)^2 + \left(\frac{x_3-\mu_3}{\sigma_3}\right)^2$$

The maximum likelihood principle is now implemented on the System 600, using the same training sets previously defined in the minimum distance classification. First the a priori probabilities are taken as equal. The only parameter to set is the desired confidence

level. The available confidence levels are 10, 25, 50, 75, 90, and 95%[4]. As an example, a confidence level of 90% means that 90% of the pixels classified as scar have the spectral signature of an actual scar. The remaining 10% classified as scar do not have the spectral signature of a scar, although they have been assigned to this class. For the various values of the available confidence levels, the results are shown in Table 8.12.

The populations of the training sets "scar" and "vegetation" also greatly vary depending upon the confidence level. The population distribution of the class "scar", like the minimum distance classification, tends to concentrate on the coast and in cloud shadows when the confidence level is decreased (50% and lower). Thus, after visualization, the best estimated population for the class "scar" is 287 pixels (confidence 75%). This confidence level discards most of the coastal pixels without affecting the inland pixels (Image 8.9). Nevertheless, most of the pixels are still concentrated in the western part like for the minimum distance classification.

Estimations of the a priori probabilities are provided in a second step. The a priori probability that a pixel belongs to the class "scar" is equal to the ratio of the total burned area in Spain and Portugal (222 081 ha, Table 4.3) to the land area of Spain and Portugal (59 271 000 ha, Table 3.4). It comes out to 0.00375. The a priori probability that a pixel belongs the class "vegetation" is equal to the ratio of the total forested area in Spain and Portugal (15 164 000 ha, Table 3.4) to the total land area of Spain and Portugal. It comes out to 0.26. When using these two a priori probabilities, the maximum likelihood classification yields another set of results, summarized in Table 8.13.

For a confidence level greater than 50%, the population estimations are identical to those produced with equal a priori probabilities. The best confidence level is once more 75% and the output classified map is the same (Image 8.9).

The unsupervised classification relies on a completely different approach[1]. It is also available on the System 600. First, the computer determines classes by locating naturally occurring concentrations of vectors, based on their values, which are then gathered into clusters. These clusters generate statistics and the classification of the whole image can be implemented. The System 600 only uses the minimum distance principle for the unsupervised classification. The classification process is iterative. The first step of this iteration consists of the generation of an initial mean vector (seed) for each class. Each pixel is then assigned the class of which the seed is the closest to its vector. Using these first boundaries, new class statistics are calculated and a new mean value is generated. The pixels are reassigned the new classes. This procedure goes on until the difference between the two consecutive mean values of all classes is too small to affect the distribution (threshold sensitivity). The parameter for this classification is the total number of classes desired in order to classify the whole image. The number of pixels classified as scars in terms of the number of classes is summarized in Table 8.14.

The importance of the population "scar" is given as a percentage with only three decimals of the total number of pixels in the image (1500×1000). Thus, it is not possible to differentiate the results in terms of the exact number of pixels per class, even though this number varies. Only the spatial distribution and the pixel size of the known scar in Portugal will enable the user to choose the best unsupervised classification. The class number differs because classes are deleted while others are added, in order to come up eventually with the original total number of classes. The original pixel number of the reference scar in Portugal is 59. The two unsupervised classification that yield the closest size estimation are when 141 and 142 seeds are originally selected. In the first case, 72 pixels show up in the class #40 at the very same location of the reference scar. This is too many! In consequence, too many pixels are attributed to this class in the whole scene. Most of them appear on the coast or in cloud shadows. The population of the class "scar" is overes-

timated. In the second case, only 29 pixels show up in the class #52 at the location of the known scar. That is less than the original 59 pixels. The population for the whole image will therefore be underestimated (Image 8.10). It is not possible to get an intermediate estimation of the pixel size of the reference scar. Therefore, the unsupervised classification does not provide a good estimation spatially and quantitatively of the burned areas because of the impossibility of getting a close size estimation for reference scars.

Classification of the burned areas on a regional scale does not turn out to be very effective whatever the classification process is, i.e., supervised minimum distance and maximum likelihood classification or unsupervised classification. On one hand, areas that are not scars are classified as scars, because they do have similar spectral properties. This shows up best with the unsupervised classification. On the other hand, actual burned areas are not classified as scar because they have different spectral properties from the selected training set. The overlap between known scars resulting from forest fires is not high enough to come up with an exhaustive classification. This shows up best with the supervised classification. Moreover, excellent imagery is required in order to minimize the classification error. Cloudless scenes without haze and without different ecosystems are best. Finally, several scars per ecosystem are needed in order to build a reliable training set. To eliminate all these problems, the classification process will be implemented on a local scale in the next chapter.

TABLE 8.1

STATISTICS OF THE TRAINING SET "SCAR" IN THE 88085 SCENE

| Channel | 1 | 2 | 4 |
|---|---|---|---|
| Average | 69 | 94.5 | 295.6 |
| Standard deviation | 9 | 13 | 2.1 |

TABLE 8.2

STATISTICS OF THE TRAINING SET "VEGETATION" IN THE 88085 SCENE

| Channel | 1 | 2 | 4 |
|---|---|---|---|
| Average | 52.4 | 109.8 | 294.7 |
| Standard deviation | 5.9 | 10.0 | 1.9 |

TABLE 8.3

CORRELATION OF THE TRAINING SETS "SCAR" IN THE SCENES

88085, 88101, AND 87107

| Scene | $\lvert\rho_{12}\rvert$ | $\lvert\rho_{14}\rvert$ | $\lvert\rho_{24}\rvert$ |
|---|---|---|---|
| 88085 | 0.59 | 0.62 | 0.51 |
| 88101 | 0.56 | 0.74 | 0.72 |
| 87107 | 0.27 | 0.76 | 0.04 |

TABLE 8.4

CORRELATION OF THE TRAINING SETS "VEGETATION" IN THE SCENES 88085, 88101, AND 87107

| Scene | $\lvert\rho_{12}\rvert$ | $\lvert\rho_{14}\rvert$ | $\lvert\rho_{24}\rvert$ |
|---|---|---|---|
| 88085 | 0.61 | 0.28 | 0.23 |
| 88101 | 0.79 | 0.47 | 0.47 |
| 87107 | 0.89 | 0.86 | 0.76 |

TABLE 8.5

STATISTICS OF THE TRAINING SET "SCAR" IN THE 87128 SCENE

| Channel | 1 | 2 | 4 |
|---|---|---|---|
| Average | 49.3 | 123.8 | 298.8 |
| Standard deviation | 3.5 | 11.4 | 1.3 |

TABLE 8.6

STATISTICS OF THE TRAINING SET "VEGETATION" IN THE 87128 SCENE

| Channel | 1 | 2 | 4 |
|---|---|---|---|
| Average | 55.4 | 116.2 | 300.2 |
| Standard deviation | 7 | 11.3 | 1.7 |

TABLE 8.7

OVERLAP, IN CHANNELS 1, 2, AND 4, OF THE "VEGETATION" TRAINING SETS BETWEEN THE 87128 AND 88085 SCENES

| Channels | 87128 scene | 88085 scene | Overlap (%) |
|---|---|---|---|
| 1 | 55.4 (7) | 52.3 (6) | 80 |
| 2 | 116.1 (11) | 109.8 (10) | 76.3 |
| 4 | 300.2 (1.7) | 294.6 (1.9) | 11.2 |

TABLE 8.8

OVERLAP, IN CHANNELS 1, 2, AND 4, OF THE "SCAR" TRAINING SETS BETWEEN THE 88101 AND 88085 SCENES

| Channels | 88085 scene | 88101 scene | Overlap (%) |
|---|---|---|---|
| 1 | 69 (9) | 64 (5) | 60.3 |
| 2 | 94.5 (13) | 85.5 (9.7) | 70.5 |
| 4 | 295.6 (2.1) | 293 (1.5) | 39.8 |

TABLE 8.9

OVERLAP, IN CHANNELS 1, 2, AND 4, OF THE "SCAR" TRAINING SETS BETWEEN THE 87107 AND 88085 SCENES

| Channels | 88085 scene | 87107 scene | Overlap (%) |
|---|---|---|---|
| 1 | 69 (9) | 81.5 (3.5) | 26.7 |
| 2 | 94.5 (13) | 99 (5.5) | 57.9 |
| 4 | 295.6 (2.1) | 295.5 (1) | 64.9 |

TABLE 8.10

TRANSFORMED DIVERGENCE FOR THE TRAINING SETS "SCAR" AND "VEGETATION" IN THE 87128 AND 88085 SCENES

| Combination | 87128 scene | 88085 scene |
|---|---|---|
| 123 | 78.65 | 90.34 |
| 12 | 74.31 | 90.23 |
| 13 | 42.96 | 55.71 |
| 23 | 35.18 | 32.98 |

TABLE 8.11

POPULATION OF THE CLASSES "SCAR" AND "VEGETATION" MINIMUM DISTANCE CLASSIFICATION

| Threshold ($\times\sigma$) | population "scar" (pixels) | population "vegetation" (pixels) |
|---|---|---|
| 1.0 | 375 | 1943 |
| 1.1 | 531 | 2531 |
| 1.2 | 700 | 3130 |
| 1.3 | 930 | 3885 |
| 1.5 | 1483 | 5656 |
| 2.0 | 3607 | 11196 |

TABLE 8.12

POPULATION OF THE CLASSES "SCAR" AND "VEGETATION", MAXIMUM LIKELIHOOD CLASSIFICATION, EQUAL A PRIORI PROBABILITIES

| Confidence (%) | Population "scar" (pixels) | Population "vegetation" (pixels) |
|---|---|---|
| 10 | 3810 | 19053 |
| 25 | 2094 | 11073 |
| 50 | 886 | 5475 |
| 75 | 287 | 2032 |
| 90 | 81 | 617 |
| 95 | 47 | 247 |

TABLE 8.13

POPULATION OF THE CLASSES "SCAR" AND "VEGETATION", MAXIMUM LIKELIHOOD CLASSIFICATION, NON EQUAL A PRIORI PROBABILITIES

| Confidence (%) | Population "scar" (pixels) | Population "vegetation" (pixels) |
|---|---|---|
| 10 | 2470 | 19154 |
| 25 | 1498 | 11073 |
| 50 | 792 | 5475 |
| 75 | 287 | 2032 |
| 90 | 81 | 617 |
| 95 | 47 | 247 |

TABLE 8.14

POPULATION OF THE CLASSES "SCAR"

UNSUPERVISED CLASSIFICATION

| # classes | Population "scar" (%) | class # | # pixels of the known scar |
|---|---|---|---|
| 120 | 0.010 | 28 | N/A |
| 130 | 0.006 | 32 | N/A |
| 138 | 0.001 | 49 | 19 |
| 139 | 0.002 | 51 | 23 |
| 140 | 0.001 | 52 | 15 |
| 141 | 0.005 | 40 | 72 |
| 142 | 0.001 | 52 | 29 |
| 143 | 0.001 | 47 | 25 |
| 144 | 0.001 | 55 | 15 |
| 150 | 0.016 | 60 | N/A |

FIGURE 8.1

OVERLAP OF TWO NORMAL DISTRIBUTIONS

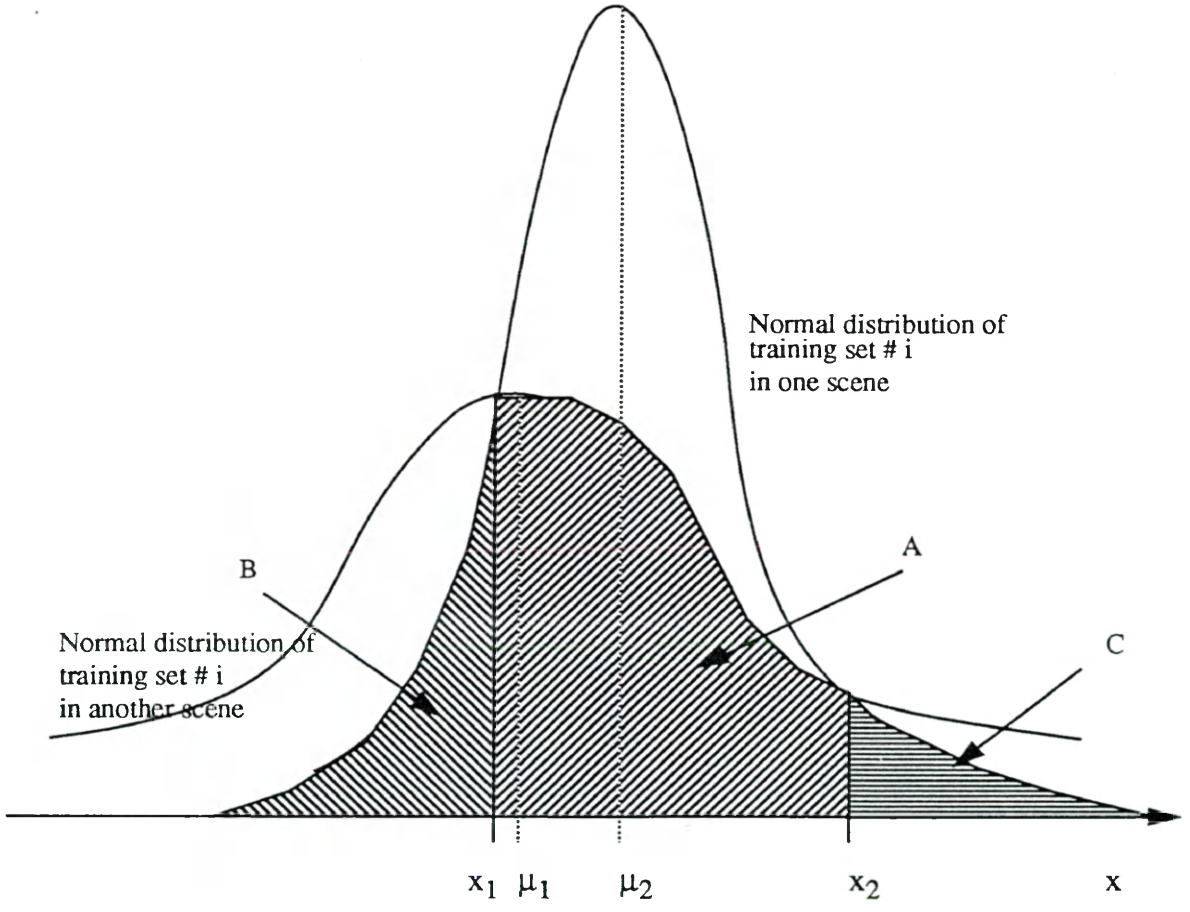

IMAGE 8.1

LAC IMAGE, MAY 8, 1987, CHANNELS 1, 2, AND 4, COLOR TABLE

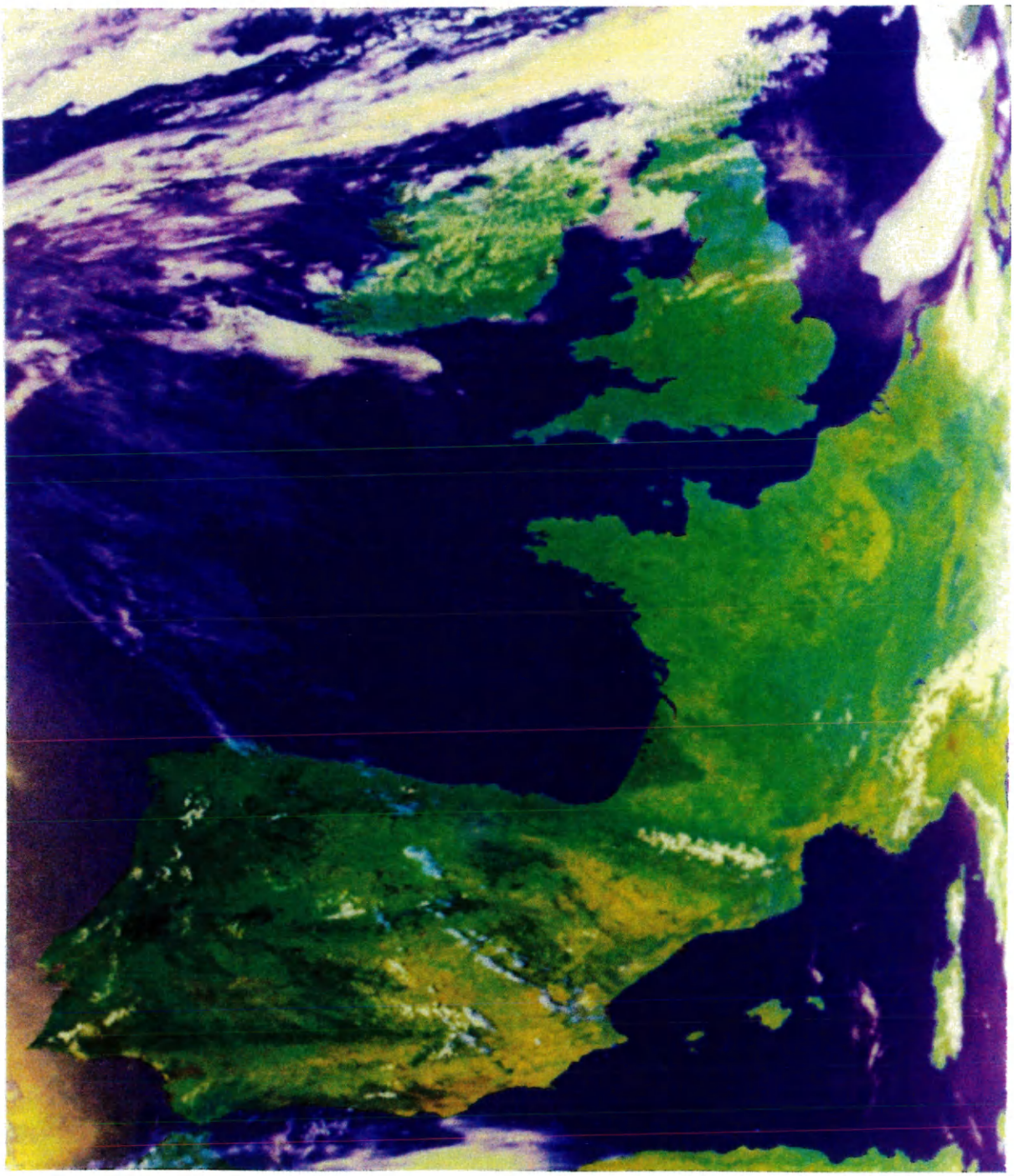

IMAGE 8.2

LAC IMAGE, MARCH 25, 1988, CHANNELS 1, 2, AND 4, COLOR TABLE

IMAGE 8.3

MAPPED LAC IMAGE, MAY 8, 1987, CHANNELS 1, 2, AND 4, (87128 SCENE),

COLOR TABLE

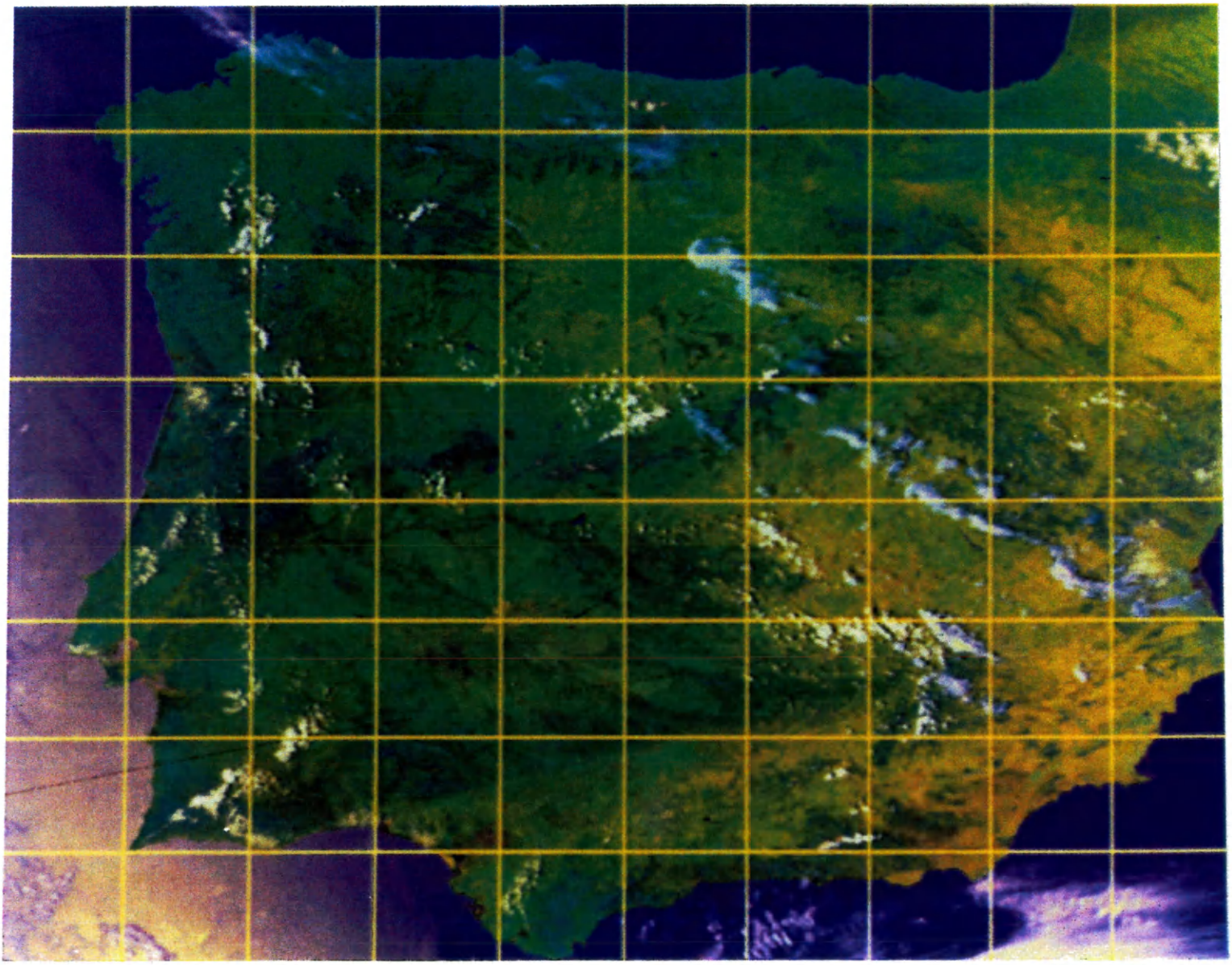

IMAGE 8.4

MAPPED LAC IMAGE, MARCH 25, 1988, CHANNELS 1, 2, AND 4, (88085 SCENE), COLOR TABLE

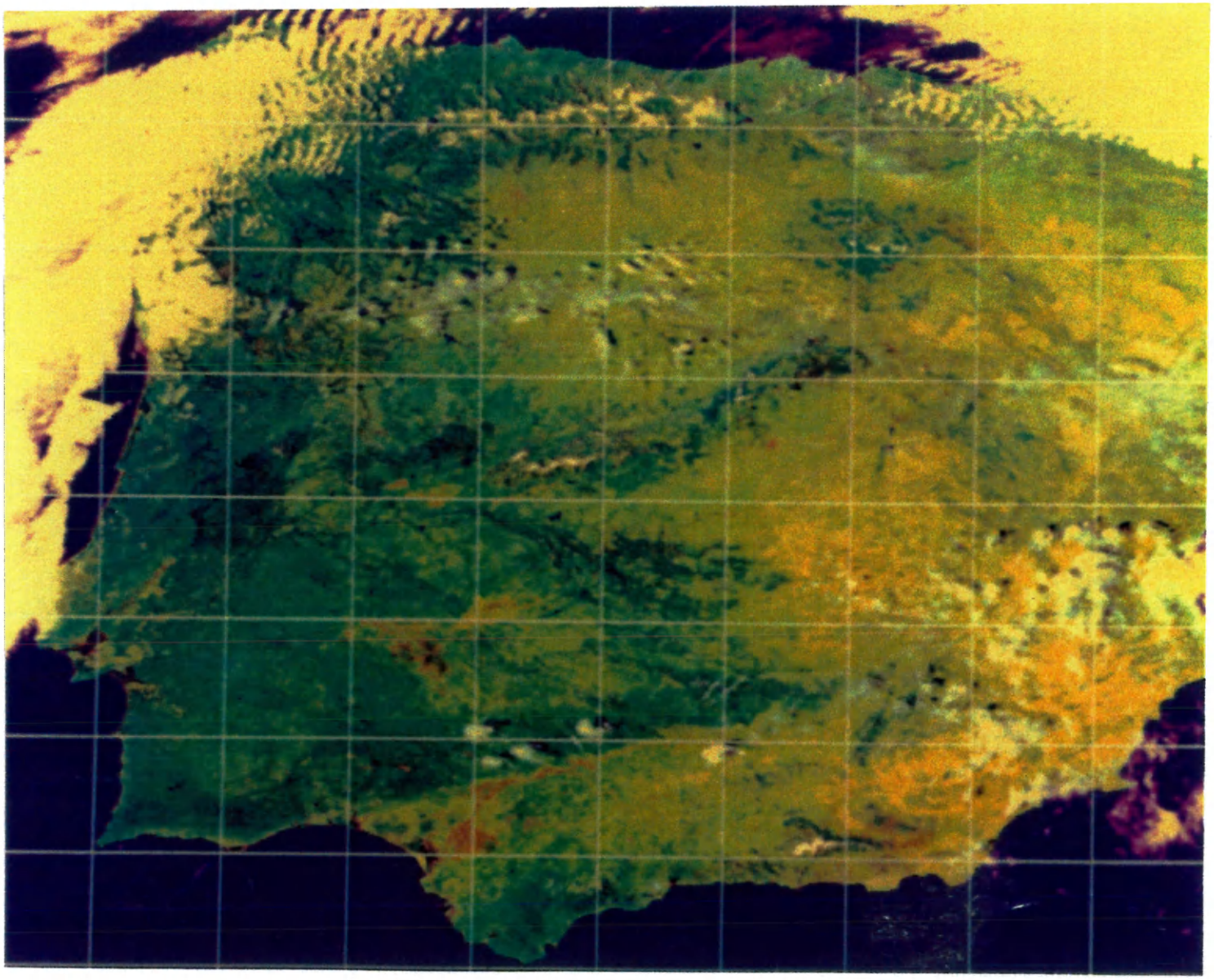

IMAGE 8.5

[40°N->41°N, 7°E->8°E], FALSE COLOR, 87128 SCENE / 88085 SCENE

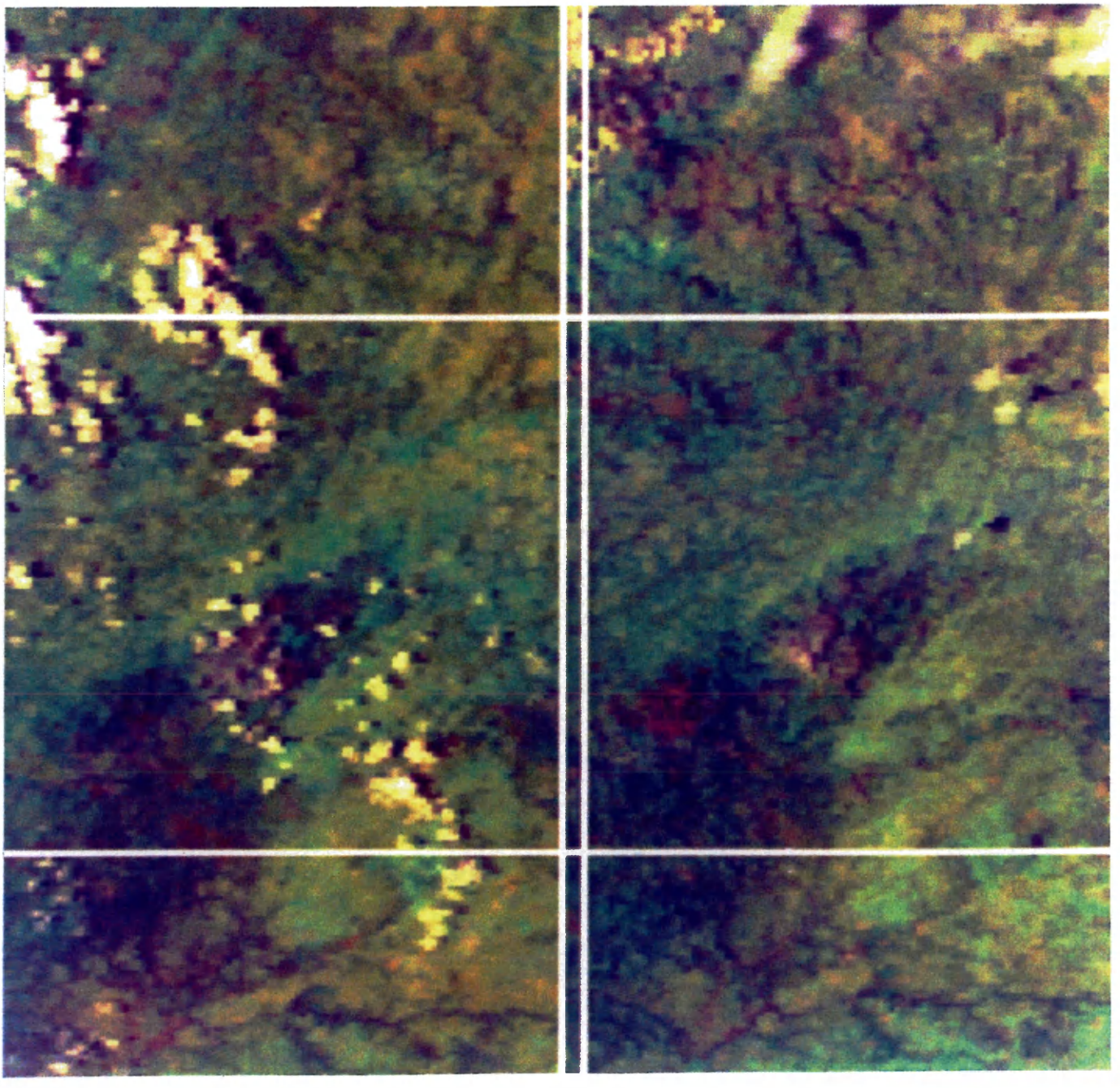

IMAGE 8.6

[40°N->41°N, 7°E->8°E], NDVI, 87128 SCENE /88085 SCENE

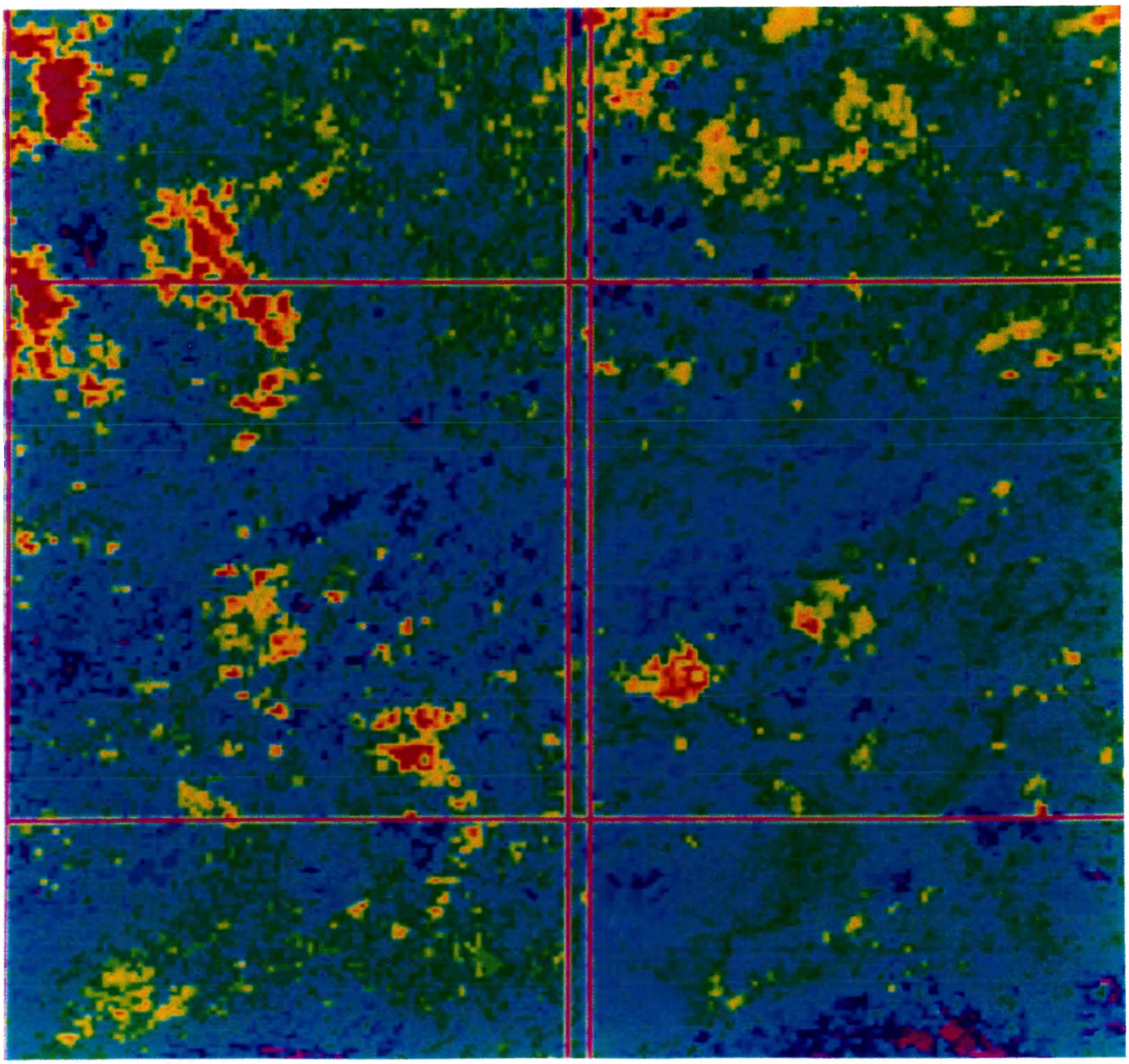

IMAGE 8.7

CONTOURS OF THE TRAINING SETS "SCAR" AND "VEGETATION"

IN THE 88085 SCENE

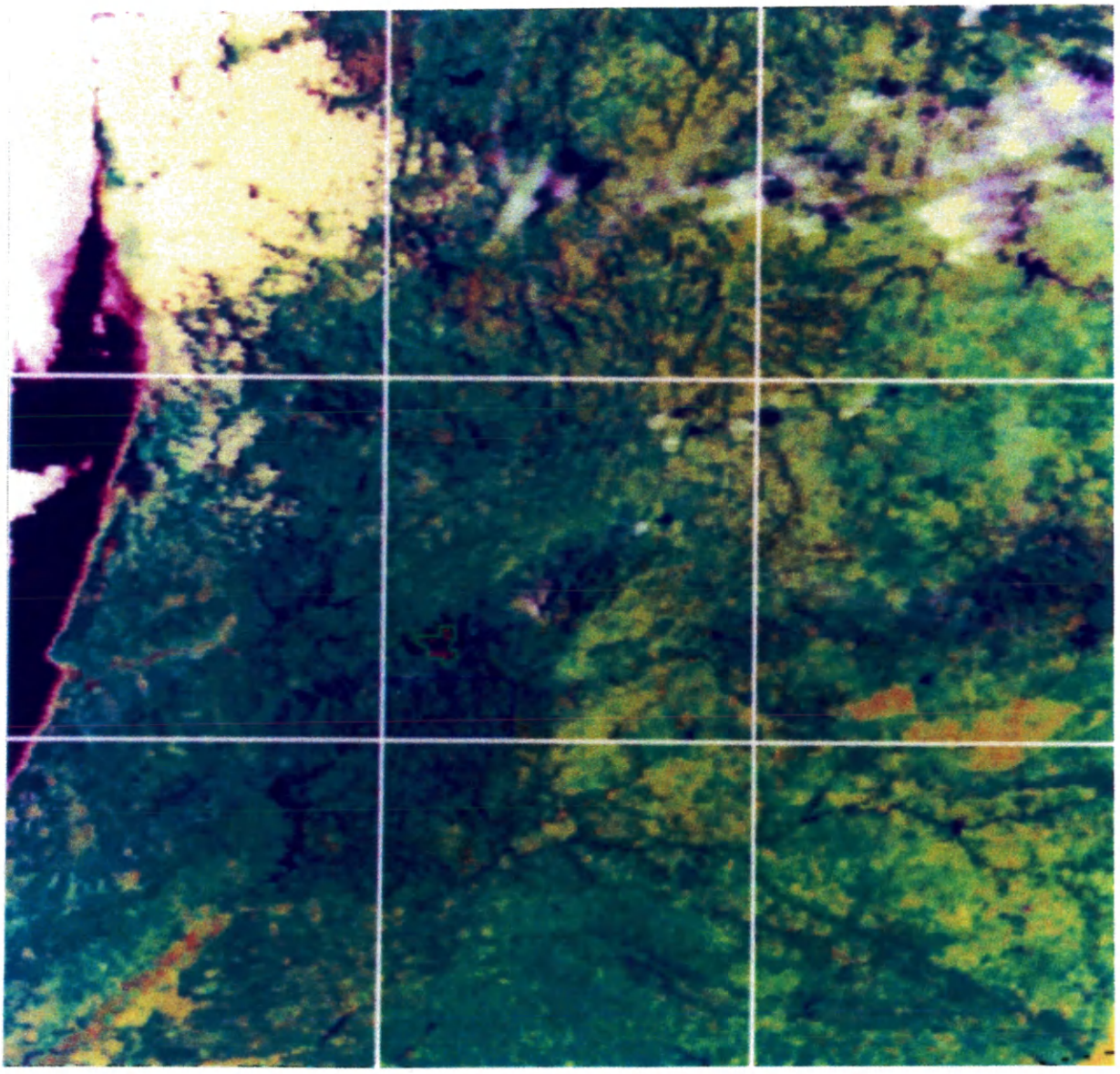

IMAGE 8.8

CLASS "SCAR", 88085 SCENE, MD CLASSIFICATION, CHANNELS 1, 2, AND 4

THRESHOLD = 1.0×σ

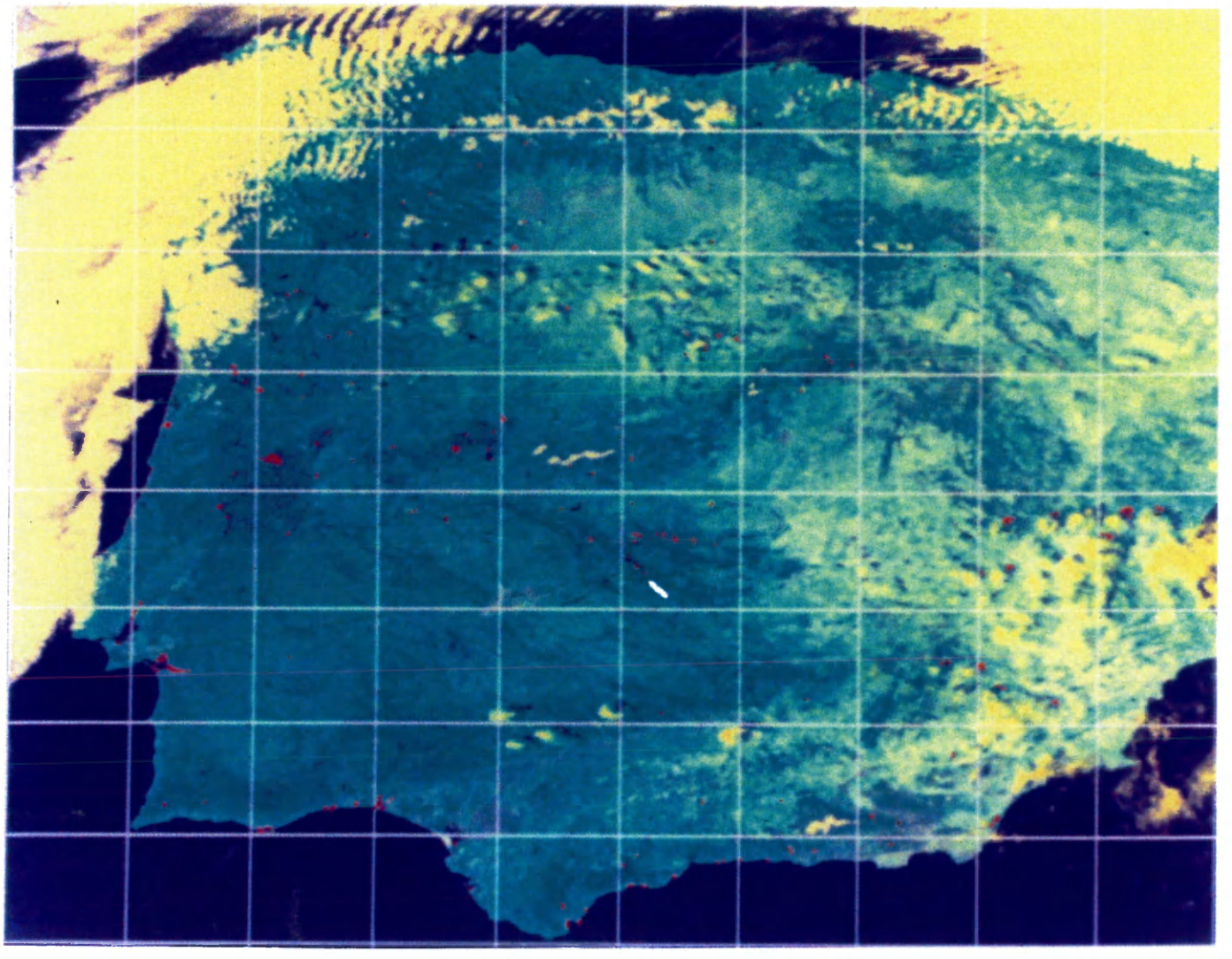

IMAGE 8.9

CLASS "SCAR", 88085 SCENE, ML CLASSIFICATION, CHANNELS 1, 2, AND 4

CONFIDENCE LEVEL = 75%

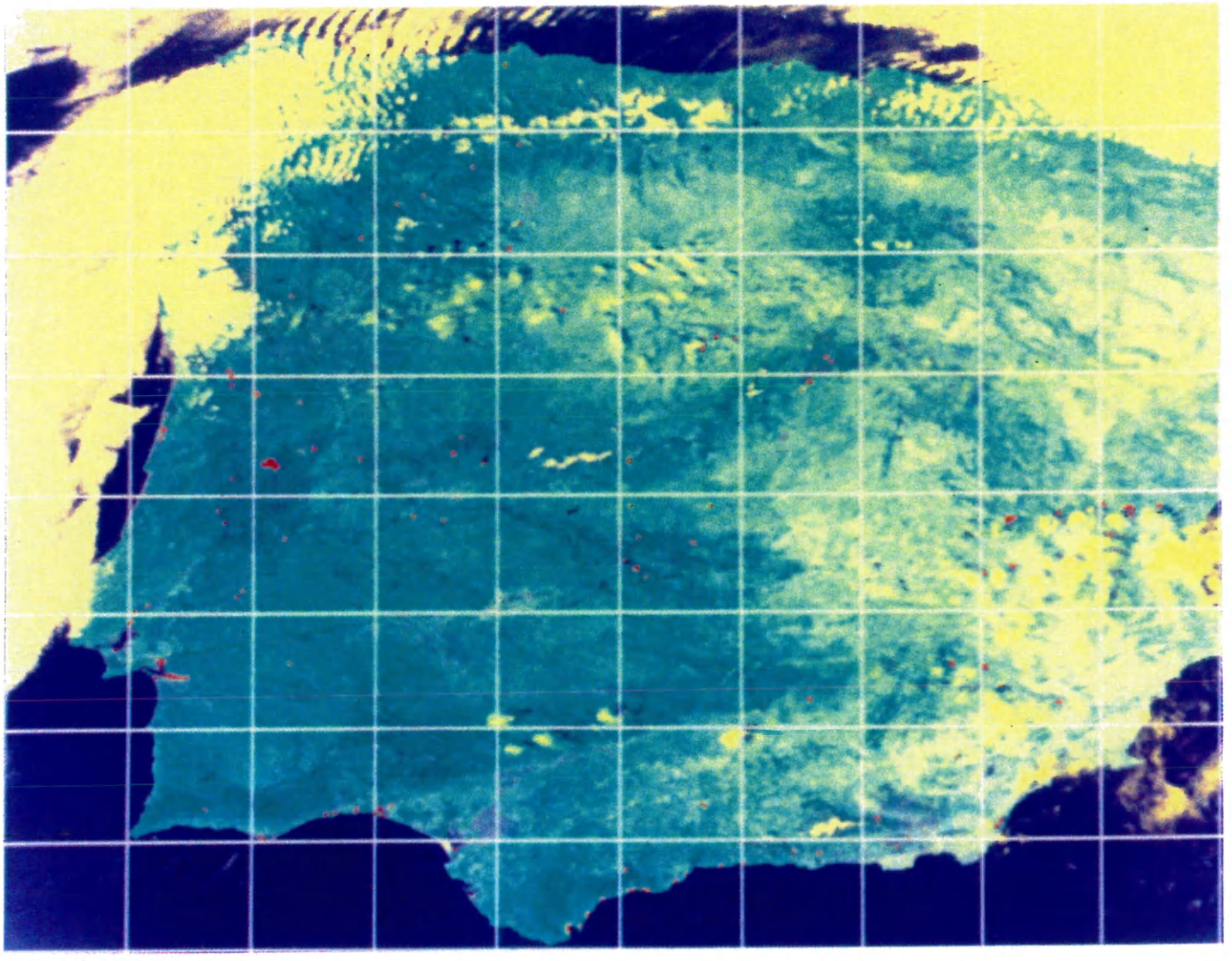

IMAGE 8.10

CLASS "SCAR", 88085 SCENE, UNSUPERVISED CLASSIFICATION, 142 SEEDS

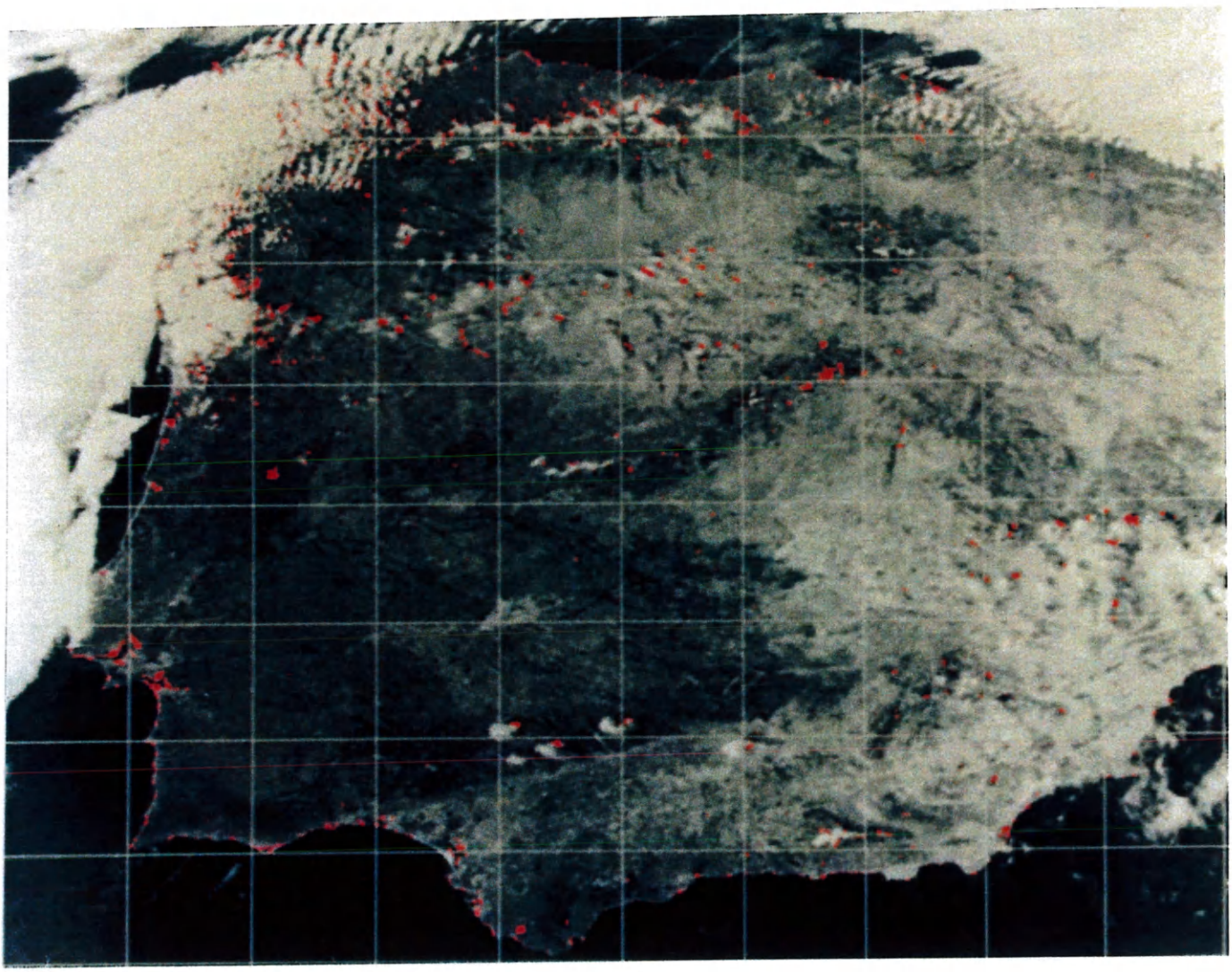

# NOTES TO CHAPTER VIII

1. Schowengerdt, R. A. Techniques for Image Processing and Classification in Remote Sensing. Academic Press, Inc., 1983.

2. IVAS General Module User's Guide. International Imaging Systems, 1991.

3. Mc Clave, J. T., Dietrich, II, F. H. Statistics. 2nd Edition, Dellen Publishing Company, Santa Clara, 1982.

4. System 600 Version 4.0 Command Reference CPU II (L-Z) Volume III. International Imaging Systems, 1990.

# CHAPTER IX

# LOCAL CLASSIFICATION OF BURN SCARS

Classification of burn scars can be implemented either on a regional scale (Chapter VIII) or on a local scale. The regional classification of scars was not successful because of the lack of training sets characteristic of scars in different ecosystems. Moreover, coastal pixels or cloud shadows would appear in the class "scar" because of similar spectral properties. The local classification of scars using the LAC imagery is now investigated in order to find out whether the classification of small areas like scars with this data would still be possible in western Europe.

In order to carry out this study, a small test area was selected in the southern part of France due to the availability of information relative to forests fires in this region. Three departments (Bouches du Rhône (13), Var (83), and Alpes-Maritimes (06)), on the mediterranean coast, have been picked up because large fires have already been located in this area for the years 1987 and 1986 (Chapter VII). Moreover, the locations and sizes of all the fires larger than 100 ha are known for these three departments. The data has been obtained for both years from the database called PROMETHEE archived by the Centre National du Machinisme Agricole, du Genie Rural, des Eaux et des Forets (CEMAGREF) in Aix en Provence, France. Scars, smaller than 100 ha, are not likely to be sensed by the NOAA-AVHRR detector because its resolution is about 100 ha at nadir (Chapter VI). The selected region fits in a $4^{o}\times1^{o}$ area, starting at $4^{o}$E $43^{o}$N and ending at $8^{o}$E $44^{o}$N. This region has been cropped in the 87107 mapped scene (Image 7.8) in order to find out the fires that happened in the year 1986. It has also been cropped in the 88101 mapped scene

(Image 7.9) to spatially locate the fires that occurred in 1987. The two resulting images are displayed respectively in Images 9.1 and 9.2.

First, the 1988 image (Image 9.2) is classified in terms of burned vegetation in order to find out the scars resulting from fires that occurred in 1987. In 1987, there were only six fires of which the extent was greater than 100 ha. They are listed in Table 9.1, with their respective size. Their approximative location appears on Image 9.3. The largest fire (Fréjus) is taken as the training set characteristic of burned vegetation because it is the only one that, due to its size, shows up well on the imagery. This scar is the same as that studied in Chapter VII. Therefore, its statistics for channels 1, 2, and 4 are the same as those displayed in Table 7.3.

Like for the regional classification, both the minimum distance and maximum likelihood classification are implemented. Table 9.2 shows the number of pixels classified as scars depending upon the threshold value used in the minimum distance classification with channels 1, 2, and 4. Since the average ground surface represented by a pixel in the $4^{o}\times1^{o}$ rectangle is about 88 ha (Chapter VII), then the total size of the classified burned area can be estimated, for each threshold, because the total number of pixels is known. The estimation is also displayed in Table 9.2. Since the actual total area burned in 1987 is 4269 ha (Table 9.1, this chapter), the best size estimation produced by the minimum distance classification would be obtained with a threshold of $1.45\times\sigma$ (4312 ha versus 4269 ha). However, the spatial distribution (Image 9.4) of the areas classified as scars does not match very well with that of the actual fires (Image 9.3). Out of the six known fires (Table 9.1, this chapter), only two show up after implementing the minimum distance classification with three channels. They are those that occurred in Le Rous and Fréjus. Although the four other large fires do not show up in Image 9.4, other areas are classified as scars. This means that areas that are not scars, nevertheless, have the spectral signature of a scar. At

this point, precision coefficients have to be determined to assess the actual accuracy of the classification. They are:

(1) - The size precision ($P_{size}$), which relates the total area classified as scar ($A_{classified}$) with the actual total scar area ($A_{scar}$). If $A_{classified} < A_{scar}$, then:

$$P_{size} = \frac{A_{classified}}{A_{scar}}$$

otherwise:

$$P_{size} = \frac{A_{scar}}{A_{classified}}$$

(2) - The classification precision ($P_{classification}$), which relates the total area of actual scars that are classified as such ($A_{classified\_scars}$) to the total area of the class "scar" ($A_{classified}$).

$$P_{classification} = \frac{A_{classified\_scars}}{A_{classified}}$$

$$A_{classified\_scars} = \sum_{fires} MIN(area\_classified, actual\_area)$$

(3) - the global classification precision ($P_{global}$), which evaluates the global accuracy of the classification.

$$P_{global} = P_{size} P_{classification}$$

For the threshold of 1.45×σ, the following figures (Table 9.3) are obtained: $A_{classified}$ = 4312 ha, $A_{scar}$ = 4269 ha, and $A_{classified\_scars}$ = 2220 ha. Therefore, the size preci-

sion is 99% and the classification precision is 51%. Finally, the global classification precision comes out to about 50.5%. This is relatively low and thus prevents from any reliable classification. This confirms that spectral signatures of scars differ, even on a local scale and within the same ecosystem.

Since the minimum distance classification does not come up with satisfying results, the maximum likelihood principle is now implemented. The training sets used are always the same. The number of pixels classified as scars depending upon the confidence level is shown in Table 9.4. The closest total size estimation is given by a confidence level of 25%. The spatial distribution corresponding to this confidence level is shown in Image 9.5. Since the total area is slightly overestimated (5544 ha versus 4269 ha), the size precision is 77%. It is not possible to get a higher precision because there is no confidence level available in the range [25%, 50%]. All the known fires listed in Table 9.1 do not show up. Only the same two scars that appeared resulting the minimum distance classification show up with the minimum likelihood classification. Therefore, the latter does not result in a better spatial distribution of scars on a local scale with the LAC imagery.

So far, the classification of the burned areas has been done with channels 1, 2, and 4 (Chapter VII). It has been a classification in a three dimensional space. A fourth dimension, that emphasizes the differences between burned and non burned vegetation can be added. This dimension is materialized by the NDVI image of the corresponding scene. The same contours for the training sets "scar" and "vegetation" as those in the three dimensional classification are used. The statistics for the channels 1, 2, and 4 are therefore identical to those displayed in Table 7.3 for the training set "scar" and in Table 7.4 for the training set "vegetation". To these statistics must be added those corresponding to the NDVI image. They are summarized in Table 9.5.

The new covariance matrices for the training sets "scar" and "vegetation" are 4×4 matrices since there are 4 dimensions. The terms $\sigma_{11}$ , $\sigma_{12}$ , $\sigma_{14}$, $\sigma_{22}$, $\sigma_{24}$, and $\sigma_{44}$ are identical to those produced in chapter VII because the statistics of the two training sets in channels 1, 2, and 4 are the same. The new terms are: $\sigma_{1,ndvi}$, $\sigma_{2,ndvi}$, $\sigma_{4,ndvi}$, and $\sigma_{ndvi,ndvi}$. The covariance matrix for the training set "scar" is:

$$\begin{bmatrix} \sigma_{11} & \sigma_{12} & \sigma_{14} & -5.365 \\ \sigma_{21} & \sigma_{22} & \sigma_{24} & 48.931 \\ \sigma_{41} & \sigma_{42} & \sigma_{44} & 2.962 \\ -5.365 & 48.931 & 2.962 & 48.356 \end{bmatrix}$$

The correlation coefficients $\rho_{12}$, $\rho_{14}$, and $\rho_{24}$ are unchanged. The new correlation coefficients ($\rho_{i,ndvi}$) pertaining to the NDVI band are calculated:

| $\rho_{12}$ | $\rho_{14}$ | $\rho_{24}$ | $\rho_{1,ndvi}$ | $\rho_{2,ndvi}$ | $\rho_{4,ndvi}$ |
|---|---|---|---|---|---|
| 0.56 | 0.74 | 0.72 | -0.15 | 0.72 | 0.27 |

New average correlation coefficients for all the bands have to be calculated. They are:

| $\rho_1$ | $\rho_2$ | $\rho_4$ | $\rho_{ndvi}$ |
|---|---|---|---|
| 0.48 | 0.66 | 0.57 | 0.38 |

For the NDVI band, the average correlation coefficient is 0.38. Therefore, the NDVI band is not highly correlated to channels 1, 2, and 4. That is the reason why it has been added. The covariance matrix for the training set "vegetation" becomes:

$$\begin{bmatrix} \sigma_{11} & \sigma_{12} & \sigma_{14} & -21.887 \\ \sigma_{21} & \sigma_{22} & \sigma_{24} & -9.330 \\ \sigma_{41} & \sigma_{42} & \sigma_{44} & -1.139 \\ -21.887 & -9.330 & -1.139 & 22.128 \end{bmatrix}$$

The correlation coefficients $\rho_{12}$, $\rho_{14}$, and $\rho_{24}$ are unchanged. The new correlation coefficients ($\rho_{i,ndvi}$) pertaining to the NDVI band are calculated:

| $\rho_{12}$ | $\rho_{14}$ | $\rho_{24}$ | $\rho_{1,ndvi}$ | $\rho_{2,ndvi}$ | $\rho_{4,ndvi}$ |
|---|---|---|---|---|---|
| 0.79 | 0.47 | 0.47 | -0.78 | -0.25 | -0.26 |

New average correlation coefficients for all the bands have to be calculated. They are:

| $\rho_1$ | $\rho_2$ | $\rho_4$ | $\rho_{ndvi}$ |
|---|---|---|---|
| 0.68 | 0.50 | 0.40 | 0.43 |

The NDVI band, also for the training set "vegetation", is not highly correlated. It can, therefore, be added and is expected to ameliorate the classification.

The classification of burned and non burned areas is now implemented in a four dimensional space and using the two principles described in Chapter VIII (minimum distance and maximum likelihood). The number of pixels per class and the estimated corresponding burned area are summarized in Table 9.6 for the minimum distance classification and in Table 9.7 for the maximum likelihood classification.

Adding one dimension to the classification results in population differences for both training sets and for both classification principles. For the minimum distance principle, the population of the class "scar" decreases by an average of 41%, over the 11 different thresholds (1.0 to 2.0×$\sigma$, step 0.1), whereas the population of the class "vegetation" decreases by an average of 49%. Adding one dimension results in discarding pixels from the classes at a constant threshold. The classification is more selective. The best total area estimation is now given by the threshold 1.68×$\sigma$ (4312 ha versus 4269 ha) whereas, with only channels 1, 2, and 4, it was given by 1.45×$\sigma$. The size precision is the same (99%). The corresponding spatial distribution is visualized in Image 9.6. It does not match also

very well with that of the actual fires (Image 9.3). Out of the 4312 ha classified as scars ($A_{classified}$), 2396 ha represent actual scars ($A_{classified\_scars}$) (Table 9.8). Then the precision of the classification is 56% and the global classification precision is 55.5%. This is better than without the NDVI dimension (55.5 versus 50.5%). The classification with four dimensions will therefore be preferred when the $4^{o}\times1^{o}$ area in the 87107 scene is studied.

For the maximum likelihood principle, adding one dimension decreases the population of the class "scar" for a confidence level of 10%, 25%, and 90% but increases it for a confidence level of 50% and 75%. On the other hand, it increases the population of the class "vegetation" by an average of about 20%. These results do not agree with those of the minimum distance classification and points out practically the differences between these two principles. The best total area estimation for the class "scar" is given by a confidence level of 25% (4576 ha versus 4269ha) and its corresponding spatial distribution is displayed in Image 9.7. It does not match very well with the distribution of the actual fires (Image 9.3). Thus it is impossible to get a close estimation of the actual total burned area with the maximum likelihood classification. The minimum distance classification will be preferred to the maximum likelihood classification although the latter is, in theory, more reliable because it takes into account the off-diagonal terms of the covariance matrix (Chapter VIII).

The last attempt to classify burned scars in the 1988 scene, before studying the 1987 imagery in order to verify what has been already shown, is the unsupervised classification. If the unsupervised classification is implemented on the $4^{o}\times1^{o}$ area, then the maximum number of classes that the System 600 can differentiate in this particular case, due to its sensitivity, is 138. Though the original number of classes was set to be 200, 62 were deleted by the System 600 because the distance to the other classes was less than the threshold sensibility, parameter to be set when using the unsupervised classification.

The resulting image is displayed in Image 9.10. Too many pixels show up in the class to which belong the known scar of Fréjus, between S$^{t}$ Raphaël and Cannes. The number of classes is not high enough to separate burned from unburned vegetation. This is due to the original determination of classes by locating naturally occurring concentrations of similar vectors in the $4^{o}\times1^{o}$ area (Chapter VIII).

By comparison, if the whole 88101 scene ($40^{o}$N -> $55^{o}$N, $5^{o}$W -> $20^{o}$E) is classified using the unsupervised classification principle into 150 classes, the spatial distribution, in the $4^{o}\times1^{o}$ area (Image 9.8), of the pixels belonging to the class "scar" (class where the scar of Fréjus is found) is different from that of Image 9.10. There are more pixels on the coast and less inland. This difference is due to the different number of classes (150 versus 138) and to the different original sampling of naturally occurring concentrations of vectors. If the same scene (88101) is classified into 250 classes, then the cropped $4^{o}\times1^{o}$ area (Image 9.9) contains less would be scars because the separation between the classes is better. Nevertheless, the population is too high compared with the actual population (Image 9.3). The unsupervised classification does not turn out to be a reliable method to classify small scars because their spectral properties are not similar enough to result in the creation of a class of their own. As far as the classification of small scars on a local scale is concerned, the supervised classification is preferred to the unsupervised classification although the classification precision of the supervised classification is about only 50%. Moreover, the minimum distance classification is preferred to the maximum likelihood because the total burned area can be more easily estimated.

The minimum distance classification of forest fire scars resulted in a maximum classification precision of 56%. Since 1987 was a below average year in terms of fires in southern France, the previous precision level has to be confirmed or infirmed for 1986, which was an above average year in terms of fires.

The same $4^{o}\times1^{o}$area is now cropped in the 87107 scene in order to locate the scars of the fires that occurred in 1986. In 1986, there were 21 fires, of which the extent was greater than 100 ha. Their total surface comes out to 20 628 ha (Table 9.11). Their spatial distribution is displayed in Image 9.11. The fire in the Tanneron forest is taken as the training set characteristic of burned vegetation. Therefore, the statistics for channels 1, 2, and 4 are the same as those in Table 7.5. Only the minimum distance classification on a four dimensional space (channels 1, 2, 4, and NDVI) is presently implemented. This is the classification principle and the space that are likely to show the best results. The statistics of the NDVI image must be added to those of Table 7.1 and 7.2. They are displayed in Table 9.9. The new correlation covariance matrix for the training set "scar" is:

$$\begin{bmatrix} \sigma_{11} & \sigma_{12} & \sigma_{14} & -13.904 \\ \sigma_{21} & \sigma_{22} & \sigma_{24} & 27.941 \\ \sigma_{41} & \sigma_{42} & \sigma_{44} & -2.533 \\ -13.904 & 27.941 & -2.533 & 33.559 \end{bmatrix}$$

The correlation coefficients are:

| $\rho_{12}$ | $\rho_{14}$ | $\rho_{24}$ | $\rho_{1,ndvi}$ | $\rho_{2,ndvi}$ | $\rho_{4,ndvi}$ |
|---|---|---|---|---|---|
| 0.27 | 0.76 | -0.04 | -0.70 | 0.87 | -0.42 |

and the new channel average correlation coefficients are:

| $\rho_1$ | $\rho_2$ | $\rho_4$ | $\rho_{ndvi}$ |
|---|---|---|---|
| 0.58 | 0.39 | 0.41 | 0.66 |

The new correlation covariance matrix for the training set "vegetation" is:

$$\begin{bmatrix} \sigma_{11} & \sigma_{12} & \sigma_{14} & -26.649 \\ \sigma_{21} & \sigma_{22} & \sigma_{24} & -17.438 \\ \sigma_{41} & \sigma_{42} & \sigma_{44} & -4.066 \\ -26.649 & -17.438 & -4.066 & 21.315 \end{bmatrix}$$

The correlation coefficients are:

| $\rho_{12}$ | $\rho_{14}$ | $\rho_{24}$ | $\rho_{1,ndvi}$ | $\rho_{2,ndvi}$ | $\rho_{4,ndvi}$ |
|---|---|---|---|---|---|
| 0.89 | 0.86 | 0.76 | -0.76 | -0.37 | 0.66 |

and the new channel average correlation coefficients are:

| $\rho_1$ | $\rho_2$ | $\rho_4$ | $\rho_{ndvi}$ |
|---|---|---|---|
| 0.84 | 0.67 | 0.76 | 0.60 |

For the training set "scar", the average correlation coefficient for the NDVI dimension is slightly greater than for the other channels. This is due to an exceptionally low correlation between channels 2 and 4 ($\rho_{24}$ = -0.04). On the other hand, for the training set "vegetation", the average correlation coefficient for the NDVI dimension is less than for all the other channels, like for both training sets in the 1988 scene. Thus, it is still assumed that adding one dimension to the classification will improve the accuracy of the class attribution.

When the minimum distance classification is applied to the $4^o \times 1^o$ area, cropped in the 87107 scene, using the previous training set, the classification results, in terms of the threshold (3.5 to 5.0×σ, step 0.1), are displayed in table 9.10. Since the average ground size of a pixel is still 88 ha, the estimation of the classified area can be made for each different threshold (Table 9.10). The best estimation of the total area burned in the $4^o \times 1^o$ area is given by a threshold of 4.26×σ (Image 9.12). Since 232 pixels are classified as scars, the estimated area burned comes out to 20 416 ha ($A_{classified}$), instead of the actual 20 628 ha ($A_{scar}$). Thus the size precision ($P_{size}$) is of 99%. The classification precision ($P_{classification}$) has now to be determined. Among the 232 pixels classified as scars, some represent areas that are not scars, but that have similar spectral properties. The classification precision is given by the ratio of the total classified area that represent actual scars

($A_{classified\_scars}$ = 7697 ha, Table 9.11) to the total area classified as scar ($A_{classified}$ = 20 416 ha). It comes out to 38%. Therefore, the global classification precision is very close to 38%, because the size precision can be estimated to 100%. This global classification precision ($P_{global}$) for the 1987 scene is much less than that estimated for the 1988 scene. The reason is that there have been many more fires in 1986 than in 1987, and more fires result in a wider range of spectral properties relative to scars. Therefore this lowers the classification accuracy.

For each single fire, the corresponding classified areas with a threshold of 4.26×σ are compared to the actual sizes of the fires (Table 9.11). The particular size estimations are not good. They range from 13% for the largest fire up to 440% for the smallest fire. Since the individual size estimations greater than 100% are usually accounted for by small fires, they do not affect too much the average size estimation which is of 69%.

The threshold 4.26×σ was chosen because the total classified area had a size equal to that of the actual fires, which is known data. The global classification precision changes with the value of the threshold. Estimations of the precision classification and size precision have been made in Table 9.13 for the thresholds 3.5×σ, 4.0×σ, 4.5×σ, and 5.0×σ. It turns out that the global precision of the minimum distance classification is maximized by the threshold 4.26×σ, but is nevertheless low (38%).

Classification of scars with the LAC imagery in western Europe, even on a local scale (same ecosystem), does not yield a better global classification precision than 55.5% for the 1988 fire season and 38% for the 1987 fire season. Therefore, the global classification precision depends upon the fire season and turns out to be too low to provide reliable estimations of the spatial distribution and the extent of the fires.

TABLE 9.1

LIST AND EXACT SIZE OF THE FIRES GREATER THAN 100 HA

THAT OCCURRED IN SOUTHERN FRANCE IN 1987

| Name of the Commune | Size (ha) |
|---|---|
| Le Rous (13088) | 196 |
| Aureltie(13006) | 608 |
| Bormes-les-Mimosas(83019) | 920 |
| Le Thoronet(83137) | 110 |
| Sanary-sur-Mer(83123) | 160 |
| Fréjus(83061) | 2275 |
| Total | 4269 |

TABLE 9.2

POPULATION AND ESTIMATED AREA OF THE CLASS "SCAR" AFTER THE MINIMUM DISTANCE CLASSIFICATION, CHANNELS 1, 2, AND 4, 88101 SCENE

| Threshold ($\times\sigma$) | Population "scar" (pixel) | Estimated area (ha) class "scar" | Population "vegetation" (pixel) |
|---|---|---|---|
| 1.0 | 16 | 1408 | 412 |
| 1.1 | 19 | 1672 | 492 |
| 1.2 | 29 | 2552 | 597 |
| 1.3 | 33 | 2904 | 731 |
| 1.4 | 38 | 3344 | 834 |
| 1.45 | 49 | 4312 | 928 |
| 1.5 | 56 | 4928 | 979 |
| 1.6 | 72 | 6336 | 1063 |
| 1.7 | 88 | 7744 | 1220 |
| 1.8 | 111 | 9768 | 1466 |
| 1.9 | 153 | 13464 | 1732 |
| 2.0 | 189 | 16632 | 1983 |

TABLE 9.3

ESTIMATED SIZE OF THE INDIVIDUAL FIRES, MINIMUM DISTANCE CLASSIFICATION, THRESHOLD = 1.45×σ, CHANNELS 1, 2, AND 4, 88101 SCENE

| Commune | Actual size (ha) | Classified size (ha) | MIN(actual,classified) |
|---|---|---|---|
| 13088 | 196 | 880 | 196 |
| 13006 | 608 | 0 | 0 |
| 83019 | 920 | 0 | 0 |
| 83137 | 110 | 0 | 0 |
| 83123 | 160 | 0 | 0 |
| 83061 | 2275 | 2024 | 2024 |
| Total | 4269 | 2904 | 2220 |

TABLE 9.4

POPULATION AND ESTIMATED AREA OF THE CLASS "SCAR", MAXIMUM LIKELIHOOD CLASSIFICATION, CHANNELS 1, 2, AND 4, 88101 SCENE

| Confidence (%) | Population "scar" (pixel) | Estimated area (ha) class "scar" | Population "vegetation" (pixel) |
|---|---|---|---|
| 10 | 107 | 9416 | 2256 |
| 25 | 63 | 5544 | 1376 |
| 50 | 28 | 2464 | 648 |
| 75 | 9 | 792 | 318 |
| 90 | 6 | 528 | 103 |

TABLE 9.5

STATISTICS, IN THE NDVI IMAGE, OF THE TRAINING SETS "SCAR" AND "VEGETATION" IN THE 88101 SCENE

| Statistics | Training set "scar" | Training set "vegetation" |
|---|---|---|
| Mean vector | 172.8 | 205.9 |
| Standard deviation | 6.9 | 4.7 |

TABLE 9.6

POPULATION AND ESTIMATED AREA OF THE CLASS "SCAR", MINIMUM DISTANCE CLASSIFICATION, CHANNELS 1, 2, 4, AND NDVI, 88101 SCENE

| Threshold ($\times\sigma$) | Population "scar" (pixel) | Estimated area (ha) class "scar" | Population "vegetation" (pixel) |
|---|---|---|---|
| 1.0 | 11 | 968 | 186 |
| 1.1 | 15 | 1320 | 271 |
| 1.2 | 17 | 1496 | 301 |
| 1.3 | 20 | 1760 | 337 |
| 1.4 | 22 | 1936 | 412 |
| 1.5 | 31 | 2728 | 467 |
| 1.6 | 40 | 3520 | 577 |
| 1.68 | 49 | 4312 | 612 |
| 1.7 | 51 | 4488 | 633 |
| 1.8 | 61 | 5368 | 753 |
| 1.9 | 72 | 6336 | 932 |
| 2.0 | 90 | 7920 | 1059 |

TABLE 9.7

POPULATION AND ESTIMATED AREA OF THE CLASS "SCAR", MAXIMUM LIKELIHOOD CLASSIFICATION, CHANNELS 1, 2, 4, AND NDVI, 88101 SCENE

| Confidence (%) | Population "scar" (pixel) | Estimated area (ha) class "scar" | Population "vegetation" (pixel) |
|---|---|---|---|
| 10 | 92 | 8096 | 2616 |
| 25 | 52 | 4576 | 1601 |
| 50 | 31 | 2728 | 803 |
| 75 | 15 | 1320 | 353 |
| 90 | 3 | 264 | 139 |

TABLE 9.8

ESTIMATED SIZE OF THE INDIVIDUAL FIRES, MINIMUM DISTANCE CLASSIFICATION, 1.68×σ, CHANNELS 1, 2, 4, AND NDVI, 88101 SCENE

| Commune | Actual size (ha) | Classified size (ha) | MIN(actual,classified) |
|---|---|---|---|
| 13088 | 196 | 968 | 196 |
| 13006 | 608 | 0 | 0 |
| 83019 | 920 | 0 | 0 |
| 83137 | 110 | 0 | 0 |
| 83123 | 160 | 0 | 0 |
| 83061 | 2275 | 2200 | 2200 |
| Total | 4269 | 3168 | 2396 |

TABLE 9.9

STATISTICS IN THE NDVI IMAGE OF THE TRAINING SETS "SCAR" AND "VEGETATION", 87107 SCENE

| Statistics | Training set "scar" | Training set "vegetation" |
|---|---|---|
| Mean vector | 164 | 197.5 |
| Standard deviation | 58 | 4.6 |

TABLE 9.13

GLOBAL CLASSIFICATION PRECISION OF THE MINIMUM DISTANCE CLASSIFICATION, 3.5, 4.0, 4.5, 5.0×σ, CHANNELS 1, 2, 4, NDVI, 87107 SCENE

| Threshold | 3.5×σ | 4.0×σ | 4.26×σ | 4.5×σ | 5.0×σ |
|---|---|---|---|---|---|
| $A_{classified\_scars}$ (ha) | 5056 | 7341 | 7697 | 8087 | 11519 |
| $A_{classified}$ (ha) | 7392 | 13464 | 20416 | 25784 | 48576 |
| $P_{classification}$ (%) | 68 | 55 | 38 | 31 | 24 |
| $P_{size}$ (%) | 36 | 65 | 99 | 80 | 42 |
| $P_{global}$ (%) | 24 | 36 | 38 | 25 | 10 |

TABLE 9.10

POPULATION AND ESTIMATED AREA OF THE CLASS "SCAR", MINIMUM DISTANCE CLASSIFICATION, CHANNELS 1, 2, 4, AND NDVI, 87107 SCENE

| Threshold (×σ) | Population "scar" (pixel) | Estimated area (ha) class "scar" | Population "vegetation" (pixel) |
|---|---|---|---|
| 3.5 | 84 | 7392 | 4677 |
| 3.6 | 94 | 8272 | 4898 |
| 3.7 | 110 | 9680 | 5158 |
| 3.8 | 123 | 10824 | 5370 |
| 3.9 | 137 | 12056 | 5580 |
| 4.0 | 153 | 13464 | 5737 |
| 4.1 | 185 | 16280 | 6011 |
| 4.2 | 207 | 18216 | 6223 |
| 4.26 | 232 | 20416 | 6366 |
| 4.3 | 242 | 21296 | 6416 |
| 4.4 | 269 | 23672 | 6591 |
| 4.5 | 293 | 25784 | 6815 |
| 4.6 | 350 | 30800 | 7057 |
| 4.7 | 403 | 35464 | 7285 |
| 4.8 | 446 | 39248 | 7482 |
| 4.9 | 493 | 43384 | 7663 |
| 5.0 | 552 | 48576 | 7878 |

TABLE 9.11

ESTIMATED SIZE OF THE INDIVIDUAL FIRES, MINIMUM DISTANCE CLASSIFICATION, 4.26×σ, CHANNELS 1, 2, 4, AND NDVI, 87107 SCENE

| Commune | Actual size (ha) | Classified size (ha) | MIN(actual, classified) | Classified / actual (%) |
|---|---|---|---|---|
| 06077 | 126 | 0 | 0 | 0 |
| 06(66+75+43+14) | 4648 | 704 | 704 | 15 |
| 06059 | 1110 | 0 | 0 | 0 |
| 06149 | 360 | 0 | 0 | 0 |
| 06(69+95) | 2380 | 3256 | 2380 | 137 |
| 06079 | 750 | 0 | 0 | 0 |
| 06085 | 110 | 352 | 110 | 320 |
| 06148 | 120 | cloud | N/A | N/A |
| 13009 | 1843 | 0 | 0 | 0 |
| 13025 | 1080 | 0 | 0 | 0 |
| 83091 | 295 | 352 | 295 | 119 |
| 83069 | 4126 | 528 | 528 | 13 |
| 83124 | 120 | 528 | 120 | 440 |
| 83(001+133) | 3420 | 4488 | 3420 | 131 |
| 83134 | 140 | 352 | 140 | 251 |
| Total | 20628 | 10560 | 7697 | 69 |

TABLE 9.12

ESTIMATED SIZE OF THE INDIVIDUAL FIRES, MINIMUM DISTANCE CLASSIFICATION, 3.5, 4.0, 4.5, 5.0×σ, CHANNELS 1, 2, 4, NDVI, 87107 SCENE

| Commune, size (ha) | ac,MIN(cl,ac) 3.5×σ | ac,MIN(cl,ac) 4.0×σ | ac,MIN(cl,ac) 4.5×σ | ac,MIN(cl,ac) 5.0×σ |
|---|---|---|---|---|
| 06077,126 | 0,0 | 0,0 | 352,126 | 352,126 |
| 06(66+75+43+14) | 0,0 | 528,528 | 968,968 | 1848,1848 |
| 06059,1110 | 0,0 | 0,0 | 0,0 | 0,0 |
| 06149,360 | 0,0 | 0,0 | 0,0 | 0,0 |
| 06(69+95),2380 | 1496,1496 | 2200,2200 | 3256,2380 | 3344,2380 |
| 06079,750 | 0,0 | 0,0 | 0,0 | 704,704 |
| 06085,110 | 0,0 | 352,110 | 352,110 | 352,110 |
| 06148,120 | cloud | cloud | cloud | cloud |
| 13009,1843 | 0,0 | 0,0 | 0,0 | 792,792 |
| 13025,1080 | 0,0 | 0,0 | 0,0 | 0,0 |
| 83091,295 | 0,0 | 352,295 | 352,295 | 528,295 |
| 83069,4126 | 0,0 | 528,528 | 528,528 | 1584,1584 |
| 83124,120 | 0,0 | 528,120 | 528,120 | 792,120 |
| 83(001+133),3420 | 3960, 3420 | 4488,3420 | 4664,3420 | 7304,3420 |
| 83134,140 | 352,140 | 352,140 | 352,140 | 352,140 |
| Total | 5808,5056 | 9328,7341 | 11352,8007 | 17952,11519 |

IMAGE 9.1

[4°E->8°E, 43°N->44°N], 87107 SCENE

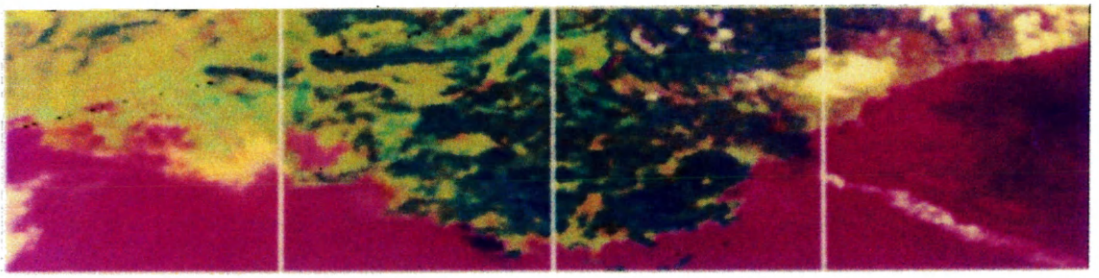

IMAGE 9.2

[4°E->8°E, 43°N->44°N], 88101 SCENE

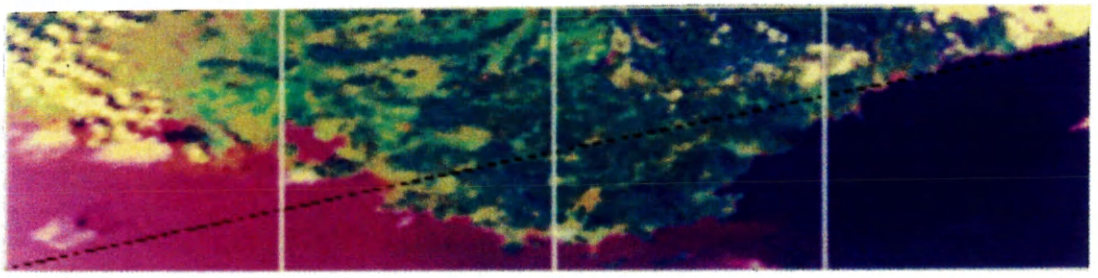

IMAGE 9.3

ACTUAL DISTRIBUTION OF THE FIRES THAT OCCURRED IN 1988

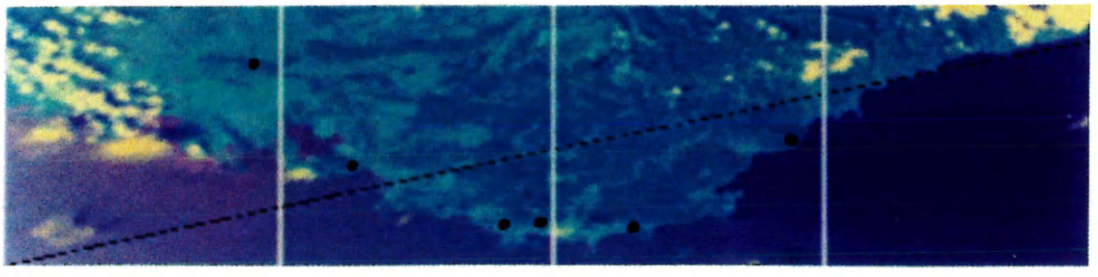

IMAGE 9.4

CLASS "SCAR", IMAGE 9.2, MD CLASS., CHANNELS 1, 2, AND 4, 1.45×σ

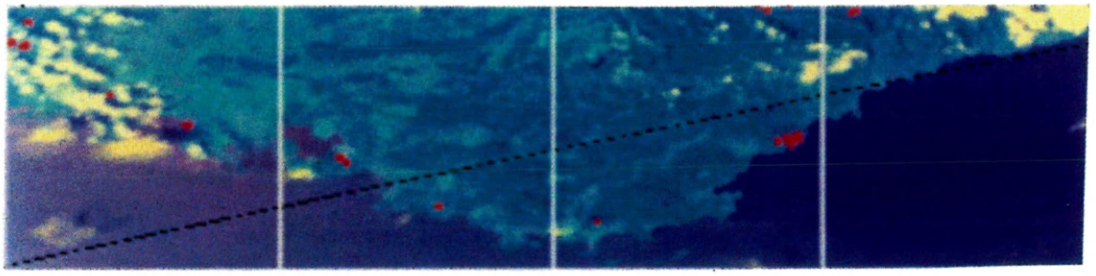

IMAGE 9.5

CLASS "SCAR", IMAGE 9.2. ML CLASS., CHANNELS 1, 2, AND 4, 25%

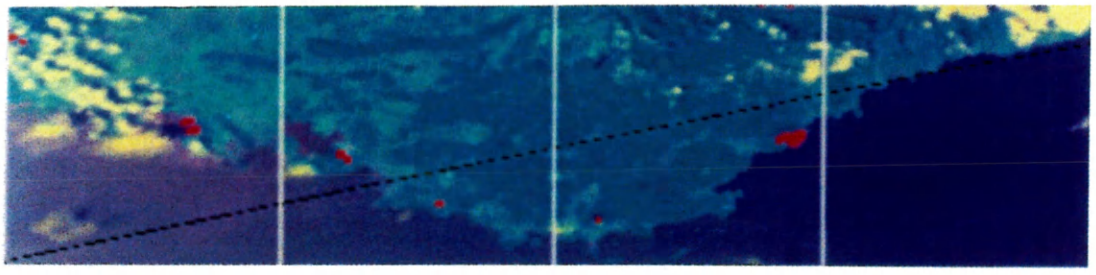

IMAGE 9.6

CLASS "SCAR", IMAGE 9.2, MD CLASS., CHANNELS 1, 2, 4, NDVI, 1.68×σ

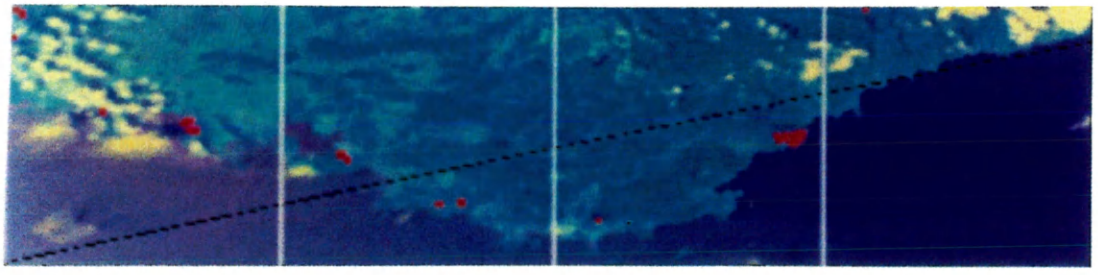

IMAGE 9.7

CLASS "SCAR", IMAGE 9.2, ML CLASS., CHANNELS 1, 2, 4, NDVI, 25%

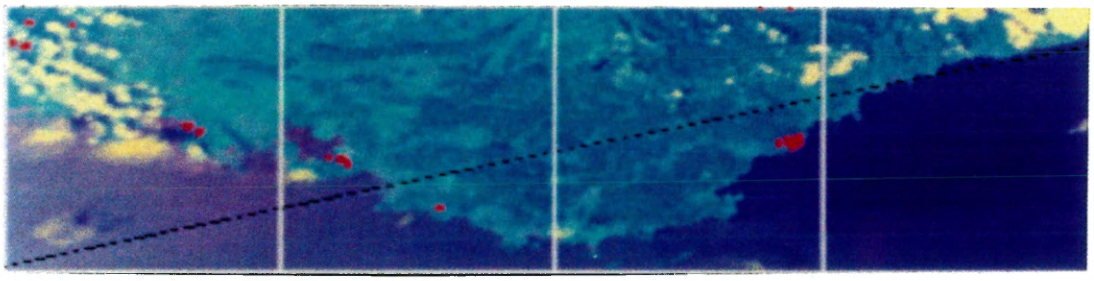

IMAGE 9.8

CLASS "SCAR", IMAGE 7.7, UNSUPERVISED CLASSIFICATION, 150 SEEDS

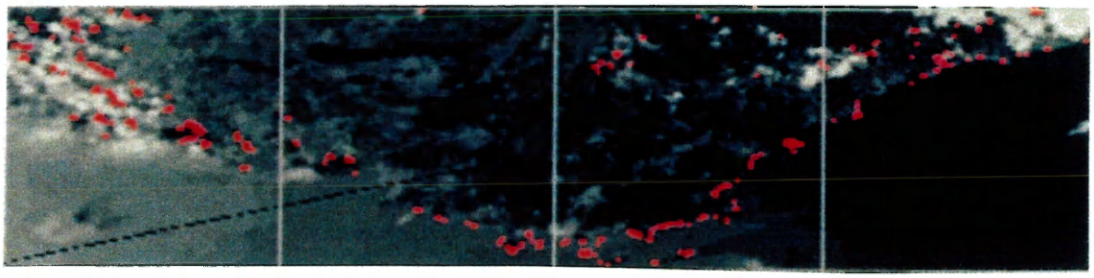

IMAGE 9.9

CLASS "SCAR", IMAGE 7.7, UNSUPERVISED CLASSIFICATION, 250 SEEDS

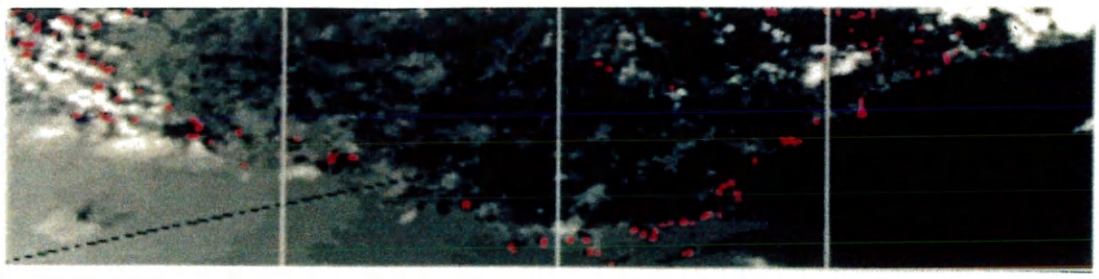

IMAGE 9.10

CLASS "SCAR", IMAGE 9.2, UNSUPERVISED CLASSIFICATION, 138 SEEDS

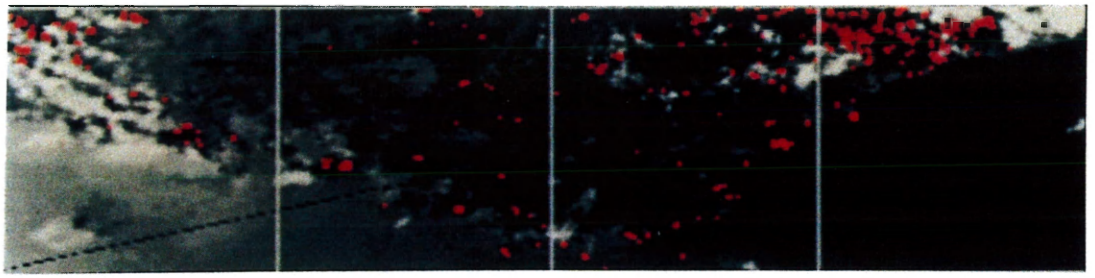

IMAGE 9.11

ACTUAL DISTRIBUTION OF THE FIRES THAT OCCURRED IN 1986

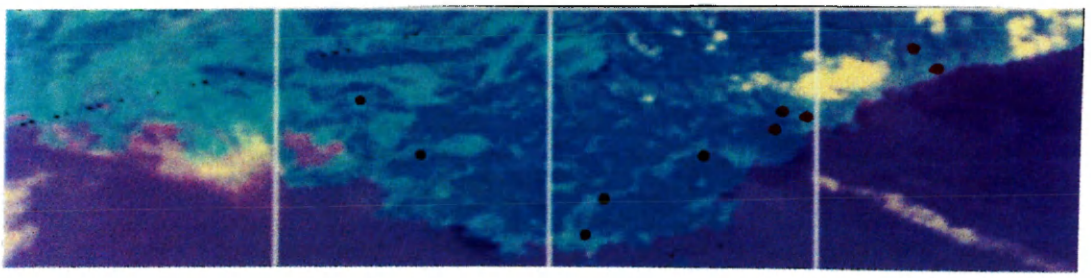

IMAGE 9.12

CLASS "SCAR", IMAGE 9.1, MD CLASS., CHANNELS 1, 2, 4, NDVI, 4.26×σ

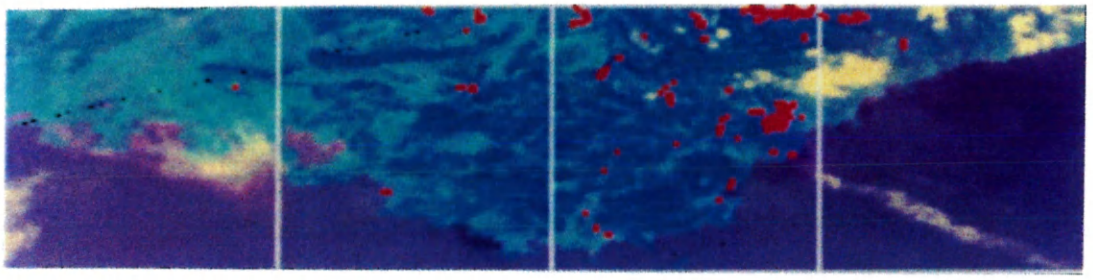

# CONCLUSION

Although biomass burning has increased in the last 150 years on a worldwide scale, it has slightly decreased in western Europe (Chapter I). Planned deforestation, which is the major cause of biomass burning in the tropics, does not take place in western Europe, where the major causes for forests fires are accidental. Prevention is an important aspect of fire control in western Europe whereas in tropical countries, fires are left to burn uncontrolled because there is an economic incentive to permit such burning.

In average, 580 000 ha of forests burn each year in western Europe. 1987 was an under average year in terms of burning in western Europe because only 480 000 ha burned. The trace gases released during and after burning contributed to about 1% of the industrial $CO_2$ emissions in 1987. In 1985, which was a particularly bad year in terms of fires, this figure went up to 3%. The amount of $CO_2$ produced by biomass burning in western Europe in 1987 came out to 0.3% of the total amount produced in the world by biomass burning. This shows that biomass burning in western Europe is not important compared to that in the rest of the world. Therefore, forest fires in this part of the world do not contribute heavily to the carbon burden in the atmosphere.

Forests fires in western Europe are spatially and temporally unequally distributed. The extent of burning varies upon the particular climatic conditions of the countries, as well as on continental changes in the weather pattern. Thus, from one year to another, the extent of burning can greatly vary. For example, 1987 was a below average year in terms of fires (432 977 ha), whereas 1985 was an above average year in terms of fires (1 058 342 ha). Nevertheless, for both years, the spatial distribution was about the same. Forests fires

are mostly located around the Mediterranean basin where, in summer, there is high temperature, little precipitation, and strong local wind. This is due to the particular air circulation over western Europe. The distribution in 1987 of the burning around the Mediterranean basin, in terms of total burning, was the following:

- 33% occurred in Spain,
- 17% occurred in Portugal,
- 27% occurred in Italy,
- 10% occurred in Greece.

Therefore, 87% of the burning in western Europe in 1987 was concentrated in 22% of the land surface.

Satellite remote sensing of forests fires in these four countries was selected to provide a $1^{o} \times 1^{o}$ grid of trace gas emissions released through burning. The imagery used was the LAC data provided by the AVHRR sensor onboard the NOAA-9 satellite. This imagery, though not of very high resolution, was the only one affordable for these studies on a regional scale. After having processed the acquired data, and having located the largest visible scars, the spectral properties of these isolated scars were studied. It turns out that spectral properties of scars are variable. They depend upon the ecosystem, upon the age of the scar, and upon the damage incurred on the vegetation by burning. Nevertheless, common features to scars can be defined: scars reflect more than vegetation in the NOAA-AVHRR channel 1, but less in the channel 2, and temperatures of scars (Channel 4) are higher than those of vegetation due to the evapo-transpiration cooling effect of vegetation.

An evaluation of the similarity between different scars is given by their spectral overlap in different wavelength bands. For some scars, the average overlap in channels 1

and 2 can be as low as 42%. This explains why the regional classification of scars is not successful. It is not possible to classify all scars with only a training set characteristic of any one type of scar. Moreover, it turns out that areas that are not scars often have spectral properties similar to those of scars. Not only do all the scars not appear in the classification process, whatever it might be (minimum distance or maximum likelihood), but also areas, that are not scars, like coastal pixels or cloud shadows, are included in the class characteristic of scars. This prevents a reliable classification on a regional scale.

When a regional classification was possible, the precision of the results (size of the individual fires and spatial distribution) needed to be quantified. In order to do this, the classification of scars was implemented on a local scale (restricted area containing only one ecosystem). In the study area, all the scars likely to appear on the LAC imagery, were identified via a computer search through a database. It turns out that less than 50% of the actual scars appear in the classified image. Therefore, even if the regional classification was satisfactorily implemented (separate training of scars characteristic of different ecosystems and classification in a cloudless image), the classification error would be too large to provide a reliable estimation of the spatial distribution and of the size of the scars.

The NOAA-9 AVHRR sensor is not able to accurately sense scars in western Europe because its spatial and spectral resolutions are not high enough. Scars in western Europe are, on average, too small to be sensed at an affordable price. Therefore, the $1^{o}\times1^{o}$ grid of trace gas emissions released through burning will not easily and precisely be obtained unless a higher resolution imagery is used or complete and detailed information about the particular fires are provided on a country to country basis. However, at present, it does not appear to be necessary to remotely sense fires in western Europe because of the negligible amount of trace gases released to the atmosphere by biomass burning.

# BIBLIOGRAPHY


Andreae, M. O. Global Biomass Burning: Atmospheric, Climatic, and Biospheric Implications. 3-21 Cambridge, Massachusetts: MIT Press, 1991.

Avery, T. E., Berlin, G. L. Fundamentals of Remote Sensing and Airphoto Interpretation. 5th edition, Macmillan Publishing Company, 1992.

Brustet, J. M., Vickos, J. B., Fontan, J., Manissadjan, K., Podaire, A., Lavenu, F. Global Biomass Burning: Atmospheric, Climatic, and Biospheric Implications. 47-52 Cambridge, Massachusetts: MIT Press, 1991.

Brustet, J. M., Vickos, J. B., Fontan, J., Podaire, A., Lavenu, F. Global Biomass Burning: Atmospheric, Climatic, and Biospheric Implications. 53-60 Cambridge, Massachusetts: MIT Press, 1991.

Cahoon, Jr., D. R., Stocks, B. J., Levine, J. S., Cofer III, W. R., O'Neill, K. P. Seasonal Distribution of African Savanna Fires, Nature, Vol 359, 812-815.

Cahoon, Jr., D. R., Stocks, B. J., Levine, J. S., Cofer III, W. R., Chung, C. C. Journal of Geophysical Research. vol. 97, no. D4, 3805-3814, 1992.

Cahoon, Jr., D. R., Levine, J. S., Cofer II, W. R., Miller, J. E., Minnis, P., Tennille, G. M., Yip, T. M., Stocks, B. J., Heck, P. W. Global Biomass Burning: Atmospheric, Climatic, and Biospheric Implications. 61-66 Cambridge, Massachusetts: MIT Press, 1991.

Connors, V. S., Cahoon, Jr., D. R., Reichle, H. G., Garstang, M., Seiler, W., Scheel, H. E. Global Biomass Burning: Atmospheric, Climatic, and Biospheric Implications. 147-153 Cambridge, Massachusetts: MIT Press, 1991.

Dozier, J. A Method for Satellite Identification of Surface Temperature Fields of Subpixel Resolution. Remote Sensing of Environment, 11, 221-229, 1981.

Drury, S. A. A Guide to Remote Sensing: Interpreting Images of the Earth. Oxford Science Publications, 1990.

EOSAT, Purchasing Guide.

Europe's green mantle: heritage and future of our forests. Commission of the European Communities, Newsletter on the Common Agricultural Policy, 1984, (n° 204).

Forest Condition in Europe: Executive Summary of the 1992 Report. Economic and Social Council, EB.AIR/R.71, United Nations, New York, 1992.

Forest Fire Statistics 1985-1988. Economic Commission for Europe, Food and Agriculture Organization, ECE/TIM/51, United Nations, New York, 1990.

Goode's World Atlas. 18th edition, Rand Mc Nally, 1992.

Houghton, R. A. Global Biomass Burning: Atmospheric, Climatic, and Biospheric Implications. 322-325 Cambridge, Massachusetts: MIT Press, 1991.

IVAS General Module User's Guide. International Imaging Systems, 1991.

Kaufman,Y. J., Setzer, A., Justice, C.,Peireira, M. C., Fung, I. Fire in the Tropical Biota: Ecosystem Processes and Global Challenges. 371-397 Berlin, Heidelberg: Sprinter-Verlag, 1990.

Kidwell, K. B. NOAA Polar Orbiter Data Users' Guide. National Oceanic and Atmospheric Administration, Satellite Data Services Division, U. S. Department of Commerce, 1991.

Les Feux de Forêts. SECRETARIAT d'ETAT chargé de l'ENVIRONNEMENT et de la PREVENTION des RISQUES TECHNOLOGIQUES et NATURELS MAJEURS, Centre Régional de documentation pédagogique, Dijon, France, 1991.

Levine, J. S., Cofer III, W. R., Winstead, E. L., Rhinehart, R. P., Cahoon, Jr., D. R., Sebacher, D. I., Stocks, B. J. Global Biomass Burning: Atmospheric, Climatic, and Biospheric Implications. 264-271 Cambridge, Massachusetts: MIT Press, 1991.

Lopez Garcia, M. J., Caselles V. Geocarto International: a Multi-disciplinary Journal of Remote Sensing. Vol. 6, 1, 1991.

Malingreau, J. P. Fire in the Tropical Biota: Ecosystem Processes and Global Challenge. 337-368 Berlin, Heidelberg: Sprinter-Verlag, 1990.

Mc Clave, J. T., Dietrich, II, F. H. Statistics. 2nd Edition, Dellen Publishing Company, Santa Clara, 1982.

Pearson, II, F. Map Projections: Theory and Applications. Boca Raton, Florida: CRC Press, Inc., 1990.

Prinn, R. G. Global Biomass Burning: Atmospheric, Climatic, and Biospheric Implications. 22-28 Cambridge, Massachusetts: MIT Press, 1991.

Radke, L. F., Hegg, D. A., Hobbs, P. A., Nance, J. D., Lyons, J. H., Laursen, K. K., Weiss, R. E., Riggan, P. J., Ward, D. E. Global Biomass Burning : Atmospheric, Climatic, and

Biospheric Implications. 209-224 Cambridge, Massachusset: MIT Press, 1991.

Robinson, J. Global Biomass Burning: Atmospheric, Climatic, and Biospheric Implications. 67-73 Cambridge, Massachusetts: MIT Press, 1991.

Schowengerdt, R. A. Techniques for Image Processing and Classification in Remote Sensing. Academic Press, Inc., 1983.

Seiler, W. and P. J. Crutzen. Estimates of Gross and Net Fluxes of Carbon Between the Biosphere and the Atmosphere from Biomass Burning. Climate Change, 2, 207-247, 1980.

Stocks, B. J. Global Biomass Burning: Atmospheric, Climatic, and Biospheric Implications. 197-202 Cambridge, Massachusetts: MIT Press, 1991.

System 600 Version 4.0 Command Reference CPU I (A-K) Volume II. International Imaging Systems, 1990.

System 600 Version 4.0 Command Reference CPU II (L-Z) Volume III. International Imaging Systems, 1990.

Trends'91 :A Compendium of Data on Global Change. Carbon Dioxide Information Analysis Center, ed. Boden, T. A., Sepanski, R. J., Stoss, F. W., December 1991.

Wallace, J. M., Hobbs, P. V. Atmospheric Science: an Introductory Survey. Academic Press, 1977.

Wallen, C., C. Climates of Northern and Western Europe.

Warren, S., G., Hahn, C., J., London, J., Chervin, R., M., Jenne, R., L. Global Distribution of Total Cloud Cover and Cloud Type Amounts over Land. NCAR/TN-273+STR, 1986.

Wood, C. A., Nelson, R. Global Biomass Burning: Atmospheric, Climatic, and Biospheric Implications. 29-40 Cambridge, Massachusetts: MIT Press, 1991.

Woods, D. C., Chuan, R. L.,Cofer III, W. R., Levine, J. S. Global Biomass Burning: Atmospheric, Climatic, and Biospheric Implications. 240-244 Cambridge, Massachusetts: MIT Press, 1991.

# VITA

Philippe Jean-François Le Canut

Born October 20, 1968 in Caen, France. Graduated from the Ecole Nationale Supérieure des Arts et Métiers (ENSAM), in Paris, France, June 1991.

In September 1991, the author entered the College of William and Mary and subsequently enrolled in the graduate program for the M.A. in Applied Science.